Design and fabrication of high-Q optical microresonators for integrated passive mode-locked lasers

Riku Imamura

Graduate School of Science and Technology
Keio University

This dissertation is submitted for the degree of
Doctor of Philosophy

August 2025

Keio University

Graduate School of Science and Technology
School of Integrated Design Engineering

Design and fabrication of high-Q optical microresonators for integrated passive mode-locked lasers

by

Imamura, Riku

A THESIS SUBMITTED
IN PARTIAL FULFILLMENT OF
THE REQUIREMENTS FOR THE DEGREE
Doctor of Philosophy

APPROVED, THESIS COMMITTEE:

Tanabe, Takasumi

Saiki, Toshiharu

Takeoka, Masahiro

Watanabe, Shinichi

Set, Sze Yun

I would like to dedicate this thesis to my parents ...

Abstract

Since the invention of the laser, mode-locked lasers, in particular, have played a critical role as foundational technology in generating ultrashort pulses of light and have paved the way for numerous applications. However, conventional mode-locked lasers require large-scale optical setups, presenting challenges in miniaturization and enhanced integration stability. On the other hand, microresonators, by confining light within a microscale region, significantly enhance light-matter interactions, enabling various phenomena, including nonlinear optical effects. Optical frequency combs (microcombs) and soliton microcombs generated using microresonators have emerged as highly promising research fields with academic and industrial significance. Nevertheless, state-of-the-art microcomb generation primarily relies on injecting a pump laser into a microresonator and obtaining gain through four-wave mixing, which demands highly precise wavelength control and often leaves residual pump light in the output. To overcome these challenges, it is crucial to achieve passive mode-locking in a self-oscillating laser by integrating both gain and nonlinear loss media into the microresonator. This thesis explores the design and fabrication of high-Q microresonators as a key step toward developing integrated passive mode-locked lasers.

In Chapter 1, the fundamental concepts of mode-locked lasers, previous research, and the objectives of this study are outlined to provide the background for this thesis.

Chapter 2 focuses on the principles of microresonators, the core devices of this study, as well as the basic theory and previous research on related nonlinear optical effects.

Chapter 3 describes the fabrication process and performance evaluation of high-Q microresonators. Specific attention is given to methods for doping erbium ions as the gain medium and incorporating carbon nanotubes or graphene as nonlinear loss materials.

Chapter 4 presents the design of integrated mode-locked lasers based on numerical analysis. Two approaches are discussed: single-resonator models and coupled-resonator models. In the single-resonator model, passive mode-locking is achieved by adding a saturable absorber and maintaining a Q higher than 10^8. Meanwhile, in the coupled-resonator model, passive mode-locking is similarly achieved without a saturable absorber, provided the microresonator maintains a Q of 10^8.

Chapter 5 concludes the thesis by summarizing the findings and discussing prospects. This study demonstrates the potential of integrated passive mode-locked lasers based on microresonators, providing clear design guidelines and fabrication processes for achieving passive mode-locking.

Table of contents

List of figures

List of tables

Chapter 1

Introduction and Motivation

1.1 Introduction to ultrashort pulse lasers

Ultrashort pulse lasers are a specialized class of lasers capable of producing light pulses with durations in the picosecond (10^{-12} s) to femtosecond (10^{-15} s) range [1]. These lasers have transformed how we explore and interact with the physical world, offering unparalleled precision in time and intensity. Unlike continuous-wave lasers, ultrashort pulsed lasers concentrate their energy into brief intervals, generating incredibly high peak powers even when the average power remains modest. This unique property allows them to access nonlinear optical effects that are otherwise unattainable, making them essential in various scientific, industrial, and medical applications. Their unique characteristics have made them indispensable tools in multiple applications, from basic research to industrial and medical fields.

The foundation of ultrashort pulse generation lies in mode-locking, which synchronizes the phases of multiple longitudinal modes in a laser cavity. In a typical laser, these modes oscillate independently, producing continuous-wave emission. However, constructive interference occurs regularly when their phases are locked, forming pulses. Mode-locking can be achieved actively, using external modulators to periodically modulate intracavity parameters or passively through saturable absorbers that preferentially transmit high-intensity light and suppress lower intensities.

1.1.1 Principle of mode-locking

Mode-locking is a fundamental mechanism that enables the generation of ultrashort pulses by synchronizing the phases of multiple longitudinal modes that oscillate independently

(Fig. 1.1). Mode-locking aligns their phases, resulting in constructive interference at regular intervals and the formation of periodic pulses.

Mathematically, the electric field $E(t)$ of a mode-locked laser can be expressed as the superposition of N longitudinal modes:

$$E(t) = \sum_{n=1}^{N} A_n e^{i(2\pi f_n + \phi_n)} \tag{1.1}$$

where A_n, f_n, and ϕ_n represent the amplitude, frequency, and phase of the n-th mode, respectively, mode-locking ensures that all ϕ_n are aligned, leading to sharp pulses separated by the cavity round-trip time. This process is essential for generating ultrashort pulses with high peak powers.

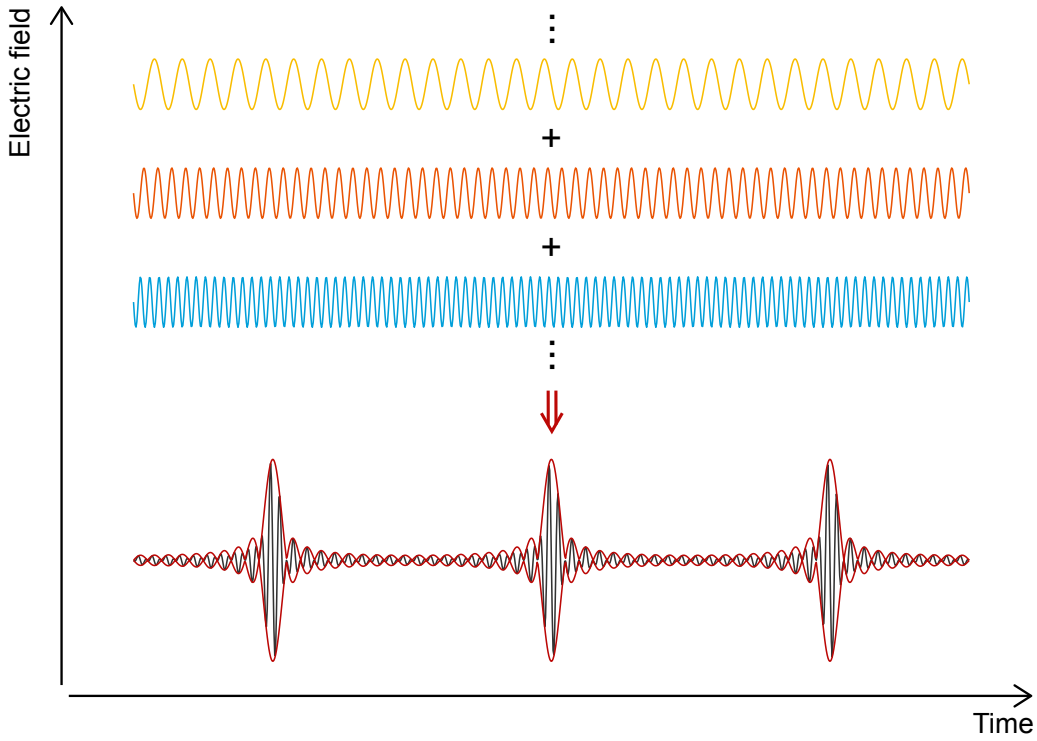

Fig. 1.1 A schematic illustration of mode-locking mechanism. The phases of multiple longitudinal modes that oscillate independently synchronize. The time duration of short pulses is periodic, given by the cavity round-trip time $T_R = 2L/v_g$, where L is the laser cavity length and v_g is the group velocity.

Two primary methods are used to achieve mode-locking: active mode-locking and passive mode-locking. Each method relies on different physical principles but shares the common goal of inducing phase coherence among the cavity modes.

1.1.2 Mode-locking platforms

Ordinary system

In mode-locked pulses from lasers, a schematically illustrated setup with a gain medium and a loss medium inside a laser cavity is shown in Figure 1.2. There are two types of mode-locking: active and passive.

Active mode-locking employs external modulation of the intracavity parameters, such as phase or loss, to enforce periodic pulse formation. This is typically achieved using acousto-optic modulators (AOM) [2] or electro-optic modulators (EOM) [3], driven at frequencies synchronized to the cavity round-trip time (1.3(a)). Active mode-locking offers precise control of modulators and is often used in systems where external synchronization is necessary. Hence, it requires additional electronic components, increasing system complexity.

In contrast, passive mode-locking relies on intracavity nonlinear effects to enhance pulse formation. Saturable absorbers (SAs), which preferentially transmit high-intensity light and absorb low-intensity light, are a common mechanism for achieving passive mode-locked lasers (1.3(b)). SAs can be broadly categorized into artificial and natural types. An example of an artificial SA is Kerr lens mode-locking, which exploits intensity-dependent focusing within the gain medium to achieve pulse formation. On the other hand, natural SAs include materials such as carbon nanotubes (CNTs) and two-dimensional materials like graphene, which exhibit inherent saturable absorption properties. Passive mode-locking typically results in shorter pulses and simpler designs, but it may require careful cavity optimization to ensure stability.

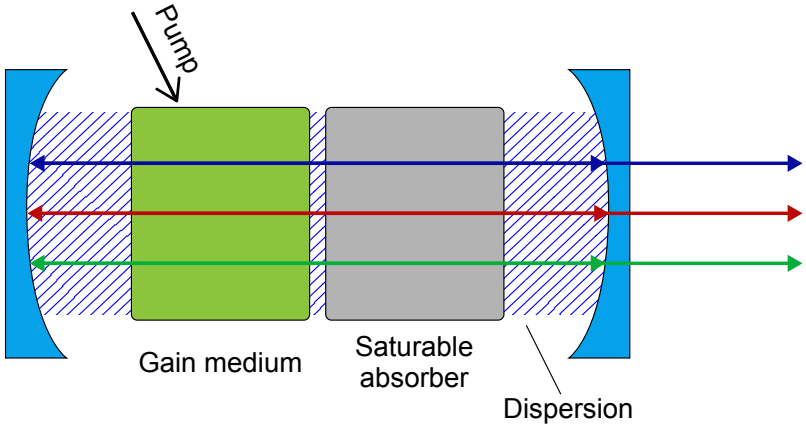

Fig. 1.2 A schematic illustration of mode-locking.

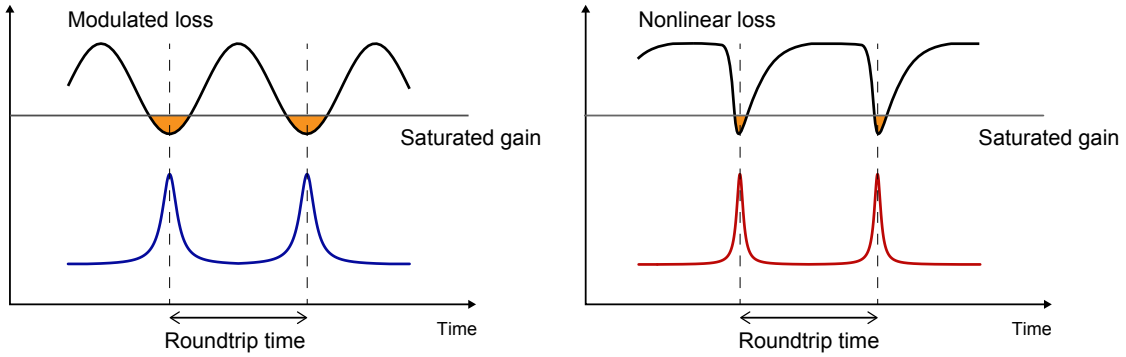

Fig. 1.3 (a) In active mode-locking, an external signal modulates optical losses through mechanisms such as the acousto-optic or electro-optic effect. This external modulation induces a sinusoidal variation in loss, with a period matching the cavity round-trip time. At a steady state, the saturated gain allows net amplification only near the minimum loss points, thereby confining the supported pulses to durations significantly shorter than the cavity round-trip time. (b) In passive mode-locking, a saturable absorber provides self-amplitude modulation by introducing intensity-dependent losses. Low-intensity light experiences higher losses, while high-intensity pulses saturate the absorber, reducing losses at the pulse peak. This creates a loss modulation with fast saturation during the pulse and slower recovery, depending on the SA's absorption mechanism.

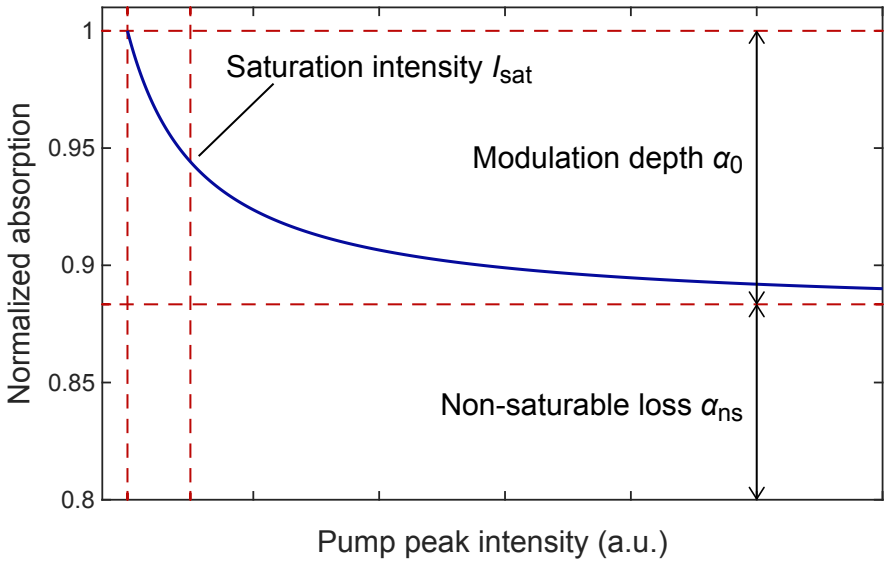

Fig. 1.4 Nonlinear absorption curve of a saturable absorber, plotted as normalized absorption versus pump peak intensity. The key parameters for a saturable absorber are saturation intensity I_{sat}, modulation depth α_0, and non-saturable loss α_{ns}. The calculation parameters are based on values reported in previous studies.

Solid state laser

Solid-state lasers, which use a solid gain medium doped with active ions such as titanium, neodymium, or ytterbium, are among the most versatile platforms for achieving mode-locking. As a historically significant example, Ti: sapphire lasers were first developed in the 1980s, revolutionizing ultrafast laser science due to their exceptionally broad gain bandwidth ($650 \sim 1100$ nm).

In these solid-state lasers, the passive mode-locking method is frequently used due to its simplicity and ability to generate ultrashort pulses, often in the femtosecond range. A notable example is Kerr lens mode-locking (Fig. 1.5), a technique that exploits the intensity-dependent refractive index of the gain medium, commonly Ti: sapphire lasers. This effect creates a self-focusing phenomenon, where high-intensity regions of the beam experience stronger focusing than low-intensity regions. This result is a lensing effect that depends on the intensity of the light, hence the term "Kerr lens." The cavity is designed so that the tightly focused beam experiences lower losses than the broader, less focused continuous wave (CW) light. In Kerr lens mode-locking, it has been reported that miniaturizing the cavity enables the generation of high repetition rate pulses at 20 GHz [4].

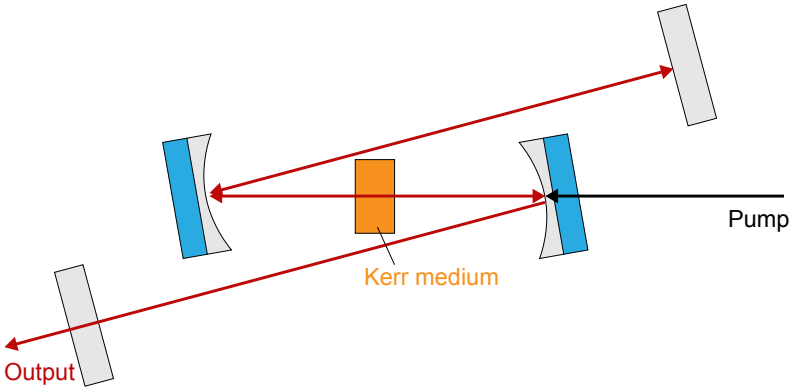

Fig. 1.5 A schematic illustration of Kerr lens mode-locking.

Semiconductor laser

Semiconductor lasers, also known as laser diodes, are a compact and efficient platform for mode-locking operation. Their small footprint, high electrical-to-optical conversion efficiency, and direct electrical pumping make them ideal for applications requiring ultrashort pulses and high repetition rates. Semiconductor lasers emerged as a platform for mode-locking in the 1980s, driven by advances in material science and the development of high-speed electronic components. Integrating saturable absorbers and external cavities marked

significant milestones, enabling shorter pulse durations and higher repetition rates. These innovations have been instrumental in transitioning from experimental demonstrations to practical applications

Passive mode-locking in semiconductor lasers relies on nonlinear intracavity elements, such as semiconductor saturable absorber mirrors (SESAMs), to enable pulse formation. Among the notable advancements in semiconductor laser platforms are the Vertical-External-Cavity Surface-Emitting Laser (VECSEL) and the Mode-Locked Integrated External-Cavity Surface-Emitting Laser (MIXSEL). VECSELs are optically pumped, surface-emitting lasers featuring an external cavity and a gain region engineered with multiple quantum wells. These lasers combine high output power with excellent beam quality and, when integrated with SESAMs, can achieve mode-locking with pulse durations ranging from a few picoseconds to sub-picoseconds [5]. Their broad tunability and scalable power make VECSELs ideal for applications such as frequency comb generation and terahertz radiation sources. MIXSELs, in contrast, integrate the gain medium and SESAM within a single semiconductor chip, eliminating the need for external cavity alignment. This monolithic design simplifies the system while retaining the ability to produce ultrashort pulses and operate at gigahertz repetition rates [6].

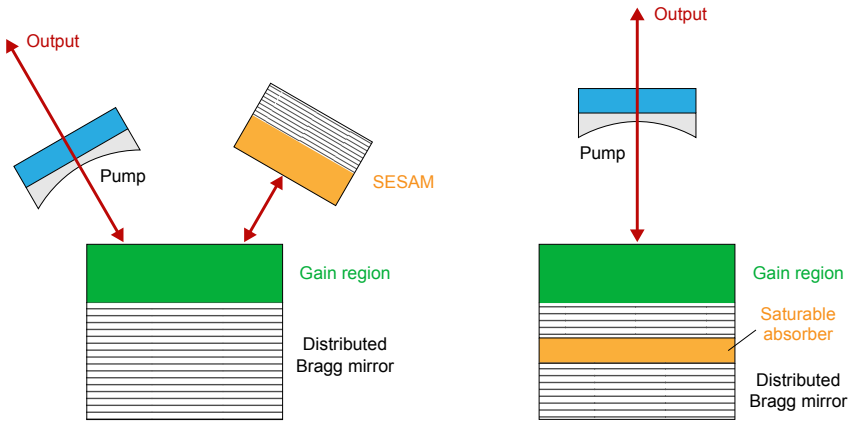

Fig. 1.6 Schematic illustrations of mode-locking in semiconductor lasers. (a) The Vertical-External-Cavity Surface-Emitting Lasers (VECSELs) have the gain region fabricated with multiple quantum wells and the semiconductor Bragg mirror, which reflects light back into the gain region, ensuring efficient amplification. The external cavity provides an additional saturable absorber. In mode-locking operation, SESAM is placed within the cavity system. (b) Mode-locked integrated External-Cavity Surface-Emitting Lasers (MIXSELs) are monolithic semiconductor lasers that integrate the gain medium, the distributed Bragg mirror, and the SESAM within a single chip.

Fiber ring laser

Fiber lasers have established themselves as a critical platform for mode-locked laser systems, offering high efficiency, excellent beam quality, and robust operation. Their compact design and ability to support long interaction lengths make them particularly suitable for generating ultrashort pulses. Since their inception in the 1960s, fiber lasers have undergone significant advancements, particularly in the development of doped fiber materials and nonlinear optical components. This has enabled a wide range of configurations and applications in ultrafast optics.

Passive mode-locking in fiber lasers is achieved in various ways [7]. The simple configuration typically relies on saturable absorbers, introducing an intensity-dependent loss mechanism that suppresses CW operation while facilitating pulse shaping. These absorbers can be implemented using bulk materials such as SESAMs or advanced nanomaterials like carbon nanotubes and graphene. These materials offer precise control over saturation intensity, recovery times, and operation bandwidths, making them suitable for diverse applications. Nonlinear mechanisms such as nonlinear polarization rotation (NPR) and nonlinear amplifying loop mirrors (NALM) also play a vital role in fiber laser mode-locking. NPR exploits the intensity-dependent phase shift of polarized light within the fiber, which enables passive mode-locking in combination with polarizing components [8]. NALM, on the other hand, uses an optical loop containing a gain-doped fiber and nonlinear fiber where nonlinear phase shifts enhance mode-locked operation through constructive interference for high-intensity pulses [9–11]. Both techniques provide excellent stability and allow for fine-tuning output characteristics through careful adjustment of cavity parameters.

In practical configurations, they operate at different wavelengths depending on the ions in the gain fiber, with central wavelengths covering a wide range from the near-infrared to the mid-infrared regions. These lasers demonstrate exceptional performance metrics, with pulse durations of 50 fs to several picoseconds and repetition rates ranging from 10 MHz to 10 GHz. The scalability and adaptability of fiber lasers make them versatile tools for a wide range of applications.

Microresonator

Microresonators have emerged as a versatile platform for mode-locked laser systems, enabling the generation of optical frequency combs through compact and efficient architectures [12, 13]. Optical frequency combs, characterized by their equidistant and mutually coherent spectral lines, have revolutionized precision optical frequency measurements and expanded the reach of laser-based technologies. Originally developed in conventional mode-locked

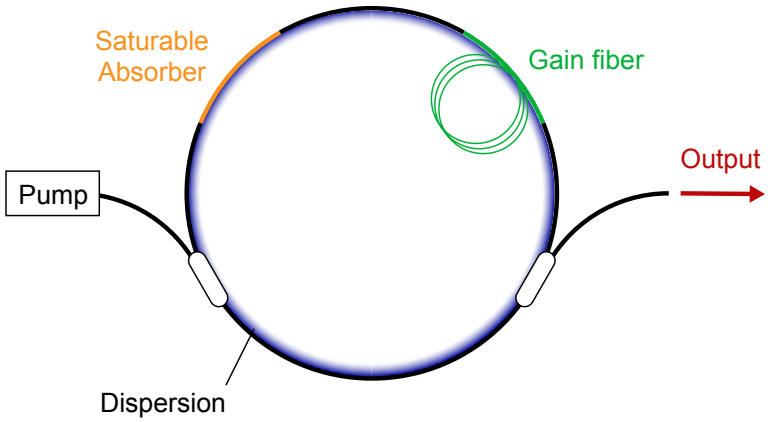

Fig. 1.7 A concept of a mode-locked fiber ring laser. The ring resonator is composed of a gain fiber, a saturable absorber, and a nonlinear fiber, and it is designed to achieve dispersion compensation for the entire system.

lasers, frequency combs have since been realized in microresonators, leveraging unique properties such as high quality factors (Q) and small mode volumes.

Figure 1.8 shows a comparison of conventional frequency comb generators and microresonators. Conventional mode-locked lasers rely on resonators containing saturable absorbers, gain media, and pump lasers. The gain medium produces light across multiple frequencies, which are synchronized by the saturable absorber to form ultrashort pulses. The pulse repetition rate corresponds to the resonator's free spectral range (FSR). By contrast, microresonators achieve mode-locking through nonlinear processes, such as cascaded four-wave mixing (FWM), driven by a continuous-wave (CW) pump laser. This process generates optical frequency combs with significantly higher repetition rates, often between 10 and 1000 GHz, exceeding the capabilities of conventional mode-locked lasers.

The first demonstration of microcombs was reported in 2007 by the Max-Planck-Institute for Quantum Optics (MPQ) [14], which showed that cascaded FWM in microresonators could produce broadband and equally spaced spectral lines in the frequency domain. However, these early microcombs did not exhibit temporal pulses.

A key breakthrough in microresonator mode-locking was the demonstration of soliton microcombs. The introduction of optical temporal cavity solitons resolved this challenge, and in 2014, researchers at the Swiss Federal Institute of Technology in Lausanne (EPFL) demonstrated soliton microcomb generation in MgF_2 microresonators [15], producing sech^2-shaped spectra and picosecond-order pulses. These occur when the relative phases of the

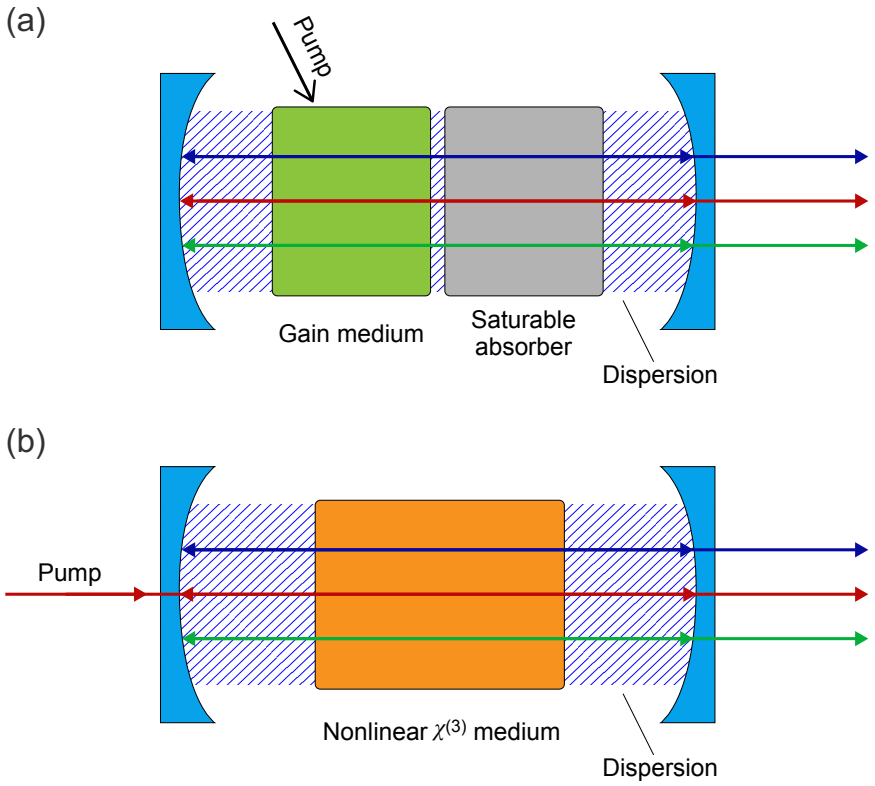

Fig. 1.8 Comparison of conventional frequency comb generators and microresonator-based comb generation. Conventional frequency comb generation in mode-locked lasers requires a gain medium and a saturable absorber within the resonator, as shown in panel (a). In contrast, panel (b) illustrates frequency comb generation in a microresonator, which is governed by a nonlinear χ^3-medium and can be described in the frequency domain. A main difference between the comb generators is that the pump laser constitutes one of the comb modes in microresonators.

comb lines are synchronized, resulting in ultrashort pulses. Soliton propagation within the microresonator balances Kerr nonlinearity with anomalous dispersion, creating a stable pulse train (Fig. 1.9 (b)). The concept of soliton microcombs builds on earlier work in fiber-based optical cavities and is adapted for compact microresonator systems [16].

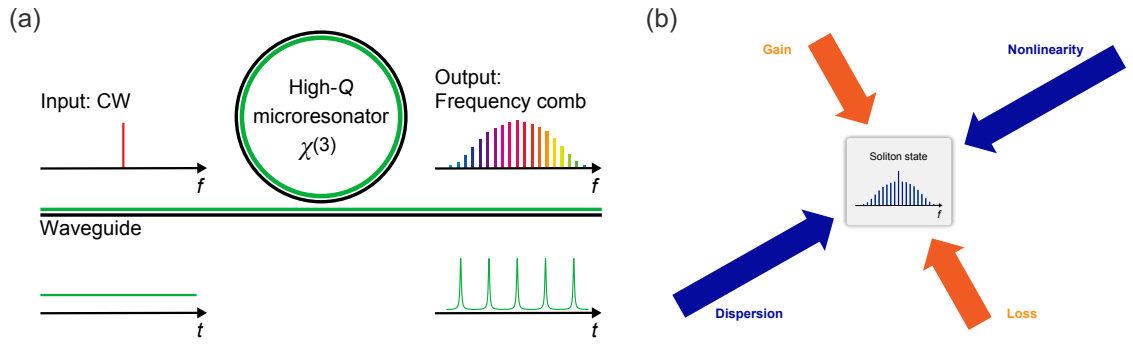

Fig. 1.9 (a) The microcomb and soliton microcomb generation system is illustrated with a dielectric high-Q microresonator fabricated from χ^3 material driven by a CW laser through a coupled external waveguide. (b) A schematic illustration of balances between Kerr nonlinearity, dispersion, gain, and loss in a microresonator system.

Soliton microcombs have since been realized in various microresonator platforms, including SiO_2 disks [17], SiO_2 toroids, SiO_2 rods, Si_3N_4 rings, AlN rings, and fiber-based Fabry-Pérot cavities. These systems offer compact, low-power, and high repetition rate sources of ultrashort pulses. Furthermore, octave-spanning soliton microcombs, critical for self-referencing and carrier-envelope offset stabilization, have been achieved both directly within microresonators and via spectral broadening in nonlinear fibers.

Microresonator-based mode-locked lasers have advanced optical frequency comb technology by combining compact cavity size with high repetition rates. This enables applications in precision metrology, telecommunications, spectroscopy, and quantum technologies. Their ability to integrate soliton formation within dielectric microresonators underscores their potential as a cornerstone for next-generation photonics.

1.2 Challenges in the related researches

In the quest to realize pulse sources free from background light using microresonators, two representative research platforms that combined a gain-doped microcavity with a saturable absorber were investigated. The first example is a waveguide-based laser by the group at Massachusetts Institute of Technology (MIT) [18–20]. Their design incorporates an optical

waveguide doped with erbium ions over a length of a few centimeters to provide gain. A saturable Bragg reflector or a nonlinear interferometer is placed externally and serves as the saturable absorber. While this approach offers the advantage of on-chip integration, the achievable repetition rate is limited to around 2 GHz, primarily due to insufficient gain in the resonator. Although such research was actively pursued around the 2010s, difficulties in overcoming the gain deficiency have curtailed recent progress in this area.

A second example is the fiber Fabry-Pérot cavity laser reported by the group at The University of Tokyo [21]. Here, a Fabry-Pérot resonator is formed by mounting mirrors on both ends of a highly doped erbium and ytterbium co-doped fiber. A saturable absorber, consisting of carbon nanotubes (CNTs) optically deposited on a fiber ferrule, is inserted in front of one mirror. By sequentially reducing the cavity length from 25 mm to 10 mm and finally to 5 mm, they investigated the upper limits of repetition rate achievable in this configuration. Under a 5 mm cavity length, they reached a repetition rate of 19.45 GHz, which was essentially the limit for this system.

These two platforms share a common challenge: insufficient resonator gain. Shortening the cavity length is indispensable for higher repetition rates, but doing so decreases the gain medium's physical length and, thus, the total gain, making stable mode-locking increasingly difficult. In contrast, the erbium-doped microresonator with a saturable absorber (e.g., CNTs and graphene) that we investigate in this work aims to address this very issue by taking advantage of a microresonator with a Q-factor exceeding 10^7. Even with a short cavity, the high-Q factor ensures adequate gain, offering the prospect of higher repetition rates than in prior studies. Such a compact, integrated source of high-repetition-rate, short optical pulses is valuable for diverse applications, including arbitrary waveform generation, ultrafast sampling, communications, and laser machining.

Moving on to the erbium-doped microresonators, the initial demonstration of erbium-doping in a microsphere was reported by the group at Caltech in 2003 [22]. Subsequent studies have been conducted largely because the fabrication process for such microspheres can be relatively straightforward. For instance, a study published in 2007 [23] investigated how the resonator's Q-factor changes with erbium ions excitation: when the ions are unexcited, their absorption reduces the Q-factor, whereas excitation provides gain, effectively lowering the total loss and raising the Q-factor. Previous examples also show that ytterbium ions are codoped with erbium ions to enhance lasing efficiency [24]. Moreover, using gain from erbium ions to facilitate soliton generation has been proposed [25], offering easier access to the soliton state: normally achieved only through specialized procedures [26].

Research on toroidal microresonators doped with erbium ions was reported for the first time in [22], after which several fundamental studies have followed. Examples include a

direct measurement of the gain lifetime [27] and theoretical and experimental examinations of saturable nonlinearities in erbium-doped resonators [28]. In the case of whispering-gallery-mode (WGM) resonators, lasing typically occurs in both the clockwise (CW) and counterclockwise (CCW) directions, but intentionally introducing scatterers into the cavity can enable unidirectional lasing [29]. There have also been demonstrations of Fano-like resonances, a nonlinear phenomenon [30], observed in erbium-doped resonators [31, 32]. Specifically, when the gain from erbium ions compensates for the cavity's inherent losses, adjusting the intensities of the pump and probe beams and the sweep rate yields asymmetric transmission spectra reminiscent of Fano resonances.

The most promising approach is the self-injection locked (SIL) soliton microcomb. SIL soliton microcombs have recently attracted significant attention as a promising route toward simplifying the generation of coherent, broad-spectrum frequency combs in high-Q microresonators [33, 34]. In this approach, a narrow-linewidth laser is coupled to a microresonator such as a microring and a whispering-gallery-mode structure, and a portion of the intracavity field is scattered or reflected back into the laser cavity, causing the laser frequency to lock to the resonator's mode [35]. This intrinsic feedback mechanism mitigates the need for external servo loops or complex frequency control systems and dramatically narrows the laser linewidth, enhancing the stability of the soliton state formed via Kerr nonlinearity. As a result, SIL soliton microcombs can provide a robust platform for on-chip comb generation, allowing for reduced device footprint and potentially lower energy consumption. However, certain challenges persist: the self-injection process restricts the range over which the laser can be tuned, requires an optimal level of backscattering or reflection, and can be sensitive to environmental fluctuations that shift the cavity resonance or disturb the feedback path. Furthermore, higher-order dispersion and multimode interactions within the resonator may introduce additional complexity, potentially limiting the bandwidth and coherence of the comb. Despite these hurdles, ongoing progress in integrated photonics design and packaging continues to advance the stability and performance of SIL soliton microcombs, paving the way for compact, robust frequency-comb sources suitable for precision metrology, optical communications, and emerging quantum applications.

1.3 Thesis objective and structure

Since the invention of the laser, mode-locked lasers, in particular, have played a critical role as foundational technology in generating ultrashort pulses of light and have paved the way for numerous applications. However, conventional mode-locked lasers require large-scale optical setups, presenting challenges in terms of miniaturization and enhanced stability through

integration. On the other hand, microresonators, by confining light within a microscale region, significantly enhance light-matter interactions, enabling various phenomena, including nonlinear optical effects. Optical frequency combs (microcombs) and soliton microcombs generated using microresonators have emerged as highly promising research fields with academic and industrial significance. Nevertheless, state-of-the-art microcomb generation primarily relies on injecting a pump laser into a microresonator and obtaining gain through four-wave mixing. This process demands highly precise wavelength control and often leaves residual pump light in the output. It is crucial to overcome these challenges to achieve passive mode-locking in a self-oscillating and background-free operating laser by integrating gain and nonlinear loss media into the microresonator. This thesis explores the design and fabrication of high-Q microresonators as a key step toward developing integrated passive mode-locked lasers.

Chapter 1 outlines the fundamental concepts of mode-locked lasers, previous research, and the objectives of this study to provide the background for this thesis.

Chapter 2 focuses on the principles of microresonators, the core devices of this study, as well as the basic theory and previous research on related nonlinear optical effects.

Chapter 3 describes the fabrication process and performance evaluation of high-Q microresonators. Specific attention is given to methods for doping erbium ions as the gain medium and incorporating carbon nanotubes or graphene as nonlinear loss materials.

Chapter 4 presents the design of integrated mode-locked lasers based on numerical analysis. Two approaches are discussed: single-resonator models and coupled-resonator models. In the single-resonator model, passive mode-locking is achieved by adding a saturable absorber and maintaining a Q higher than 10^8. Meanwhile, in the coupled-resonator model, passive mode-locking is similarly achieved without a saturable absorber, provided the microresonator maintains a Q of 10^8.

Chapter 5 concludes the thesis by summarizing the findings and discussing prospects. This study demonstrates the potential of integrated passive mode-locked lasers based on microresonators, providing clear design guidelines and fabrication processes for achieving passive mode-locking.

Chapter 2

Introduction to optical microresonators

This chapter describes a comprehensive introduction to optical microresonators, which are used as the primary device in this research, emphasizing their fundamental principles and advanced research topics. The chapter begins with a discussion on the fundamentals of microresonators, detailing key characteristics such as resonance frequency, quality factor, cavity decay rate, and effective mode area, which collectively define their optical performance. The roles of cavity dispersion and thermal effects are then explored, highlighting their influence on light propagation and stability within the resonator. Nonlinear optical processes, including Kerr effects and parametric oscillations, are also examined as critical phenomena enabling advanced applications such as frequency comb generation.

The chapter further delves into optical coupling mechanisms, including evanescent coupling, which are vital for efficiently interfacing external light with microresonators. Practical aspects, such as tapered fiber fabrication and quality factor measurements, are also discussed, providing a complete framework for experimental implementations.

The following section introduces optical frequency comb generation in optical microresonators, focusing on its principles. Particular attention is given to soliton microcombs, detailing their formation mechanisms and recent advancements in their generation.

2.1 Fundamentals of microresonators

2.1.1 Microresonator characteristics

Whispering-gallery-mode microresonators

Optical resonators are essential components in photonics, enabling the confinement and manipulation of light within small volumes for various applications. Among the many types

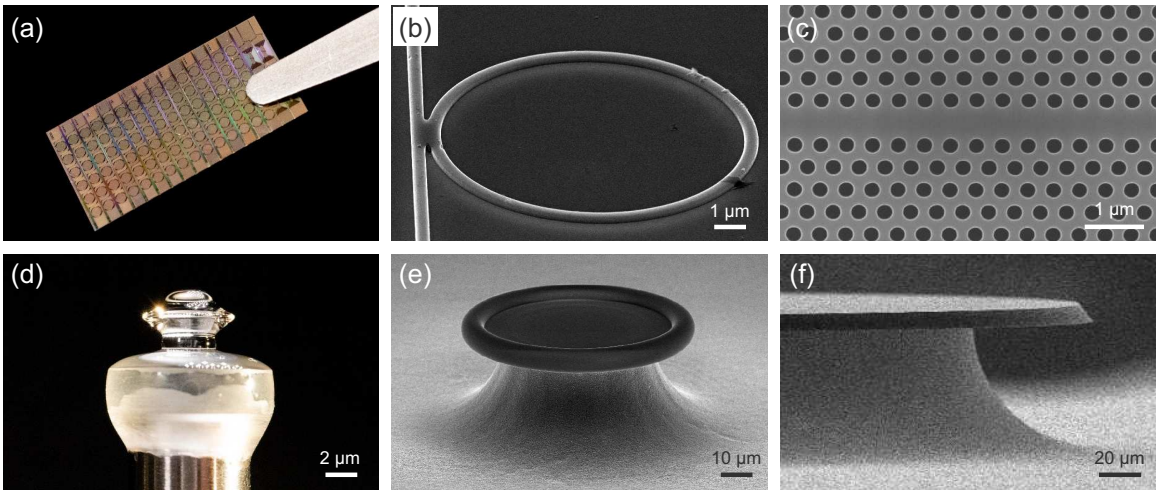

Fig. 2.1 Phographs of optical microresonators. (a) A waveguide-integrated Si_3N_4 ring, (b) an SEM image of a Si ring, and (c) a photonic crystal. Whispering-gallery-mode microresonators of (d) MgF_2 crystal, (e) SiO_2 microtoroid, and (f) SiO_2 microdisk.

of optical resonators, Fabry-Pérot resonators, ring resonators, photonic crystal resonators, and whispering-gallery-mode (WGM) microresonators are prominent designs, each offering distinct advantages and functionalities. Note that there are no significant differences between "resonator" and "cavity" in this thesis.

A Fabry-Pérot resonator, which is the most typical design, consists of two highly reflective mirrors forming a linear cavity, where light resonates when the optical path length matches an integer multiple of the wavelength. Due to their straightforward design, these resonators are widely used for spectral filtering, interferometry, and laser cavities. However, their linear geometry and relatively large mode volumes limit their compactness and scalability in integrated photonic systems.

Ring resonators (Fig. 2.1(a), (b)) come in various sizes, ranging from millimeter-scale fiber-based designs to micrometer-scale on-chip integrated photonic systems. Fiber ring resonators, constructed from optical fibers spliced into a closed loop, leverage the inherent flexibility, low loss, and compatibility of fiber optics, making them ideal for applications such as gyroscopes and optical delay lines. On the other hand, waveguide-integrated ring resonators are fabricated using CMOS-compatible processes that allow for precise control over the structure and resonant mode profiles. One key advantage of these processes is the simultaneous fabrication of the microresonator and the coupling waveguide, ensuring a stable coupling condition. However, the material options for CMOS-compatible fabrication are limited to silicon nitride (Si_3N_4), silicon (Si), high-index silica glass, aluminum nitride (AlN), aluminum gallium arsenide (AlGaAs), and diamond. This diversity in size and design

enables ring resonators to serve a wide range of photonic applications. However, their Q-factors are generally lower than those of whispering-gallery-mode (WGM) microresonators, limiting their performance in applications requiring ultra-high light confinement or enhanced nonlinear interactions.

Photonic crystal resonators (Fig. 2.1(c)) are another high-performance resonator class that confines light using the photonic bandgap effect. These structures are designed by introducing periodic variations in the refractive index of a material, creating bandgaps where certain wavelengths cannot propagate. A defect in this periodic structure acts as a resonant cavity, confining light within subwavelength volumes. Photonic crystal resonators are fabricated CMOS-compatible processes [36], and they can achieve Q-factors of $\sim 10^5$ and extremely small mode volumes, making them highly suitable for applications in cavity QED, quantum information processing, and biosensing [37].

WGM microresonators (Fig. 2.1(d)-(f)) operate based on total internal reflection along the curved surfaces of dielectric materials such as spheres, toroids, or disks. The term "whispering gallery" originates from an acoustic phenomenon found in St. Paul's Cathedral in London. Inside the cathedral's dome is a circular gallery encircled by a remarkably smooth stone wall. This gallery is famous for its unique acoustic effect, allowing a whispered voice from one side of the dome to be clearly heard by someone on the opposite side. Lord Rayleigh could explain this phenomenon by the continuous reflection of sound waves at the inner wall of the dome in 1910 [38]. In such a WGM, the input light propagates along the outer edge of the resonator, acting as a waveguide (Fig. 2.2). The refractive index contrast between the resonator material and its surroundings enables ultra-high Q-factors ($Q > 10^8$) and small mode volumes, making them highly efficient for light-matter interactions. These properties are ideal for nonlinear optics, soliton frequency comb generation, and cavity quantum electrodynamics (QED). WGM resonators can be fabricated using materials like silica (SiO_2), fluoride crystals, sapphire (Al_2O_3), polymers, and lithium niobate ($LiNbO_3$) through methods such as polishing and laser processing, allowing for flexibility in applications and integration [12, 39].

Resonance frequency

Optical microresonators have equidistant resonance frequencies (wavelength) determined by:

$$\omega_{\mathrm{m}} = \frac{2\pi mc}{nL}, \tag{2.1}$$

$$\lambda_{\mathrm{m}} = \frac{nL}{m}, \tag{2.2}$$

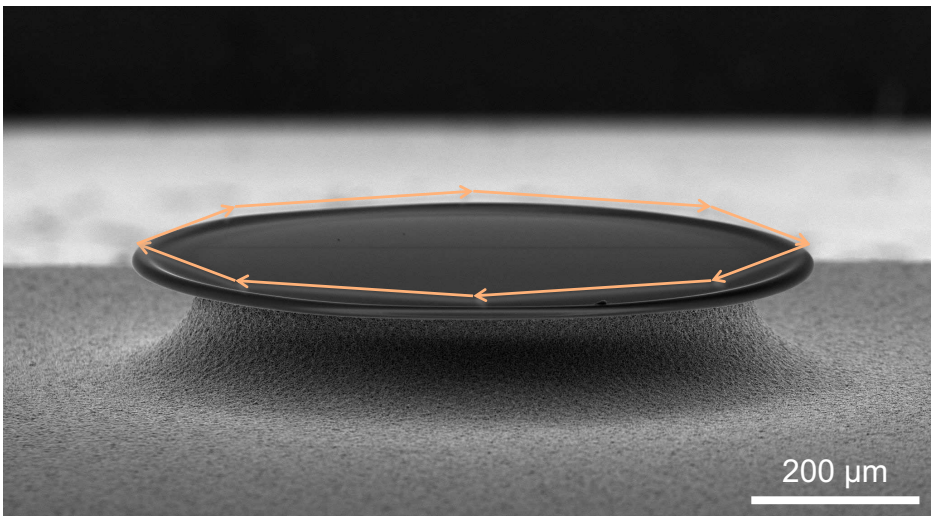

Fig. 2.2 (a) A schematic illustration of a light path in a circular whispering-gallery-mode on a toroidal microresonator with diameter of 800 μm.

where m is the mode number ($m \in \mathbb{N}$), ω_{m} (λ_{m}) is the angular frequency (wavelength) of the m-th mode, c is the speed of light, n is the refractive index, L is the cavity roundtrip length. The roundtrip time t_{R} is expressed as the inverse of the free-spectral range (FSR) of the resonator as

$$t_{\mathrm{R}} = \frac{1}{\mathrm{FSR}} = \frac{nL}{c}. \tag{2.3}$$

In the case of no dispersion, the effective refractive index does not depend on the frequency, and the resonance frequencies have an equal mode spacing D_1 ($D_1 = \omega_{\mathrm{m}}/m$).

Quality factor and cavity decay rate

The quality factor is an important parameter for evaluating the property of the resonator. Passing through a waveguide due to the material absorption and the scattering loss, the optical energy stored in the resonator ($U_{\mathrm{cav}}(t)$) decays exponentially:

$$U_{\mathrm{cav}}(t) = U_{\mathrm{cav}}(0)\exp(-\gamma t), \tag{2.4}$$

where γ is the cavity decay rate, which is related to the intrinsic cavity decay rate γ_{int} and the coupling rate to the external waveguide γ_{ext} ($\gamma = \gamma_{\mathrm{int}} + \gamma_{\mathrm{ext}}$). The quality factor is defined as

$$Q = 2\pi \cdot \frac{(\text{Intracavity optical energy})}{(\text{Energy loss per roundtrip})} = 2\pi \frac{U_{\mathrm{cav}}(t)}{-\frac{U_{\mathrm{cav}}(t)}{dt}\frac{2\pi}{\omega_0}} = \frac{\omega_0}{\gamma}. \tag{2.5}$$

The Q-factor is derived from the cavity decay rate in the time domain, corresponding to the full-width at half-maximum (linewidth) of the resonance mode in the frequency domain. The photon lifetime τ_p is defined as $\tau_p = \gamma^{-1}$ in the time domain. Therefore, the resonance linewidth can be directly measured from the resonator's transmission spectrum, while the cavity lifetime is measurable through time-domain measurements.

Effective mode area

One of the most attractive advantages of microresonators is that they confine light into a small area and volume. The effective mode area A_{eff} is determined by a resonant mode profile:

$$A_{\text{eff}} = \frac{(\int |E|^2 dA)^2}{\int |E|^4 dA}, \tag{2.6}$$

where $|E|^2$ corresponds to the light intensity and A is defined as the integral area. The effective mode volume is expressed as $V_{\text{eff}} = A_{\text{eff}} L$.

2.1.2 Cavity dispersion

Dispersion, a critical parameter in photonics, describes the dependence of phase velocity on frequency or propagation modes within a medium. Specifically, chromatic dispersion refers to the frequency or wavelength dependence of phase velocity, which arises from the frequency-dependent refractive index of the material and is influenced by the structural dispersion of the waveguide.

In microresonators, this phenomenon, known as cavity dispersion, encapsulates the dependence of the effective refractive index on frequency, resonance mode profiles, and polarization. Cavity dispersion is governed by both material and geometrical dispersions: material dispersion, dictated by the Sellmeier equation, defines the refractive index of the medium, while geometrical dispersion, which can be tailored by modifying the microresonator structure, depends on the spatial distribution of optical intensity. For instance, a significant evanescent field outside the microresonator reduces the effective refractive index. This interplay of material and structural properties makes dispersion a key factor in frequency comb generation, ultrafast optics, and the fundamental behavior of light propagation described by the frequency dependence of the propagation constant β as follows [40, 41]:

$$\begin{aligned} \beta(\omega) &= \frac{\omega}{c} n(\omega) \\ &= \beta_0 + (\omega - \omega_0)\beta_1 + \frac{1}{2}(\omega - \omega_0)^2 \beta_2 + \frac{1}{6}(\omega - \omega_0)^3 \beta_3 + \cdots, \end{aligned} \tag{2.7}$$

where ω is the angular frequency. Especially, the second-order dispersion β_2 of Eq. (2.7) represents the rate of change in the inverse group velocity in terms of frequency, which corresponds to group velocity dispersion (GVD) as follows:

$$\beta_2 = \left.\frac{d^2\beta}{d\omega^2}\right|_{\omega=\omega_0} = \frac{1}{c}\frac{d}{d\omega}\left(\frac{c}{v_\mathrm{g}}\right). \tag{2.8}$$

Here, v_g is the group velocity. β_2 plays an important role in nonlinear pulse propagation, such as broadening of the pulse bandwidth. In addition to the GVD parameter β_2, the dispersion parameter D is a useful expression, which is derived by the change of group delay time $T_\mathrm{g} = \beta_1 L$ in function to wavelength as,

$$D = \frac{1}{L}\frac{dT_\mathrm{g}}{d\lambda} = -\frac{2\pi c}{\lambda^2}\beta_2. \tag{2.9}$$

The choice of whether to use β_2 or D to represent GVD depends on the preferences within the research community. The parameters β_2 and D are expressed in units of $(\mathrm{ps}^2/\mathrm{km})$ and $(\mathrm{ps/km\cdot nm})$, respectively. Importantly, the signs of these two dispersion parameters are opposite: for normal dispersion, $\beta_2 > 0$ and $D < 0$, while for anomalous dispersion, $\beta_2 < 0$ and $D > 0$. It is also important to note that this definition of normal and anomalous dispersion refers to GVD at a specific wavelength. In the field of microresonator frequency combs, "dispersion" generally refers to GVD, and this thesis adopts the same convention.

As explained in 2.1.1, the resonance frequencies have equal mode spacings when cavity dispersion is not taken into account. However, cavity dispersion changes the mode spacings depending on the frequency. The resonance frequencies can be expressed with a relative mode number μ ($\mu \in \mathbb{Z}$) that is obtained from the absolute mode number m. The center mode number is $\mu = 0$, corresponding to the pump mode for optical frequency comb generation. The angular frequency ω_μ and the resonance frequency f_μ are expressed with Taylor-expanded equations:

$$\begin{aligned}\omega_\mu &= \omega_0 + D_1\mu + \frac{1}{2}D_2\mu^2 + \frac{1}{6}D_3\mu^3 + \cdots \\ &= \omega_0 + D_1\mu + D_\mathrm{int}(\mu),\end{aligned} \tag{2.10}$$

$$\begin{aligned}f_\mu &= f_0 + d_1\mu + \frac{1}{2}d_2\mu^2 + \frac{1}{6}d_3\mu^3 + \cdots \\ &= f_0 + d_1\mu + d_\mathrm{int}(\mu),\end{aligned} \tag{2.11}$$

where $D_1/2\pi$ is the equidistant resonator FSR in units of (Hz), $D_2/2\pi$ is the second-order dispersion related to β_2, and $D_3/2\pi$, $D_4/2\pi$, $\cdots$ represent the higher order dispersion. The integrated dispersion D_{int} is defined as the deviation of the resonance frequency, including all orders of dispersion from the equidistant grid of $D_1/2\pi$ (FSR).

Figure 2.3 provides a schematic illustration of microresonator dispersion. Higher-order dispersion terms can be neglected if the relationship $D_2 \gg D_3 \gg D_4 \cdots$ holds true, meaning the impact of each dispersion term decreases significantly.

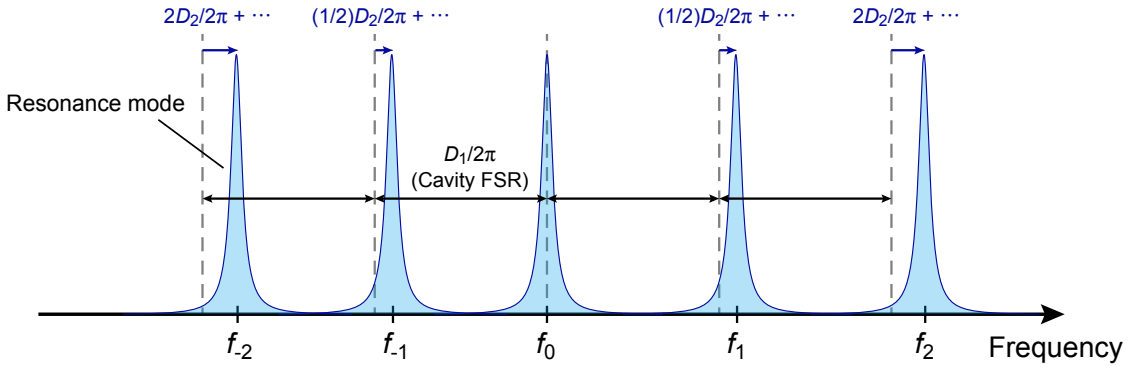

Fig. 2.3 Resonance frequencies taking dispersion into account. The mismatch between the equidistant comb grid (black dashed line) and the resonance mode (blue) corresponds to the microresonator dispersion.

2.1.3 Thermal effects in microresonators

Thermal effects play a significant role in the behavior and stability of microresonators, impacting optical coupling, resonance shift, and system performance. When light is stored inside a microresonator, thermal losses result in heating, which leads to a shift in the resonance frequency [42]. This thermal resonance shift arises from two primary mechanisms: the thermo-optic effect, where the refractive index changes with temperature (dn/dT), and thermal expansion, which alters the cavity length (dL/dT). These contributions combine to cause the resonance wavelength shift, expressed as:

$$\begin{aligned}\Delta\lambda_{\text{m}} &= \frac{(L+\Delta L)(n+\Delta n)}{m} - \frac{nL}{m} \\ &\approx \frac{nL}{m}\left(\frac{\Delta L}{L} + \frac{\Delta n}{n}\right) \\ &= \lambda_{\text{m}}\left(\frac{1}{L}\frac{dL}{dT}\Delta T + \frac{1}{n}\frac{dn}{dT}\Delta T\right),\end{aligned} \tag{2.12}$$

where ΔT is the induced temperature change of the resonator material.

At low input power, resonances maintain a Lorentzian shape, but at higher power levels, they become distorted and transition to a triangular shape. This phenomenon occurs because the scanning pump laser thermally pushes the resonance frequency from its original position until the laser crosses the shifted resonance, causing it to snap back. This behavior is particularly evident when the pump laser is swept from shorter to longer wavelengths, where stored light heats the resonator material.

Thermal effects can also be leveraged to stabilize optical coupling through a mechanism known as thermal locking. This passive locking technique uses the thermo-optic and thermal expansion effects to maintain coupling when the pump laser is blue-detuned relative to the resonance frequency. Many common microresonator materials, such as silica, MgF_2, and Si_3N_4, exhibit positive thermal coefficients for both the refractive index and cavity length. This positive sign ensures stable locking on the blue-detuned side but makes red-detuned coupling unstable. Since soliton microcomb generation requires red-detuned pumping, thermal instability becomes a challenge for soliton formation.

In cases where the thermal coefficients of the material have opposite signs [43], as seen in materials like PDMS-coated SiO_2, CaF_2, and BaF_2, thermal self-oscillation can occur. This oscillatory behavior complicates the use of passive thermal locking, necessitating external locking mechanisms to stabilize the optical coupling. Despite these challenges, thermal effects remain integral to the operation and control of microresonators, providing both opportunities and limitations for advanced photonic applications.

2.1.4 Optical nonlinear processes in microresonators

Third order nonlinearities

Optical nonlinear processes indicate that the polarization P in dielectric materials scales nonlinearly with externally applied electric fields E, represented by the following relation:

$$P = \varepsilon_0\{\chi^{(1)}E + \chi^{(2)}E^2 + \chi^{(3)}E^3 + \cdots\}. \tag{2.13}$$

Here ε_0 is the vacuum permittivity, $\chi^{(1)}$ is the linear electric susceptibility and $\chi^{(2)}$ and $\chi^{(3)}$ are the second and third order nonlinear electric susceptibilities, respectively. While higher-order terms can be ignored when electric field amplitudes are low, they become dominant in strong electric fields. The second order term works in dielectric materials that are inversion asymmetric at the molecular level. The nonlinear contribution takes account of only the third order term because of using SiO_2 that are symmetric molecules. The third order nonlinearity

can occur in all dielectric materials. Therefore, the polarization contributed by nonlinearity, P_{NL}, can be extracted from Eq. (2.13):

$$P_{\mathrm{NL}} = \varepsilon_0 \chi^{(3)} E^3. \tag{2.14}$$

Since the third order nonlinear process interacts between four electric field components, the total electric field is described as

$$E = \sum_{j=1}^{4} E_j \exp\{i(k_j z - \omega_j t)\} \ . \tag{2.15}$$

Substituting Eq. (2.15) into Eq. (2.14) yields the following equation.

$$P_{\mathrm{NL}} = \sum_{j=1}^{4} P_j \exp\{i(k_j z - \omega_j t)\} \ . \tag{2.16}$$

P_{j} has a large number of terms, including three electric field components such as

$$\begin{aligned} P_4 \propto \{ & |E_4|^2 E_4 + 2(|E_1|^2 + |E_2|^2 + |E_3|^2) E_4 \\ & + 2E_1 E_2 E_3 \exp(i\theta_+) + 2E_1 E_2 E_3^* \exp(i\theta_-) + \cdots \} \ , \end{aligned} \tag{2.17}$$

where θ_+ and θ_- are expressed as

$$\begin{aligned} \theta_+ &= (k_1 + k_2 + k_3 - k_4) z - (\omega_1 + \omega_2 + \omega_3 - \omega_4) t, \\ \theta_- &= (k_1 + k_2 - k_3 - k_4) z - (\omega_1 + \omega_2 - \omega_3 - \omega_4) t. \end{aligned} \tag{2.18}$$

In Eq. (2.13), the components proportional to E_4 denote self-phase modulation (SPM) and cross-phase modulation (XPM). The term with θ_+ represents frequency conversion processes of THG and sum frequency generation. Additionally, the term with θ_- denotes the frequency conversion processes of FWM.

Self-phase modulation and cross-phase modulation

SPM and XPM are phenomena to change an effective refractive index in dielectric materials, whose shift depends on the propagating light intensity [40]. SPM refers to the self-induced phase shift caused by the interaction of one optical field. XPM, on the other hand, refers to the phase shift induced by a separate optical field that has a different frequency, direction, polarization, or transverse mode. The change in effective refractive index due to SPM and XPM is usually smaller than that caused by thermal effects, as expressed in Eq. (2.12).

Therefore, the resonance shift is primarily attributed to thermal effects. In contrast, the response time of SPM and XPM (on the order of nanoseconds or less) is significantly faster than that of thermal effects (on the order of microseconds). For example, in Eq. (2.17), $|E_4|^2E_4$ and $2(|E_1|^2+|E_2|^2+|E_3|^2)E_4$ represent SPM and XPM, respectively. Since XPM effects work twice as much as SPM effects, change of the effective refractive index $\Delta n(t)$ is expressed as

$$\Delta n(t) = n_2 I_4(t) + 2n_2\{I_1(t)+I_2(t)+I_3(t)\}, \tag{2.19}$$

where n_2 is the nonlinear refractive index and I_* is the light intensity ($* \ni 1-4$). Assuming the case that a microresonator is pumped with a CW laser, the wavelength shift via SPM is as follows

$$\Delta\lambda_m = \frac{(n+\Delta n)L}{m} - \frac{nL}{m} = \frac{n_2 I_4 L}{m} = \frac{n_2 P_{\mathrm{cav}} L}{m A_{\mathrm{eff}}} = \lambda_m \frac{n_2 P_{\mathrm{cav}}}{n A_{\mathrm{eff}}}\ , \tag{2.20}$$

where the second term on the right-hand side in Eq. (2.19) is neglected because the term represents XPM effects.

Four-wave mixing

Four-wave mixing (FWM) is a nonlinear optical process in which two photons are annihilated and two new photons are generated, obeying energy conservation as [44]

$$\begin{aligned} \hbar\omega_1 + \hbar\omega_2 &= \hbar\omega_3 + \hbar\omega_4 \quad \text{(non-degenerate)}, \\ 2\hbar\omega_1 &= \hbar\omega_3 + \hbar\omega_4 \quad \text{(degenerate)}. \end{aligned} \tag{2.21}$$

When the annihilated photons have different frequencies, the process is called non-degenerate FWM; if they share the same frequency, it is referred to as degenerate FWM. Both processes require a phase-matching condition of $k_1 + k_{2(1)} = k_3 + k_4$, as shown in Eq. (2.18). In particular, degenerate FWM can arise in the anomalous dispersion regime through modulation instability. The threshold input power for zero detuning in a coupling waveguide is given by

$$P_{\mathrm{in}}^{\mathrm{FWM}} \approx \frac{\gamma_{\mathrm{NL}}^2 n^2 A_{\mathrm{eff}} L}{8c\omega_0 n_2 \eta}\ . \tag{2.22}$$

Here, γ_{NL} represents the nonlinear coefficient. In essence, a microcomb is typically initiated by degenerate FWM triggered by a continuous-wave (CW) pump laser. This degenerate FWM process generates equally spaced sidebands around the pump frequency, marking the onset of the comb formation (Fig. 2.4(a)).

Stimulated Raman scattering

Stimulated Raman scattering (SRS) is an optical nonlinear process in which pump photons generate red-shifted photons by interacting with molecular vibrations of the host material. The amount of frequency shift, denoted (Ω_{SRS}), depends on the properties of the resonator material. For instance, in silica, Ω_{SRS} is approximately 14 THz. The threshold input power in a coupling waveguide under zero-detuning conditions can be expressed as

$$P_{\mathrm{in}}^{\mathrm{SRS}} \approx \frac{\gamma_{\mathrm{NL}}^2 n^2 A_{\mathrm{eff}} L}{4c^2 \eta g_{\mathrm{R(max)}}}, \tag{2.23}$$

where $g_{\mathrm{R(max)}}$ is the maximum Raman gain (in units of m/W). For example, silica at 1550 nm has $g_{\mathrm{R(max)}} = 6.2 \times 10^{-14}$ m/W. Because microresonators offer both high-Q factors and small mode volumes, they can achieve exceptionally low threshold powers for Raman lasing [45, 46].

Despite these advantages, the broadband nature of Raman gain makes it challenging to fully suppress SRS in many microcomb experiments, except in systems using very small microresonators or materials with narrow Raman gain spectra. Figure 2.4(b) illustrates how a Raman comb can form within a microresonator due to the material's broad Raman gain profile. In silica microresonators operating under anomalous dispersion, FWM typically has a lower threshold than SRS, as reflected in the ratio

$$\frac{P_{\mathrm{in}}^{\mathrm{SRS}}}{P_{\mathrm{in}}^{\mathrm{FWM}}} \approx \frac{(2\omega_0 n_2)}{(c g_{\mathrm{R(max)}})} \approx 2.9, \tag{2.24}$$

indicating that FWM is likely to occur before any substantial SRS takes place. Conversely, in normal-dispersion regions, FWM is impeded by the lack of modulation instability, and SRS can become the dominant nonlinear process.

Stimulated Brillouin scattering

Stimulated Brillouin scattering (SBS) is an optical nonlinear process in which pump photons generate red-shifted photons propagating in the backward direction through interaction with acoustic waves [40]. The frequency shift (Ω_{SBS}) depends on the resonator material; for example, silica typically exhibits a Brillouin shift of about 11 GHz. When the waveguide is assumed to be at zero detuning, the threshold input power for SBS is given by

$$P_{\mathrm{in}}^{\mathrm{SBS}} \approx \frac{\gamma_{\mathrm{NL}}^2 n^2 A_{\mathrm{eff}} L}{4c^2 \eta g_{\mathrm{B}}}, \tag{2.25}$$

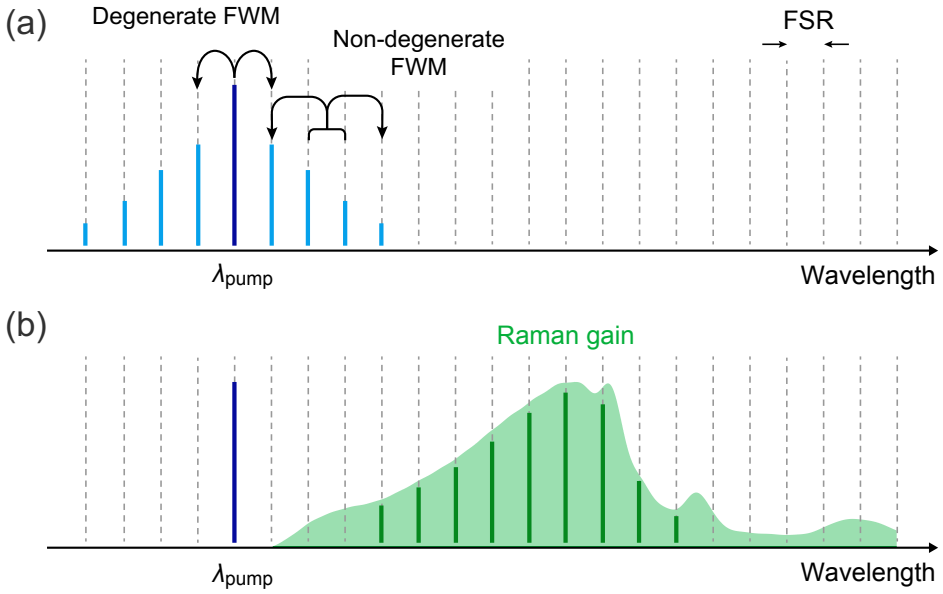

Fig. 2.4 Illustrations of microcomb formation via (a) FWM and (b) SRS. Since FWM needs to satisfy a phase-matching condition, a microcomb via FWM can be mutually coherent. On the other hand, basically, a microcomb via SRS is mutually incoherent because SRS does not require a phase-matching condition.

where g_{B} is the Brillouin gain in units of m/W ($\sim 6 \times 10^{-11}$ m/W in silica at 1550 nm). Because the Brillouin gain can be on the order of three magnitudes larger than the Raman gain, SBS often dominates over SRS in conventional silica optical fibers.

In optical microresonators, however, SBS requires resonator modes that coincide with the Brillouin gain spectrum. As a result, SBS typically does not interfere with microcomb operation except in specific cases—for instance, when the resonator is sufficiently large that its FSR falls below Ω_{SBS} (e.g., a diameter exceeding approximately 6 mm in silica). This arises from the fact that the Brillouin gain spectrum in dielectric materials is usually narrower than 100 MHz, which is smaller than the FSR of most microresonators.

On the other hand, by carefully engineering microresonator structures, one can design high-Q resonators that support Brillouin laser generation at low threshold powers [47–49]. Through appropriate choices of resonator size, geometry, and material, SBS-based lasing can thus be harnessed for applications such as narrow-linewidth light sources, without necessarily disrupting Kerr-comb or other nonlinear processes.

2.1.5 Optical coupling to microresonators

Coupled mode equation

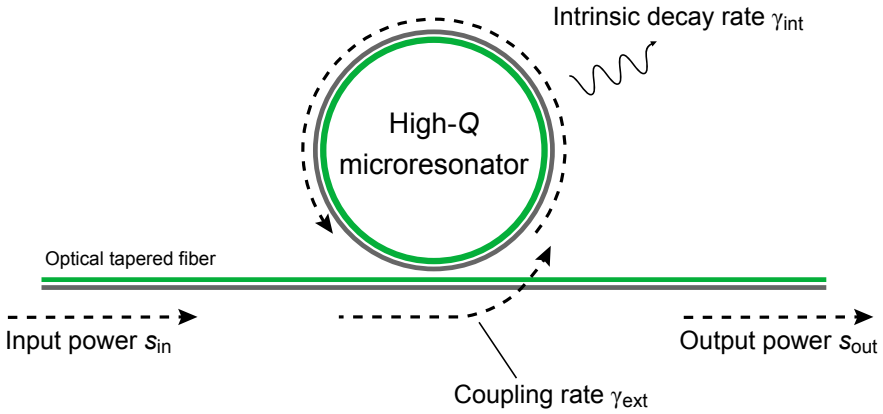

Fig. 2.5 Optical coupling system between a microresonator and a coupling waveguide. s_{in} and s_{out} are the input and output fields, respectively. γ_{int} and γ_{ext} are the intrinsic decay and coupling rates, respectively.

A coupled mode equation describes an optical coupling between a resonator and an external coupler through an evanescent field, as shown in Fig. 2.5. When adopting slowly varying envelope approximation, the time evolution of a light field $A_0(t)$ at the resonance frequency ω_0 can written as [50]

$$\frac{dA_0(t)}{dt} = -\frac{\gamma}{2}A_0(t) - j\omega_0 A_0(t) + \sqrt{\gamma_{ext}}s_{in}(t)\exp(-j\omega_p t), \tag{2.26}$$

where s_{in} is the driving field and ω_p is the pump frequency. The decay rate γ is given by $\gamma = \gamma_{int} + \gamma_{ext}$. It is noted that the field amplitude $A_0(t)$ is normalized to the number of intracavity photons at the resonance as $|A_0(t)|^2$. Here, Eq.(2.26) can be rewritten by adopting the phase transformation ($a_0(t) = A_0(t)\exp(j\omega_p t)$) as follows,

$$\frac{da_0(t)}{dt} = -\left(\frac{\gamma}{2} + j(\omega_0 - \omega_p)\right)a_0(t) + \sqrt{\gamma_{ext}}s_{in}(t). \tag{2.27}$$

When we assume the steady state ($da_0(t)/dt = 0$), the amplitude is expressed as,

$$a_0 = \frac{\sqrt{\gamma_{ext}}}{\gamma/2 + j(\omega_0 - \omega_p)}s_{in}, \tag{2.28}$$

$$|a_0|^2 = \frac{\gamma_{ext}}{\gamma^2/4 + (\omega_0 - \omega_p)^2}|s_{in}|^2. \tag{2.29}$$

In addition, the relation between the input field and the output field is described as

$$s_{\text{out}} = -s_{\text{in}} + \sqrt{\gamma_{\text{ext}}} a_0, \tag{2.30}$$

and the transmittance can be defined as follows:

$$t = \frac{s_{\text{out}}}{s_{\text{in}}} = \frac{(\gamma_{\text{ext}} - \gamma_{\text{int}})/2 - j(\omega_0 - \omega_{\text{p}})}{(\gamma_{\text{ext}} + \gamma_{\text{int}})/2 + j(\omega_0 - \omega_{\text{p}})}, \tag{2.31}$$

$$T = \left| \frac{s_{\text{out}}}{s_{\text{in}}} \right|^2 = \frac{(\gamma_{\text{ext}} - \gamma_{\text{int}})^2/4 + (\omega_0 - \omega_{\text{p}})^2}{(\gamma_{\text{ext}} + \gamma_{\text{int}})^2/4 + (\omega_0 - \omega_{\text{p}})^2}. \tag{2.32}$$

When zero detuning condition ($(\omega_0 - \omega_{\text{p}}) = 0$), the maximum dip of transmission T_0 is expressed as,

$$T_0 = \left(\frac{Q_{\text{int}} - Q_{\text{ext}}}{Q_{\text{int}} + Q_{\text{ext}}} \right)^2. \tag{2.33}$$

Here, $T_0 = 0$, which indicates that full extinction of transmittance happens at the critical coupling condition, $Q_{\text{int}} = Q_{\text{ext}}$ ($\gamma_{\text{int}} = \gamma_{\text{ext}}$), and then the loaded Q becomes half of the intrinsic and coupling Q ($Q_{\text{total}} = Q_{\text{int}}/2 = Q_{\text{ext}}/2$). The optical coupling condition is categorized into three conditions:

$$\begin{aligned} \text{under coupling} &: Q_{\text{int}} < Q_{\text{ext}} (\gamma_{\text{int}} > \gamma_{\text{ext}}), \\ \text{critical coupling} &: Q_{\text{int}} = Q_{\text{ext}} (\gamma_{\text{int}} = \gamma_{\text{ext}}), \\ \text{over coupling} &: Q_{\text{int}} > Q_{\text{ext}} (\gamma_{\text{int}} < \gamma_{\text{ext}}). \end{aligned} \tag{2.34}$$

When the coupling ratio is defined as $\eta = \gamma_{\text{ext}}/\gamma_{\text{int}}$, Fig. 2.6 shows the minimum transition for different coupling rates and the corresponding normalized transmission. The coupling ratio can generally be controlled by changing the gap between the resonator and the waveguide.

Measuring the Q-factor

The Q-factor is an important parameter to evaluate whether the microresonator could build up intracavity optical power and cause optical nonlinear effects. The Q-factor is determined by using the cavity decay rate following Eq. (2.5), which can be evaluated by measuring the linewidth of a resonance mode in the frequency (wavelength) domain and the photon lifetime in the time domain. Figure 2.7(a) shows the tapered fiber coupling setup to measure Q-factors. A microresonator is placed on a three-axis automatic positioning stage that can control the relative position between the microresonator and fiber. The coupling position is monitored by using microscopes from the top and side. Figure 2.7(b) and (c) shows experimental setups

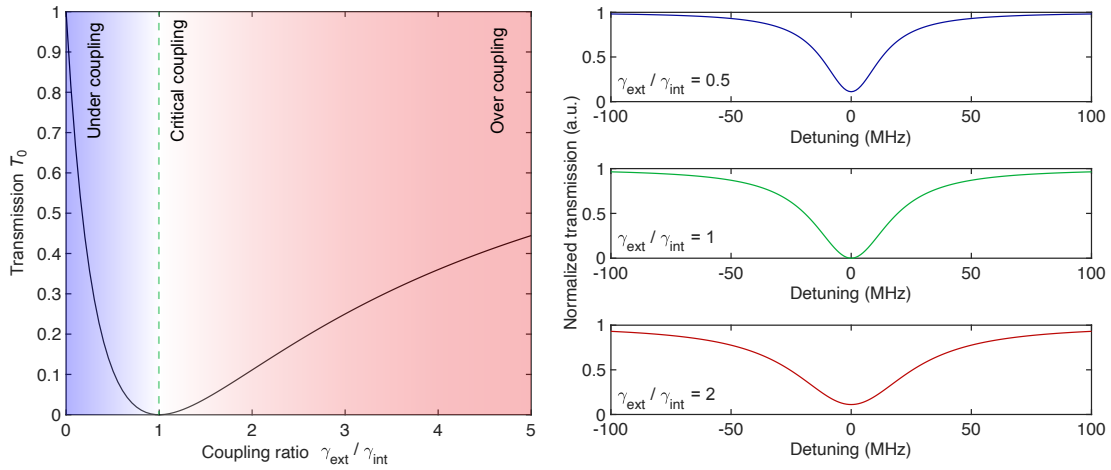

Fig. 2.6 (a) Transmission T_0 for different coupling ratio $\gamma_{ext}/\gamma_{int}$. (b) Calculation results of transmission in three different coupling ratios.

used for Q-factor measurement in the frequency domain. Figure 2.8 shows measurement results with a silica toroid.

As explained in §2.1.1, the transmission in a resonance mode has a Lorentzian shape as a function of the detuning between the resonance and laser frequencies. Therefore, the linewidth of a resonance mode can be evaluated by monitoring the transmission while scanning the laser frequency. Here the frequency (wavelength) axis needs to be calibrated with some frequency (wavelength) marker, that are created by using the built-in function of a commercial laser (Santec TSL-510 and TSL-710), a fiber Mach-Zehnder interferometer (MZI). For example, Fig. 2.8(a) shows measured resonance modes with 20 MHz sine wave modulated by MZI. A Q-factor is determined as $Q = \omega_0/\gamma$ $(= \lambda_0/\Delta\lambda)$, where λ_0 is the resonance wavelength and $\Delta\lambda$ is the linewidth in the wavelength domain.

For high-Q cavities exceeding Q of 10^8 (corresponding to the long photon lifetime), the ring-down method is also used for Q measurement. When the input is suddenly interrupted, the stored optical energy decays exponentially over time. The optical intensity inside the cavity $I(t)$ decays exponentially:

$$I(t) = I_0 \exp(-t/\tau_p), \tag{2.35}$$

where I_0 and τ_p are the initial intensity and the photon lifetime ($\tau_p = 1/\gamma$), respectively. Since the Q-factor is related to τ_p by Eq. (2.5), we can calculate Q by measuring τ_p. Fig. 2.8(b) shows the result of the Q-factor measurement using the ring-down method, indicating a Q of 6×10^8 for a 200-μm-diameter microtoroid.

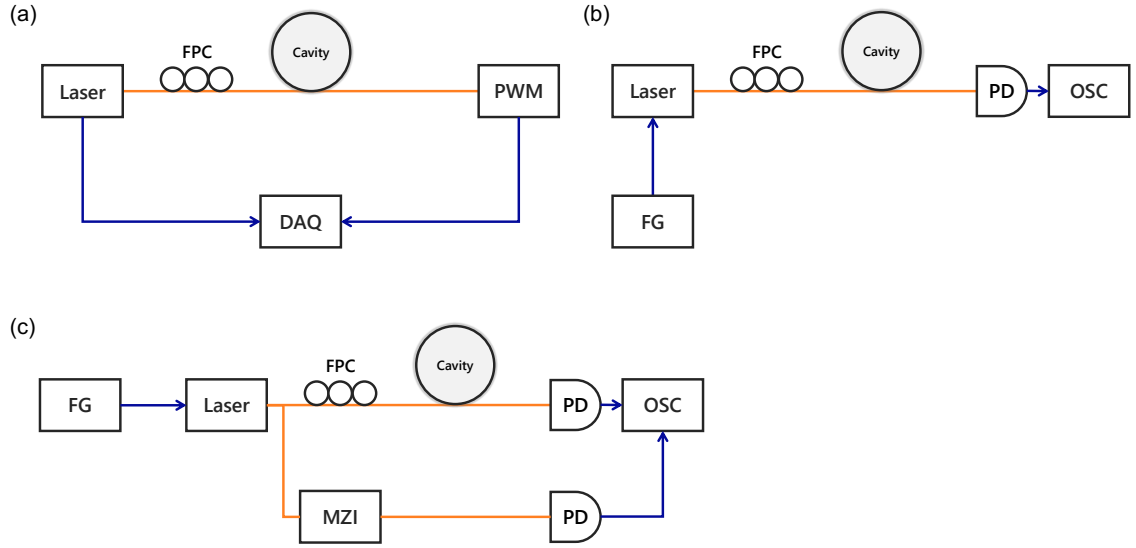

Fig. 2.7 Experimental setups for Q measurement in frequency domain. The orange lines indicate optical paths, and the blue lines indicate electrical paths. FPC, fiber polarization controller; PWM, power meter; DAQ, data acquisition; FG, function generator; PD, photodiode; OSC, oscilloscope; MZI, fiber Mach-Zehnder interferometer.

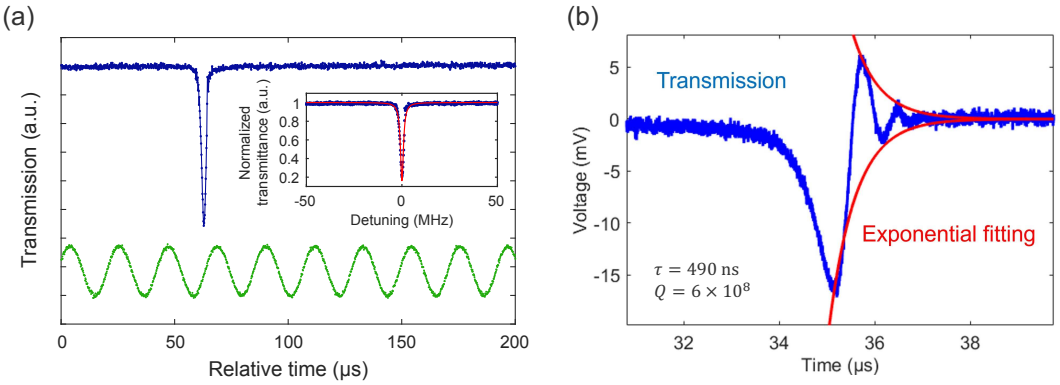

Fig. 2.8 (a) Q-factor measurement in the frequency domain. The blue dots and green dots represent the experimental data. The frequency axis is calculated by using fiber MZI spectrum with 20 MHz of FSR. The red line is a fitted curve by the Lorentzian function. (b) Measurement result by using cavity ring-down method in the time domain. The blue line represents the transmission signal, and the red line is the fitted curve, respectively. The calculated τ_p is 490 ns, yielding the Q-factor of 6×10^8.

2.2 Microcomb generation

2.2.1 Optical frequency combs in microresonators

A microcomb is generated in a microresonator via cascaded FWM driven by a CW pump laser through an external waveguide. The commonly used method is to scan the pump frequency over the resonance mode to the lower side. The pump scanning changes the intracavity conditions from the CW state: Turing pattern and chaotic combs with blue-detuned pumping; breather soliton, multi-soliton, and single soliton combs with red-detuned pumping [15]. The general formation and properties of microcombs are shown using an LLE (detailed in Chapter 4).

The first sidebands of a microcomb are generated via degenerate FWM driven by a CW pump laser. Degenerate FWM generates in anomalous dispersion regime with modulation instability that amplifies amplitude noises of the coupled CW laser in the time domain. Also, in the frequency domain, the CW laser is coupled to a resonance mode at the blue-detuned side and generates sidebands at the centers of resonance modes. The mode number offsets μ_{th}, where first sidebands generate, are determined by as follows [51, 52]:

$$-\Delta\omega_0 + \frac{1}{2}D_2\mu_{\mathrm{th}}^2 \approx 0 \,, \tag{2.36}$$

when reaching the intracavity power to the threshold for degenerate FWM. To satisfy with Eq. (2.36), the blue-detuned pumping ($\Delta\omega_0 = \omega_{\mathrm{p}} - \omega_0 > 0$) is required in anomalous dispersion regime ($D_2 > 0$). The threshold intracavity power for degenerate FWM $P_{\mathrm{cav}}^{\mathrm{FWM}}$ can be expressed as

$$P_{\mathrm{cav}}^{\mathrm{FWM}} = \frac{\gamma_{\mathrm{NL}} n A_{\mathrm{eff}}}{2\omega_0 n_2} \,, \tag{2.37}$$

by using Eq. (2.22) and the relation between input power P_{in} and intracavity power P_{cav}:

$$P_{\mathrm{cav}} = \frac{\gamma_{\mathrm{ext}}}{\frac{1}{4}\gamma_{\mathrm{NL}}^2 + \Delta\omega_0^2}\frac{D_1}{2\pi}P_{\mathrm{in}} \,. \tag{2.38}$$

Therefore, the pump detuning to generate the first sidebands can be calculated as

$$\Delta\omega_0 = \sqrt{\frac{2c\omega_0 n_2}{n^2\eta A_{\mathrm{eff}} L}P_{\mathrm{in}} - \frac{1}{4}\gamma_{\mathrm{NL}}^2} \,. \tag{2.39}$$

In a case with a normal dispersion regime, the lack of modulation instability obstructs the creation of degenerate FWM, which is a trigger for the formation of a microcomb. However, when mode coupling between different transverse modes in a microresonator (or

between different transverse modes in two microresonators) shifts a resonance frequency that effectively creates anomalous dispersion, the first sidebands can oscillate at the shifted resonance mode [53]. As a result of the microcomb formation, microresonators with normal dispersion can generate a mode-locked pulse that propagates as a dark soliton pulse [54, 55].

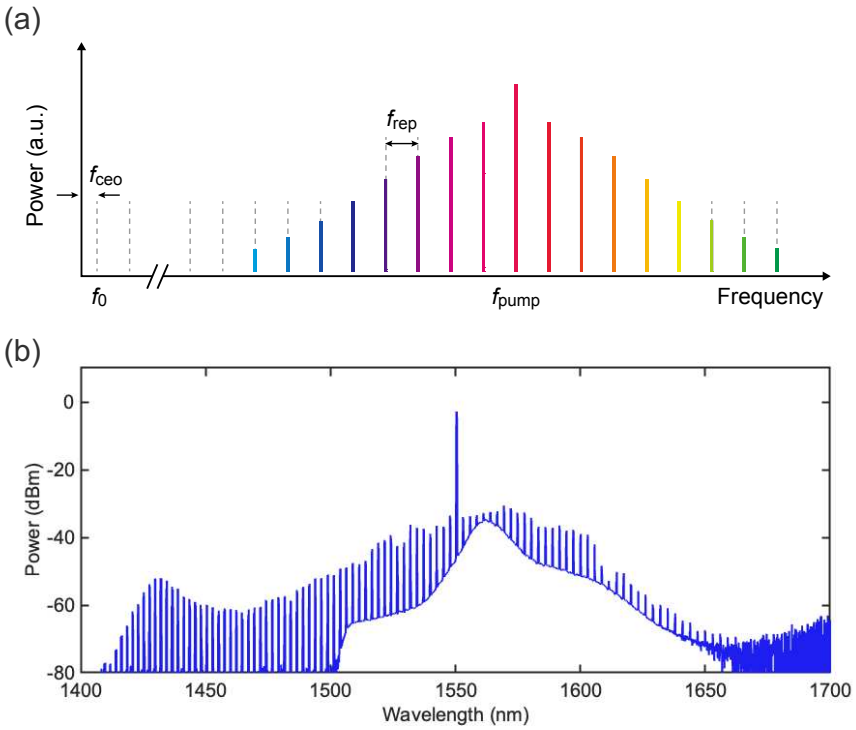

Fig. 2.9 (a) A schematic spectrum of microcomb in the frequency domain. The comb spectrum and the pulse train can be mathematically converted by Fourier transform, which means that properties such as bandwidth and mode spacing are characterized by a one-by-one relationship. (b) Microcomb generation in a silica microtoroid which has $Q = 4 \times 10^8$ and a cavity FSR of around 220 GHz. The ASE noise of EDFA is not filtered out.

An optical frequency f_{m} of frequency comb is defined as,

$$f_{\mathrm{m}} = f_{\mathrm{ceo}} + \mathrm{m} f_{\mathrm{rep}}, \tag{2.40}$$

where m is the integer, f_{ceo} and f_{rep} represent the carrier envelope offset frequency and repetition frequency, respectively. The pulse repetition equals the frequency spacing of comb lines, namely the cavity FSR. The offset frequency f_{ceo} can be interpreted as the frequency of the "first" comb line. The repetition frequency f_{rep} is directly measurable with a fast photodetector because the RF beatnote of the overall frequency comb gives the information of f_{rep}. On the other hand, the f_{ceo} measurement is a challenge since it does not appear in

the beat signal. However, it has been possible to determine f_{ceo} when the comb bandwidth exceeds one octave by means of the useful method referred to as f-$2f$ self-referencing. The lower frequency of the octave-spanning comb f_{n} is converted to a doubled frequency $2f_{\mathrm{n}}$ via second-harmonic generation. When the harmonic light and filtered higher frequency $f_{2\mathrm{n}}$ are mixed with a photodiode, the beat signal corresponds to the f_{ceo} as,

$$2f_{\mathrm{n}} - f_{2\mathrm{n}} = 2(f_{\mathrm{ceo}} + nf_{\mathrm{rep}}) - (f_{\mathrm{ceo}} + 2nf_{\mathrm{rep}}) = f_{\mathrm{ceo}} \ . \tag{2.41}$$

The frequency comb is usually stabilized by locking these two frequencies to an external reference clock for frequency stability and accuracy.

2.2.2 Microcomb formation dynamics

Microcomb formation can be analyzed using two primary theoretical frameworks: one is the spectrotemporal model, which employs a set of nonlinear coupled-mode equations to track the evolution of each comb line in the frequency domain [56, 57], and the other is the spatiotemporal model, where the intracavity field is computed as a function of azimuthal angle and time via the Lugiato–Lefever Equation (LLE) [58, 59]. While the spectrotemporal model provides insight by directly tracking mode amplitudes, it can be computationally demanding when the number of comb lines grows large. In contrast, the LLE-based spatiotemporal model captures the key physics of comb generation in a single partial differential equation and thus often offers greater computational efficiency.

Here, we can describe soliton formation and microcomb dynamics in a high-Q microresonator using the LLE. The LLE treats the intracavity field in multiple resonance modes $a(\phi,t)$ as a function of the angular coordinate ϕ and the slow time t. By imposing a periodic boundary condition $(\phi,t) = a(\phi + 2\pi,t)$, it is possible to model the resonator circumference as a continuous spatial dimension. The intracavity field $a(\phi,t)$ relates to the optical field of μ-th comb mode $a_\mu(t)$ by a discrete Fourier transform,

$$a(\phi,t) = \sum_{\mu} a_\mu(t) \exp(i\mu\phi) \ . \tag{2.42}$$

Eq. (2.42) is differentiated by a nonlinear coupled-mode equation [58] as

$$\begin{aligned}\frac{\partial a(\phi,t)}{\partial t} &= \sum_{\mu}\frac{\partial a_{\mu}(t)\exp(i\mu\phi)}{\partial t} \\ &= -\frac{\gamma}{2}a_{\mu}\exp(i\mu\phi) - i\delta_{\mu=0}\sum_{\mu}a_{\mu}\exp(i\mu\phi) - i\sum_{\mu}D_{\text{int}}a_{\mu}\exp(i\mu\phi) \\ &\quad + \sqrt{\gamma_{\text{ext}}}a_{\text{in}} + ig\sum_{\mu}\sum_{\mu_1,\mu_2}a_{\mu_1}a_{\mu_2}a^{*}_{\mu_1+\mu_2-\mu}\exp(i\mu\phi)\ .\end{aligned} \tag{2.43}$$

Here, δ_{μ} is the Kronecker delta function to validate the driving field (i.e., $\delta_{\mu}=1$ for $\mu=0$), g is the Kerr nonlinear coefficient given as $(\hbar\omega_0^2 c n_2)/(n_0^2 V_{\text{eff}})$. The last term on the right-hand side represents Kerr effects, including SPM, XPM, and FWM. The requirement of energy conservation to satisfy the relation $\mu=\mu_1+\mu_2-\mu_3$. Equation (2.43) can be simplified using Eq. (2.42) as,

$$\frac{\partial a(\phi,t)}{\partial t} = -\left(\frac{\gamma}{2}+i\delta_{\mu=0}\right)a - i\sum_{k\geq 2}\frac{D_k}{k!}\left(\frac{\partial}{i\partial\phi}\right)^{k}a + ig|a|^2 a + \sqrt{\gamma_{\text{ext}}}a_{\text{in}}\ . \tag{2.44}$$

Equation (2.44) is a LLE, which can describe microcomb dynamics.

An LLE can be calculated, incorporating Kerr effects as well as stimulated Raman scattering. Kerr effects happen instantaneously, while the response of Raman effects is delayed compared to the carrier light field. Therefore, the responses of Kerr and Raman effects need to be calculated using integral calculus as a function of the angular coordinate, which is related to the fast time domain in the microresonator. The response function of Kerr and Raman effects $h(\tilde{t})$ can be expressed as

$$h(\tilde{t}) = (1-f_{\text{R}})\delta(\tilde{t}) + f_{\text{R}}h_{\text{R}}(\tilde{t})\ , \tag{2.45}$$

where $\tilde{t}$, f_{R}, and $h_{\text{R}}(\tilde{t})$ are the fast time frame, the Raman retribution coefficient ($f_{\text{R}}=0.18$ in silica), and the Raman response function which is normalized as $\int_0^{\infty}h_{\text{R}}(\tilde{t})d\tilde{t}=1$, respectively. $\delta(\tilde{t})$ is the Kronecker delta function ($\delta(\tilde{t})=1$ at $\tilde{t}=0$). Hence, an LLE that can rewrite taking account of Raman effects as follows:

$$\begin{aligned}\frac{\partial a(\phi,t)}{\partial t} &= -\left(\frac{\gamma}{2}+i\delta_{\mu=0}\right)a - i\sum_{k\geq 2}\frac{D_k}{k!}\left(\frac{\partial}{i\partial\phi}\right)^{k}a \\ &\quad + iga\int_0^{2\pi}h\left(\frac{\phi'}{D_1}\right)\left|a(\phi-\phi')\right|^2 d\phi' + \sqrt{\gamma_{\text{ext}}}a_{\text{in}}\ .\end{aligned} \tag{2.46}$$

2.2.3 Microcomb formation and the states

A microcomb is generated in a microresonator through cascaded FWM, driven by a CW pump laser coupled via an external waveguide. The typical method involves scanning the pump frequency across the resonance mode toward the lower frequency side. This pump scanning modifies the intracavity conditions, transitioning through various states: Turing patterns and chaotic combs appear with blue-detuned pumping, while breather solitons, multi-solitons, and single solitons emerge with red-detuned pumping.

Using the LLE, we can provide an overview of the general formation and properties of microcomb. Figure 2.10 shows simulation results of microcomb formation as a function of pump detuning, calculated using Eq. (2.44). Initially, the CW pump laser builds up intracavity power, triggering degenerate FWM that generates a Turing pattern comb (or primary comb). This comb exhibits evenly spaced modes due to pure FWM. As pump detuning progresses, a chaotic comb, which is also called a modulation instability (MI) comb, forms. In this state, sub-comb lines are independently generated from each primary comb line, resulting in overlapping modes. This overlap leads to multiple laser lines within a single resonance mode, causing amplitude noise in the microcomb. When the pump detuning shifts from blue to red, the intracavity field transitions into a mode-locked state, where the microcomb propagates as soliton pulses within the microresonator. As shown in Fig. 2.10(a), soliton states exhibit discrete intracavity power levels corresponding to the number of soliton pulses. These step-like transitions in power are referred to as "soliton steps" or "soliton access range." However, soliton steps are typically observed for only a few microseconds in the time domain due to the strong thermal effects induced by the resonator material. Therefore, as described in the next section, various methods for soliton generation have been developed.

2.2.4 Advances in soliton microcomb generation

Soliton microcombs are a transformative development in photonics, enabling applications ranging from precision spectroscopy and optical communication to frequency metrology and distance ranging. These devices rely on microresonators to generate coherent optical frequency combs, with soliton states representing the most desirable operational regime due to their low noise, high coherence, and robust spectral properties. However, achieving soliton formation in microresonators presents substantial technical challenges associated with thermal effects, dispersion management, and nonlinear optical dynamics.

The primary difficulty in soliton generation stems from the inherent thermal instability of the microresonator. During soliton formation, the pump laser induces thermal effects as it heats the microresonator, shifting the resonator's resonance frequency. This frequency shift

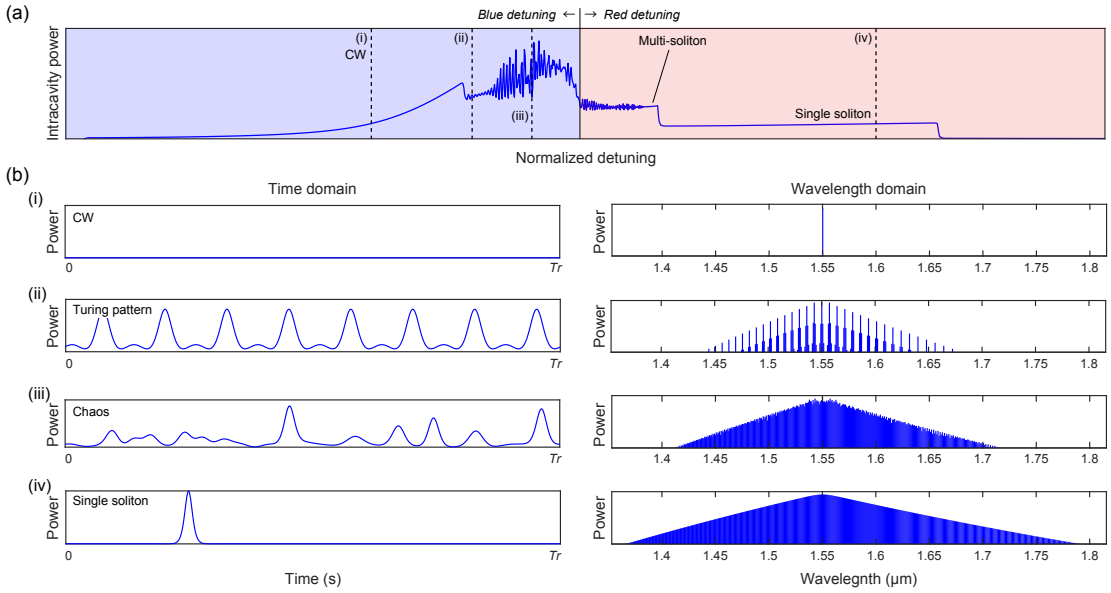

Fig. 2.10 Calcurated results of microcomb formation with an LLE (Equation (2.44)). The parameters used are typical values for microtoroids with a diameter of 600 μm. (a) Intracavity power is a function of pump detuning. (b) Microcomb spectra in the time domain (left column) and in the wavelength domain (right column). There are mainly four states in the microcomb which depend on the pump detuning: (i) CW state, (ii) Turing pattern state, (iii) chaotic state, (iv) single soliton state.

can destabilize the conditions required for soliton formation. Moreover, the Kerr nonlinearity, which is central to soliton formation, must be precisely balanced against the microresonator's group velocity dispersion. These conditions are highly sensitive to various parameters, including pump power, laser detuning, and resonator material properties, rendering the process complex and vulnerable to instability.

To address these challenges, researchers have developed several advanced techniques for facilitating reliable soliton generation in microresonators. These methods focus on actively managing the thermal dynamics and nonlinear interactions to guide the system toward stable soliton states.

Frequency-scanning method In the frequency-scanning technique, the pump laser frequency is gradually tuned across the resonator's resonance, allowing the system to move from chaotic comb states to soliton states. As the frequency is swept from the blue-detuned side toward the red-detuned side, solitons emerge once a stable balance between Kerr nonlinearity and GVD is established. Crucially, the scanning speed must match the resonator's thermal relaxation time (i.e. the thermo-optic response time). A scan that is too rapid may miss

the soliton formation window, while an overly slow scan can lead to undesirable thermal drift. This relatively simple approach has been widely implemented in fluorite crystal [15], Si_3N_4 [60], and AlN [61] microresonators to reliably produce soliton microcombs.

Power-kicking method In microresonators with pronounced thermo-optic effects, the available soliton steps in the resonance tend to be extremely short, often on the order of submicroseconds. This makes it difficult for conventional tunable lasers to stabilize the pump frequency precisely within these narrow windows. To overcome this limitation, a "power-kicking" approach is employed, in which modulators control the pump power and timing sequence with high precision [62, 63]. In this method, the pump laser first passes through an erbium-doped fiber amplifier (EDFA) and an acousto-optic modulator (AOM) before coupling into a microresonator. The AOM is used to reduce the pump power prior to tuning into the resonance and subsequently increase the power within the soliton step near the end of the thermal triangular signature. This power drop minimizes thermal nonlinearity and enables a rapid transition to zero detuning. It is noted that this power modulation must be carefully optimized in terms of timing, amplitude, and initial pump power in order to generate reliable soliton microcombs.

While power kicking has proven effective in various proof-of-concept experiments, including dual-comb spectroscopy [64] and microcomb-based ranging [65], the requirement for multiple modulators and precision control circuitry can make the overall system more complex, thereby complicating attempts at device miniaturization.

Fast-scanning method Fast-scanning involves rapidly tuning the pump laser frequency in a manner that outpaces the resonator's thermal response [66]. This strategy prevents thermally induced resonance shifts from destabilizing the soliton formation process. By mitigating the impact of thermal hysteresis, fast-scanning enables repeatable access to soliton states without prolonged temperature-related drifts. Experimental work in Si_3N_4 microresonators has shown that fast-scanning can be particularly beneficial in systems with pronounced thermal effects or higher pump power levels.

Auxiliary laser method The auxiliary laser method addresses the thermal instability that often complicates soliton microcomb generation by maintaining a steady level of intracavity power throughout the tuning process [67]. Microresonators exhibit opposite thermal responses depending on whether the pump light is in the blue- or red-detuned regime. As the pump laser moves from blue- to red-detuned conditions, the intracavity heat typically decreases dramatically, destabilizing the resonator and shortening the soliton existence range.

By introducing a second (auxiliary) laser that remains in the blue-detuned regime, however, this decrease in intracavity heat can be effectively compensated, thereby stabilizing the cavity resonance and relaxing the strict timing requirements ordinarily needed for soliton formation.

In a typical configuration, the auxiliary and pump lasers are coupled into a microresonator. First, the auxiliary laser is aligned to the resonance on the blue-detuned side, and then the pump laser is gradually tuned into an adjacent resonance. Once the pump laser enters the red-detuned regime, the drop in intracavity power is offset by the auxiliary laser, preventing resonance shifts and enabling a stable transition from chaotic comb states to soliton states. This approach ensures that the total intracavity power remains nearly constant, effectively eliminating harmful thermal drifts.

Employing an auxiliary laser at around 1.3 μm has been shown to extend soliton steps by two orders of magnitude [67], allowing robust soliton generation even via manual tuning of the pump resonance at sub-milliwatt power levels. This technique has also proven effective in other microresonator platforms, including silica [67, 55] and Si_3N_4 [68] resonators, and is thus regarded as a robust and universal approach to stabilizing soliton generation. Beyond thermal stabilization, the auxiliary laser offers additional degrees of freedom for exploring microcomb dynamics. For instance, the frequency spacing between the auxiliary and pump lasers can significantly influence the accessible microcomb states, while their beating may create an optical lattice that facilitates soliton crystal formation [69].

In conclusion, many methods represent significant advances in soliton microcomb generation. By tackling the fundamental challenges of thermal instability and nonlinearity, they have substantially enhanced the reliability and robustness of soliton states in microresonators. As these techniques continue to mature, they are expected to accelerate innovations in integrated photonics, enabling wider adoption of compact, high-coherence soliton microcombs for next-generation applications.

Chapter 3

Fabrication and evaluation of ultra-high-Q microresonators

In this thesis, I mainly use two types of microresonators: silicon dioxide microspheres and silicon dioxide microtoroids. This chapter focuses on the fabrication processes of silicon dioxide-based microresonators, which are critical components in integrated mode-locked laser systems. Microresonators provide high-Q optical cavities capable of confining light within a small volume, enabling enhanced light-matter interactions and facilitating ultrafast optical phenomena. The primary goal of this chapter is to establish a systematic methodology for fabricating high-quality microresonators, addressing the challenges of precision, uniformity, and scalability.

The chapter begins by discussing the fabrication of silicon dioxide microspheres, which serve as simple yet effective resonator structures with high-quality factors. It then transitions to silicon dioxide microtoroids, whose toroidal geometry provides improved mode confinement and versatility for integration into photonic systems. Detailed procedures for creating these structures, including thermal reflow and surface tension-based reshaping, are outlined.

In this research, I use the sol-gel chemical fabrication technique to incorporate optical gain into silica microresonators. Doping the silica matrix with erbium ions during the sol-gel process enables precise control over the uniformity and concentration of the gain material within the resonator structure. Subsequently, the chapter explores the fabrication of erbium-doped silicon dioxide microspheres and microtoroids. The incorporation of erbium ions introduces optical gain to the resonators, which is essential for achieving lasing at 1550 nm of wavelength.

3.1 Silicon dioxide microsphere

Microsphere resonators, one of the types of whispering-gallery-mode (WGM) microresonators, were first reported in 1939 [70]. Due to their relatively simple fabrication process, these resonators have been widely studied and utilized in a variety of fields, including the generation of microcombs [71], cavity quantum electrodynamics [72], microlasers [73–75], and sensing applications [76]. Their ability to confine light with minimal losses and achieve high Q-factors makes them particularly attractive for both fundamental research and practical applications.

The fabrication of microsphere resonators is straightforward and involves the following steps:

Preparation of the fiber: A segment of optical fiber, approximately 10 cm in length, is cut. The protective polymer coating around the fiber end, where the microsphere will be formed, is stripped off over a few centimeters to expose the bare silica core.

Polishing the fiber end: The cut surface is polished using a fiber cleaver to ensure that the fiber end face is smooth and perpendicular to the fiber axis. This step is crucial for achieving precise shaping in subsequent steps.

Heating and melting with a CO_2 laser: The polished fiber end is exposed to a CO_2 laser, which melts the silica material at the tip. As the silica melts, surface tension causes it to form a spherical shape. The laser power is gradually increased during this process to achieve the desired geometry.

Shape optimization: The formation of the microsphere is continuously monitored using a camera. The position of the CO_2 laser beam is adjusted in real-time to refine the symmetry and smoothness of the sphere, ensuring optimal optical performance.

In addition to using CO_2 lasers, the fiber end can also be melted using arc discharge as an alternative method. Arc discharge is often employed in cases where more straightforward equipment is preferred.

Microscopic images of the fabricated microspheres are shown in Fig. 3.1(b). The fabrication time for a single microsphere is approximately 5 minutes. The resulting resonators have an average diameter of around 200 μm. Considering that the diameter of the cladding in the optical fiber used is 125 μm, it is possible to enlarge the microsphere diameter to approximately 400 μm through multiple exposures to the CO_2 laser. Conversely, by etching

the fiber end face with buffered hydrofluoric acid (HF), microspheres with diameters as small as 70 μm can be produced [77].

By selecting microspheres without distortions or defects, it is possible to obtain resonance spectra, as shown in Fig. 3.1(a), in the 1550 nm wavelength band. These microspheres exhibit Q-factors exceeding 10^7 in this wavelength range. Fig. 3.1(b) presents a histogram of the Q-factor measurements for approximately 400 resonances observed between 1540 nm and 1560 nm.

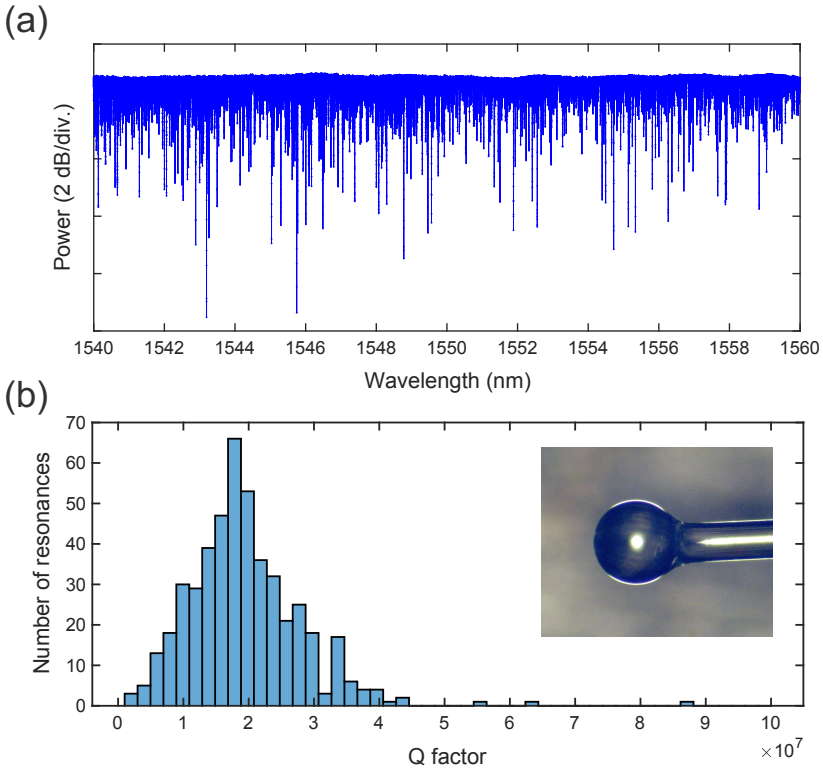

Fig. 3.1 (a) Transmission spectrum measured from 1540 nm to 1560 nm. (b) Histogram of the Q-factor measurements for approximately 400 resonances observed between 1540 nm and 1560 nm. The inset shows a microscopic image of a fabricated microsphere resonator.

3.2 Silicon dioxide microtoroid

Silicon dioxide microtoroids were developed in 2003 by the California Institute of Technology (Caltech) [78] and used to demonstrate microcomb generation in the first critical report in 2007 by the Max Planck Institute for Quantum Optics (MPQ) [14]. The advantages of microtoroids lie in their ability to combine ultra-high Q-factors (∼100 million) with

a compact footprint, enabling strong light confinement and enhanced nonlinear optical interactions.

Figure 3.2 shows that the microtoroid fabrication process consists of four main steps: photolithography, wet Etching, dry Etching, and laser reflow. Each step plays a critical role in ensuring the high precision and optical quality of the resonators. This section provides a detailed explanation of each stage in the process.

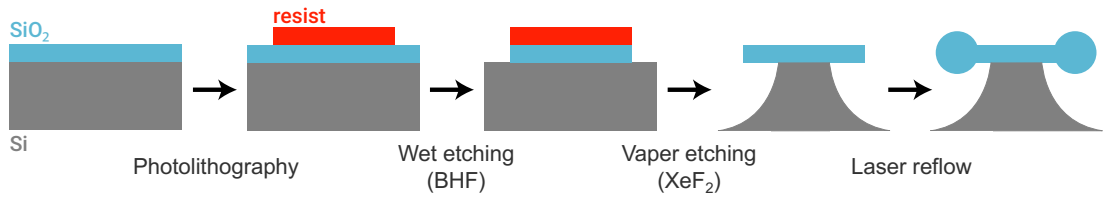

Fig. 3.2 Schematic cross-section image of microtoroid fabrication.

3.2.1 Photolithography

Microtoroids are fabricated using silica film, which is prepared using thermally oxidized silicon substrates. The process begins with photolithography, where patterns are formed on the silica substrate. A negative photoresist, OFPR-800 LB, is applied, and a photomask specifically designed for microresonator structures is used to define the desired patterns. The detailed photolithography process is as follows.

Substrate preparation The cleaning process for the substrate starts by removing debris using acetone, ethanol, and ultrapure deionized water in sequence, followed by drying with an N_2 blow gun. O_2 plasma ashing is performed to remove organic contaminants that adhere during substrate preparation. Additionally, since the substrate absorbs moisture from exposure to the atmosphere, it is heated on a hot plate at 150°C for 3 minutes to remove residual moisture.

Photoresist coating The spin-coating method treats the substrate surface condition before applying a negative photoresist with hexamethyldisilazane (HMDS). This process renders the substrate surface hydrophobic. Without this treatment, the hydrophilic surface can allow the developer solution, which contains water, to infiltrate between the photoresist and the substrate during development. This infiltration causes the patterned photoresist to wash away, as shown in Fig. 3.3

After HMDS spin-coating, the substrate is baked at 130°C for 90 seconds in a constant temperature drying oven. This baking step ensures the HMDS molecules adhere to the substrate surface, acting as a surfactant. Without this step, residual ammonia remains on the surface, negatively affecting subsequent processing steps.

Next, the photoresist (OFPR-800 LB) is spin-coated onto the substrate, and a pre-bake is conducted at 110°C for 90 seconds in the drying oven. The purpose of pre-baking is to evaporate solvents within the photoresist, improving adhesion between the photoresist and the substrate. However, excessively high pre-bake temperatures alter the sensitivity of the photoresist to UV exposure, so moderate temperatures are typically used. It is also crucial to allow the photoresist to equilibrate to room temperature ($\sim$ 25°C) after being taken from a storage environment (approximately 15°C). Suppose the photoresist is still cold during exposure and development. In that case, its photosensitivity decreases, leading to poor pattern formation. Proper temperature management using a hot plate ensures these issues do not occur.

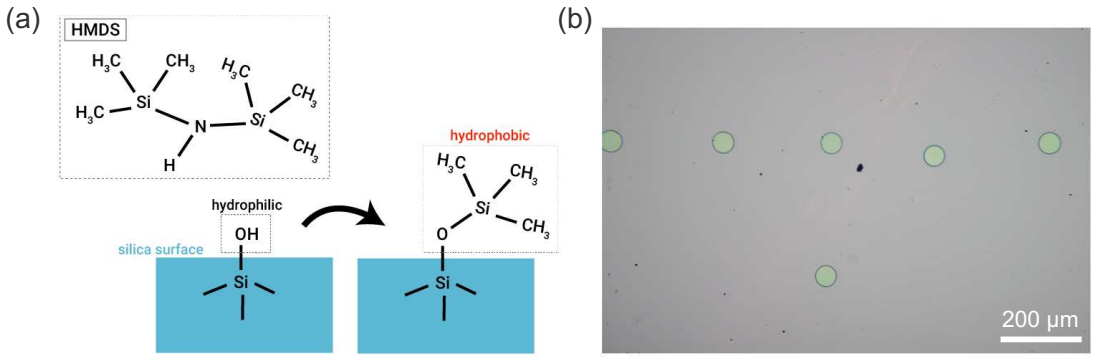

Fig. 3.3 (a) The chemical reaction of HMDS coating on the silica surface renders the surface from hydrophilic to hydrophobic. (b) A microscopic image of patterning issues occurred after photolithography. The photoresist patterns lift during development, causing it to shift from its intended alignment.

Exposure Exposure involves transferring the desired pattern from a mask to the photoresist by irradiating it with light of a specific wavelength. This causes a chemical reaction that either dissolves or retains the photoresist in the developer solution. This study uses a negative photoresist, meaning the exposed areas remain after development.

Using the hard-contact method, I employ a mask aligner for exposure. A composite UV lamp emits g-line, h-line, and i-line light. Exposure is carried out for 5–10 seconds, and the time is carefully selected to ensure sufficient reaction for successful development.

Development The development process, followed by rinsing, selectively dissolves the photoresist's exposed or unexposed areas in the developer solution to create the desired pattern. In this process, I use the organic solvent NMD-W as the developer, followed by rinsing with ultrapure deionized water to halt the reaction and eliminate any residual developer. Insufficient rinsing leaves residual photoresist, potentially compromising the pattern quality.

Following rinsing, I conduct a post-bake process at 130°C for 5 minutes. This step removes any residual solvents or developer solution and enhances the adhesion between the photoresist and the substrate by promoting the polymerization of the photoresist material. After the photolithography process, the height of the patterned photoresist pads ranges from 1 to 2 μm.

3.2.2 Wet etching

In photolithography, the patterned photoresist is a mask for wet Etching, a process used to remove silica. Wet Etching involves using chemical solutions to corrode or dissolve the material. This technique is widely employed in microsensors and micromachines, particularly when etching depths range from several tens to hundreds of micrometers or when fabricating three-dimensional structures.

Wet Etching can be categorized into isotropic and anisotropic types, significantly affecting the etched cross-section's shape. Generally, when etching proceeds through the mask opening, the corrosion advances perpendicular to the surface (sidewall etching) and underneath the mask (undercutting). In isotropic Etching, the etching solution uniformly supplies reactants and removes by-products, resulting in equal etching rates in all directions. Conversely, anisotropic Etching occurs when the workpiece material, such as single-crystal silicon or quartz, exhibits a crystalline structure with inherent directional properties.

The choice between isotropic and anisotropic Etching is critical, as it directly influences the precision and geometry of the final structure. Isotropic Etching is suitable for applications requiring smooth, rounded profiles, while anisotropic Etching is essential for creating sharp, well-defined edges and features. These characteristics make wet Etching a versatile tool in microfabrication processes.

Etching with buffered hydrofluoric acid In the fabrication of silica microtoroids, buffered hydrofluoric acid (BHF) is used as the etching solution. BHF is an aqueous mixture of hydrofluoric acid (HF) and ammonium fluoride (NH_4F), commonly utilized for etching silica and for evaluating the quality of glass materials. The etching time is estimated based on

the etching rate, which varies depending on the solution's temperature. A thermostatic bath maintains the solution at 25°C, and the etching rate is approximately 100 nm per minute.

Due to the hazardous nature of hydrofluoric acid in the solution, strict safety measures are implemented. Specialized gloves are worn, and all handling is conducted with utmost caution to minimize risks during the process.

Photoresist removal After reacting the substrate with BHF for the estimated time, the substrate is removed from the solution and carefully rinsed with ultrapure deionized water to eliminate any residual acid. The substrate is then dried using an N_2 blow gun to remove moisture. At this stage, the photoresist pads remain intact on the silica surface. These are subsequently removed using an organic solvent. The substrate is immersed in acetone and subjected to ultrasonic cleaning for 3 minutes to dissolve and remove the photoresist completely.

A critical consideration during this wet etching process is the potential for particles to adhere to the silica pattern, leading to defects (Fig. 3.4(a), (b)). To mitigate this, thorough cleaning with ultrapure deionized water between each process step is essential to maintain the integrity of the silica pattern and prevent contamination. In addition, the smooth surface of the limb of the photoresist is also important to fabricate high-Q microresonator [79, 80]. Figure 3.4(e) shows a rough surface of a photoresist after the photolithography process. This micrometer roughness causes the surface roughness of the disk surface, leading to surface scattering loss. To solve this issue, post-exposure baking (PEB) is applied because it can facilitate the cross-linking of the polymer chains, making the surface smooth even after the development and the wet etching processes.

3.2.3 Vapor etching

Vapor etching includes isotropic Etching through chemical reactions, as exemplified by silicon etching with xenon difluoride (XeF_2) gas and Etching using plasma-activated gases. In this study, the disk resonators are realized by under-etching the silica pads with XeF_2 gas.

In the reaction between XeF_2 and Si, XeF_2 dissociates into Xe and F on the Si surface. The F radicals then directly interact with the Si atoms, facilitating the etching process. The reaction begins with the adsorption of fluorine on the silicon surface [81, 82]:

$$XeF_2(\text{gas}) + \text{Si} \rightarrow XeF_2(\text{ads}) + \text{Si}, \tag{3.1}$$

$$XeF_2(\text{gas}) + \text{Si} \rightarrow \text{Xe(ads)} + 2\text{F(ads)} + \text{Si}. \tag{3.2}$$

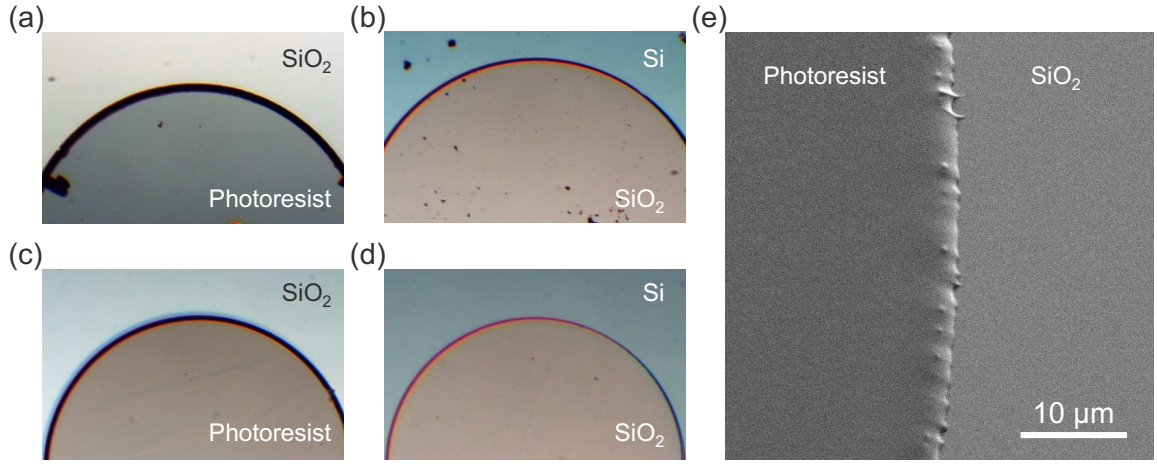

Fig. 3.4 (a) A microscope image showing defects near the patterned region after development. (b) A microscope image after wet etching with particles. (c) and (d) Fabrication results using the same process but with more careful cleaning steps. (e) A SEM image illustrating rough edges in the photoresist pattern boundary. This micrometer roughness causes the surface roughness of the disk surface, leading to surface scattering loss and low-Q.

Next, silicon tetrafluoride (SiF_4) is formed as a product and desorbs from the surface.

$$4F(ads) + Si \rightarrow SiF_4(ads), \tag{3.3}$$

$$SiF_4(ads) \rightarrow SiF_4(gas). \tag{3.4}$$

Finally, residual by-products are removed from the reaction chamber.

$$XeF(ads) \rightarrow XeF(gas). \tag{3.5}$$

Summarizing equations 3.1 through 3.5, the overall reaction can be expressed as:

$$2XeF_2 + Si \rightarrow 2Xe + SiF_4. \tag{3.6}$$

This reaction sequence illustrates the stepwise etching process, from initial fluorine adsorption to removing reaction products, ultimately achieving isotropic Etching of silicon. Etching with XeF_2 gas is characterized by its extremely high selectivity for the target material. For silicon and silica, the selectivity ratio is as high as $Si : SiO_2 = 1000 : 1$. This means that while silica remains unaffected, silicon undergoes Etching, enabling the undercutting process. However, XeF_2 reacts with H_2O to produce HF, which can etch SiO_2. If moisture is present on the substrate, the generated HF may compromise the integrity of the silica layer.

To mitigate this, it is crucial to thoroughly dry the substrate and remove residual moisture through vacuum processing.

The etching process uses a XeF_2 gas etching system (Samco VPE-4F). This system operates by introducing XeF_2 gas into a vacuum chamber, releasing it for a defined period, and then evacuating the chamber in repeated cycles. Following this process, a structure consisting of a silica disk resting atop a silicon pillar is formed. While this structure already functions as a silica disk resonator, the surface roughness remaining after vapor etching—on the order of 100 nm results in a relatively low Q factor.

To achieve a high-Q microtoroid, the surface roughness must be significantly reduced. This necessitates the next step in the fabrication process: CO_2 laser reflow, which is described in the following section. The reflow process smooths the silica surface, enabling the creation of high-Q resonators suitable for advanced photonic applications.

3.2.4 Laser reflow

The CO_2 laser reflow process involves irradiating a silica disk, undercut from its silicon pillar, with a CO_2 laser from above. This process melts the outer edge of the silica disk, smoothing its surface and transforming it into a toroidal shape. Silica strongly absorbs the CO_2 laser wavelength (10.6 μm) due to its significantly higher absorption coefficient than silicon. Additionally, silicon's high thermal conductivity facilitates heat dissipation from the central region of the silica disk, which is in contact with the silicon pillar. In contrast, the disk's outer edge retains heat, reaching its melting point, while the central region remains solid. This localized melting results in the formation of a donut-shaped silica microtoroid.

Precise control of heat accumulation is crucial for forming effective waveguide structures at the disk edges. Therefore, the depth of vapor etching must be carefully adjusted, ensuring that the diameter of the silicon pillar is reduced to approximately 60% of the silica disk diameter before the reflow process begins.

In this study, the CO_2 laser parameters are set within the following ranges: power of 10–25 W, spot size of 300–500 μm, and irradiation time of 1–3 seconds. These parameters are adjusted based on the diameter of the silica disk being processed. During irradiation, a visible-light camera monitors the sample, focusing on the formation of the waveguide structure at the disk edge. This real-time observation is essential for optimizing the laser parameters to achieve the desired geometry.

For disks with diameters exceeding 800 μm, the relationship between the laser's power and spot size makes direct reflow challenging. To address this, the sample holder is rotated to ensure uniform laser exposure around the disk's outer edge, enabling the successful

fabrication of sub-millimeter-scale microtoroids. This controlled reflow process produces high-Q silica microtoroids with smooth surfaces.

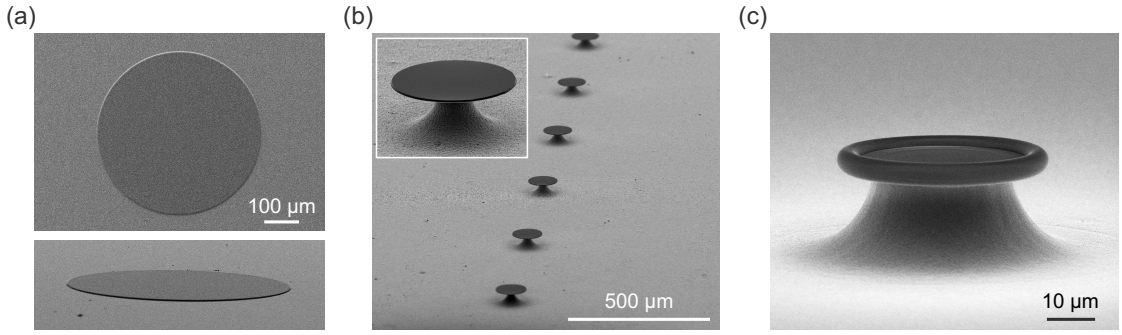

Fig. 3.5 (a) A top-view (upper panel) and angled-view (lower panel) SEM image of a patterned silica pad on a silicon wafer with a diameter of 500 μm. (b) An SEM image of disk resonators (50 μm diameter) after XeF_2 vapor etching process. The inset image is an enlarged view of one of the disk resonators. (c) A fabricated silica toroidal microresonator with a diameter of 40 μm.

3.2.5 Microcomb generation in silicon dioxide microtoroid

This section examines the measurement of the soliton access range (soliton step) at the 1550 nm band using the setup shown in Fig. 3.6 and a silica microtoroid with a quality factor of 4×10^8, has a diameter of ~ 200 μm. A fiber laser (Koheras AdjustiK E15) with a 0.1 kHz linewidth serves as the pump source, and an EDFA amplifies the output light before it enters the resonator through a tapered fiber. A coupler separates the transmission signal, which an OSA monitors in the wavelength domain. Simultaneously, an FBG and an oscilloscope measure the waveforms of the pump and comb light in the time domain.

Figure 3.7 presents the observed soliton steps under these conditions. The input power is 20 mW, and the pump laser sweep rate is 1 MHz/μs. The soliton step duration is extremely short, lasting only 2 μs. Additionally, the number of steps varies with each scan, revealing the coexistence of single-soliton and multi-soliton states.

To extend the soliton step and access the soliton regime, we employ the auxiliary laser method that is commonly used in silica microresonators. The auxiliary laser method, which compensates for thermal effects inside the resonator, is used to expand the soliton access range. Figure 3.8 shows the schematic of the experimental setup. A 1550 nm fiber laser is used as the pump laser for generating a soliton frequency comb. A 1480 nm tunable laser is used as an auxiliary laser to compensate for changes in the thermal shift in the resonator. We choose a microtoroid with 300 μm diameter to generate optical frequency comb. The

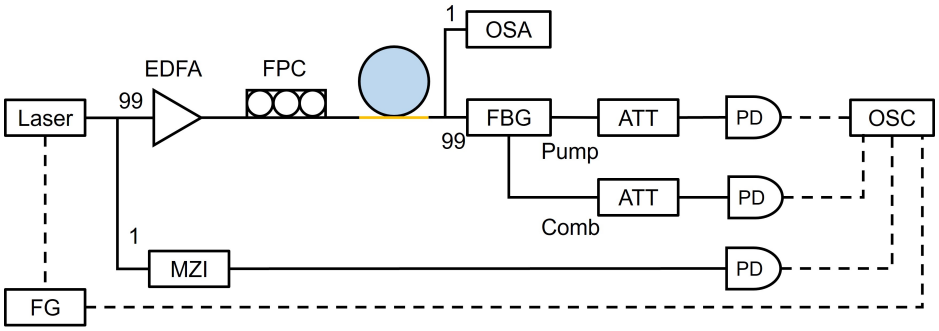

Fig. 3.6 Experimental setup for soliton step measurement. FG, function generator; EDFA, erbium-doped fiber amplifier; MZI, Mach Zehnder interferometer; FPC, fiber polarization controller; OSA, optical spectrum analyzer; FBG, fiber Bragg grating; ATT, attenuator; PD, photodiode; OSC, oscilloscope.

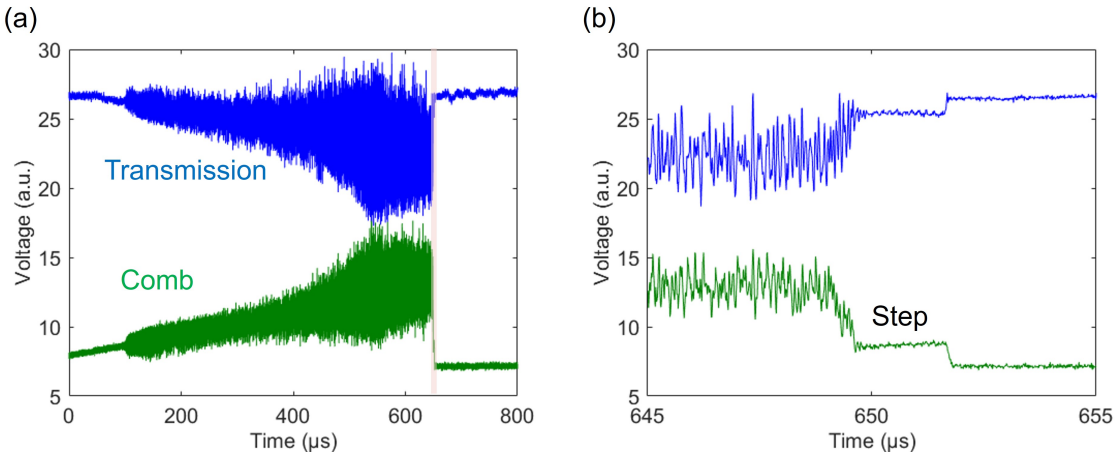

Fig. 3.7 (a) Measured intracavity power in the time domain (blue) and generated comb power (green). The input power is 20 mW, and the pump laser sweep rate is 1 MHz/μs. (b) An enlarged view of (a), showing a trace of the narrow soliton step with a duration of 2 μs.

pump optical mode has a Q factor of 4×10^8, while the chosen auxiliary optical mode has a Q factor of 1×10^8 in 1480 nm. At the tapered fiber coupled resonator output, the auxiliary and pump lights are separated by another WDM. For 1550 nm, one part of the path is sent to an optical spectrum analyzer (OSA), and the other path is sent into a fiber Bragg grating (FBG) filter to separate the generated comb power from the pump light. The auxiliary light is monitored by another photodiode.

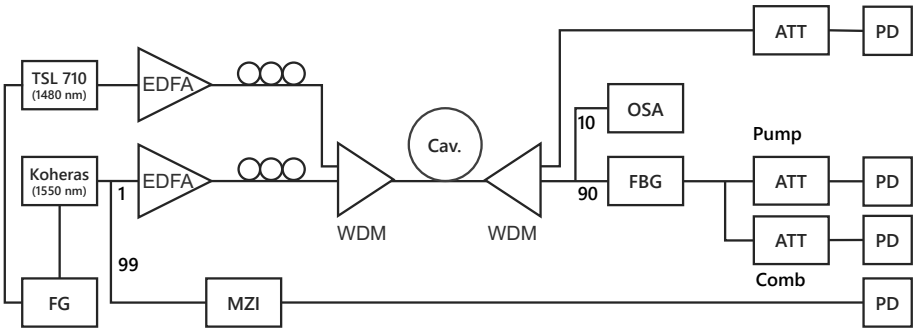

Fig. 3.8 Experimental setup to extend the soliton access range in silica microtoroid by using an auxiliary laser to compensate the resonator's thermal effect.

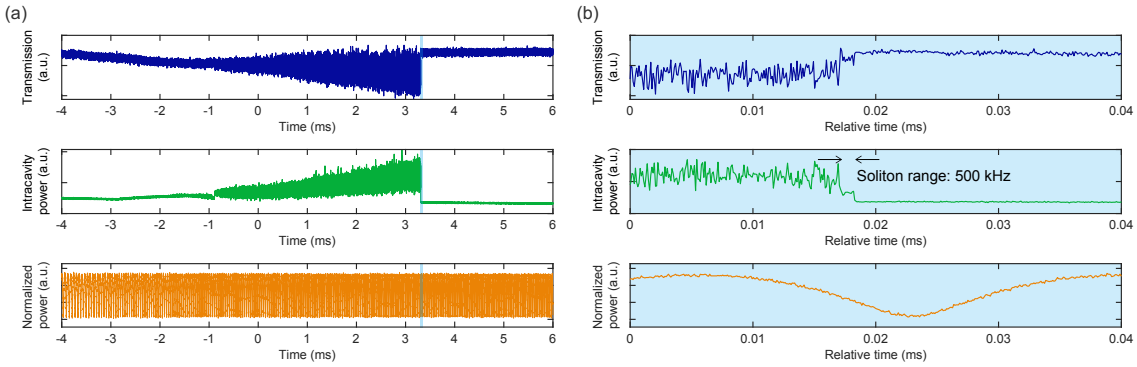

Fig. 3.9 (a) Experimental result of the 1550 nm intracavity power when scanning the pump laser frequency from blue to red detuning without auxiliary laser. The top panel indicates the transmission spectrum, the middle panel shows the intracavity power, and the bottom panel is a signal from MZI. (b) Enlarged views of the blue box region in (a). At the end of the triangle shape in the middle panel, the soliton step ranging $\sim$ 500 kHz is observed.

Soliton mode-locked states are generated by scanning the pump laser frequency from blue detuning to red detuning. The measured intracavity power of the generated comb has a triangular shape, as shown in Fig. 3.9(a). The pump wavelength, optical power, and laser scan speed are $\sim$ 1550 nm, $\sim$ 75 mW, and $\sim$ 5 MHz/μs, respectively. The width of the shifted resonance (top panel of Fig. 3.9(a)) is $\sim$ 700 MHz. As shown in the middle panel of

Fig. 3.9(a) corresponding to the intracavity power, the soliton range (soliton step) is observed. Fig. 3.9(b) shows a zoom into a soliton range without the auxiliary laser with a width of 500 kHz.

Here, an auxiliary laser (1480 nm) is used to expand the soliton range. Fig. 3.10(a) and (b) show the experimental results without/with the auxiliary laser. When the auxiliary laser with $\sim$ 100 mW is simultaneously coupled into the resonator, the length of the soliton range is significantly extended by a factor of 10, exceeding 6 MHz. As a result, with the auxiliary laser, the soliton range can last for 100 μs, which is 20 times longer duration than that without the auxiliary laser. Additionally, as shown in Fig. 3.10(c), the intracavity power from both the pump (green) and the auxiliary laser (red) exhibits a step-like waveform within the soliton range. This indicates that thermal compensation occurs in this regime.

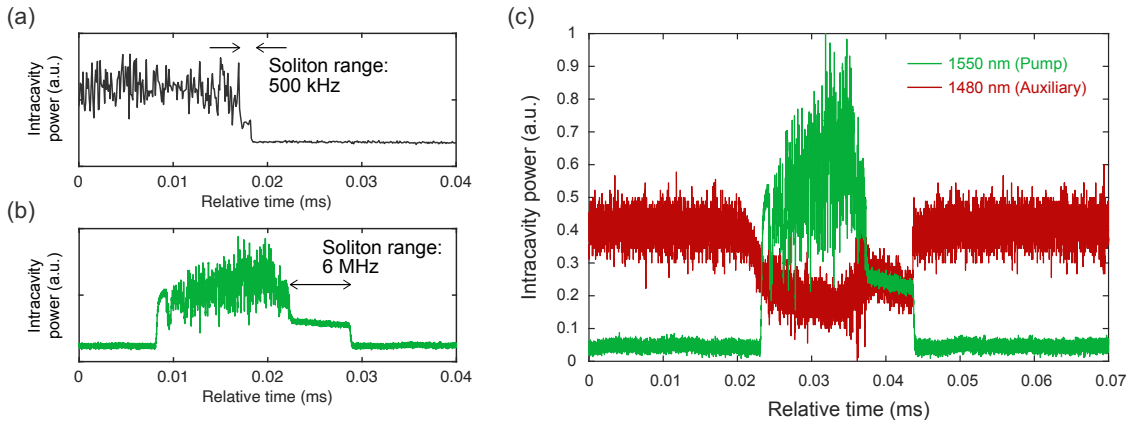

Fig. 3.10 Experimental traces of the 1550 nm intracavity power (a) without the auxiliary laser and (b) with the auxiliary laser. The pump laser scanning speed is $\sim$ 5 MHz/μs and pump power is $\sim$ 75 mW. After the auxiliary laser with $\sim$ 100 mW coupled into the resonator, the width of the thermal tringle is narrowed to $\sim$ 10 MHz, while the soliton range is extended from $\sim$ 500 kHz to $\sim$ 6 MHz. (c) The intracavity power excited by the pump laser (green) and the auxiliary laser (red). The auxiliary laser (1480 nm) passively compensates for changes in the intracavity power of the pump laser (1550 nm).

3.3 Saturable absorber deposition to microresonators

In this section, we developed a fabrication method for depositing a saturable absorber (SA) onto a microresonator. We have already reported the saturable absorption of CNTs on a silica toroid microcavity grown on a cavity surface by using chemical deposition (CVD) [83]. However, it was somewhat challenging to control the quantity of CNTs with this method, which is critical if we want to develop a mode-locked laser. Here, we use two different

approaches. The first one is that CNTs are dispersed in the Polydimethylsiloxane (PDMS) polymer and then coated on a microcavity. This approach is advantageous since we can control the quantity of CNTs, which means that we can precisely control the linear and nonlinear loss. The other is that the few layers of graphene are directly transferred onto the surface of a microresonator. This method allows graphene to be transferred to any desired location on the resonator, and two-dimensional materials such as graphene minimize linear losses.

3.3.1 Polydimethylsiloxane coating

We start with ultrasonicated CNTs made in isopropanol with the high-pressure CO (HiPco) method [84], where PDMS is added step-by-step to the solution, thus allowing the viscosity to increase gradually. Then, the isopropanol (boiling point of 83°C) is slowly evaporated while the solution is kept at 70°C for 48 hours to prevent rough surfaces with holes [85]. Finally, the CNT/PDMS droplets are transferred to the fabricated silica toroid microcavity with the method shown in Fig. 3.11.

Fig. 3.11 Images of CNTs dispersed in PDMS and coated on the silica microtoroid with a diameter of 70 μm. We attach the CNT/PDMS droplets to a thin fiber (10-μm-diameter) and coat it on a resonator by bringing the resonator closer to the fiber.

The thickness of the CNT/PDMS coating layer is determined by calculation. Figure 3.13(a) shows the relationship between the thickness of the PDMS coating layer and the Q-factor analyzed using FEM (COMSOL Multiphysics). The coating layer thickness is calculated from the absorption limit of the PDMS layer in three different dispersed CNT concentrations. Based on the results for 0.03 mg/ml and 0.24 mg/ml, the coating layer thickness is determined to be approximately 160 nm.

The SA of a CNT/PDMS coated microcavity with 0.24 mg/ml CNTs is measured. We developed a CW pump-probe method (Fig. 3.12(a)), where the frequencies of both the pump and probe are simultaneously scanned but at different sweep speeds (a slow sweep speed for the pump and a fast sweep for the probe that measures the Q). Fig. 3.12(b) and (c) are schematic illustrations of this method. The pump light gradually enters the cavity due to

the thermal shift. Then, by scanning the probe light fast, the Q-factor can be measured at different coupling pump powers. The Q of the cold cavity is 1.3×10^6, where the value increases to 1.8×10^6 when the pump is coupled to the cavity.

The result is summarized in Fig. 3.13(b), where clear SA is observed. As the pump light gradually enters the cavity, the intracavity power increases, the absorption of the CNTs weakens, and the Q-factor rises. Then to replace the increase in the Q-factor with the absorption coefficient, we measure the saturable absorption. The saturation intensity is 15 $\mathrm{MW/cm^2}$, and the modulation depth per round trip is 3.2×10^{-3}.

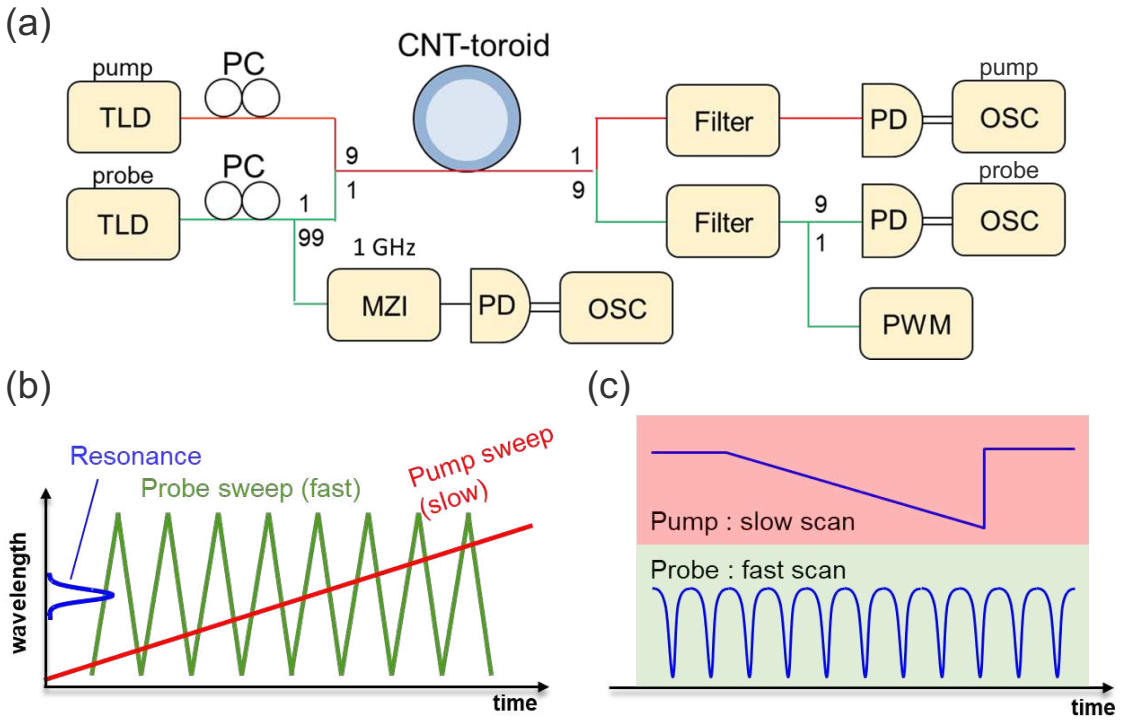

Fig. 3.12 (a) Experimental set-up for the saturable absorption measurement of a CNT/PDMS coated silica microtoroid. (b) A schematic illustration of scanning wavelengths of pump and probe light in the time domain. (c) A schematic illustration of the transmittance of pump and probe light in the time domain. This scanning method allows us to measure Q-factors at different coupling pump powers.

3.3.2 Graphene transferring

The coating method using CNT/PDMS allows for the measurement of the SA in microresonators; however, the absorption of PDMS significantly reduces the Q-factor to the order of 10^6. To address this issue, we introduced a graphene transfer method. In this approach,

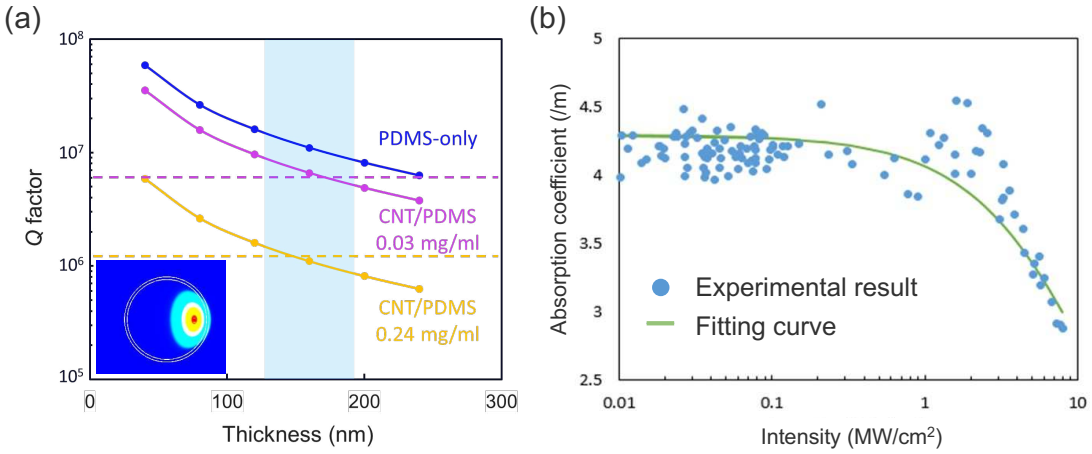

Fig. 3.13 (a) The relationship between the thickness of the PDMS coating layer and the Q-factor is analyzed using FEM. The blue, purple, and yellow lines represent the calculated results for CNT concentrations of none, 0.03 mg/ml, and 0.24 mg/ml, respectively, while the dashed lines indicate the Q-factors obtained from experiments. Based on the results for 0.03 mg/ml and 0.24 mg/ml, the coating layer thickness is determined to be approximately 160 nm. The inset image shows the mode cross-section of the PDMS-coated toroid resonator. (b) The relationship between intensity and absorption coefficient of a CNT/PDMS coated silica microtoroid. The blue dot is the experimental result, and the green line is a fitting curve. A clear SA is obtained, with a saturation intensity of 15 $\mathrm{MW/cm^2}$ and a modulation depth per roundtrip of 3.2×10^{-3}.

few-layer highly oriented pyrolytic graphene (HOPG) is exfoliated using the Scotch tape method with mechanical cleavage and subsequently transferred onto the microresonator using a PDMS sheet. Figure 3.14 shows a microscope image of a microsphere resonator before and after the graphene transfer, while Figure 3.15 presents an SEM image of a toroid resonator following the same process. Before the transfer, the average Q-factor of the toroid resonator at the 1550 nm band is 1.5×10^7, which decreases to 9×10^6 after the transfer. Additionally, in the high-Q mode, the Q-factor decreases from 8×10^7 to 4×10^7. Compared to the CNT/PDMS method, this approach minimizes the reduction in the Q-factor while incorporating the SA material.

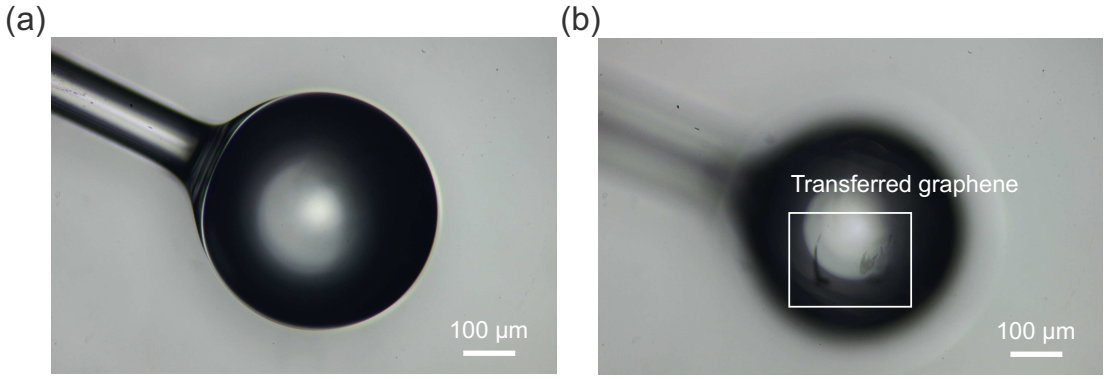

Fig. 3.14 Microscopic images of a microsphere resonator (a) before and (b) after graphene transferring. A few layers of graphene are clearly obtained on the surface of the microsphere with a diameter of 400 μm.

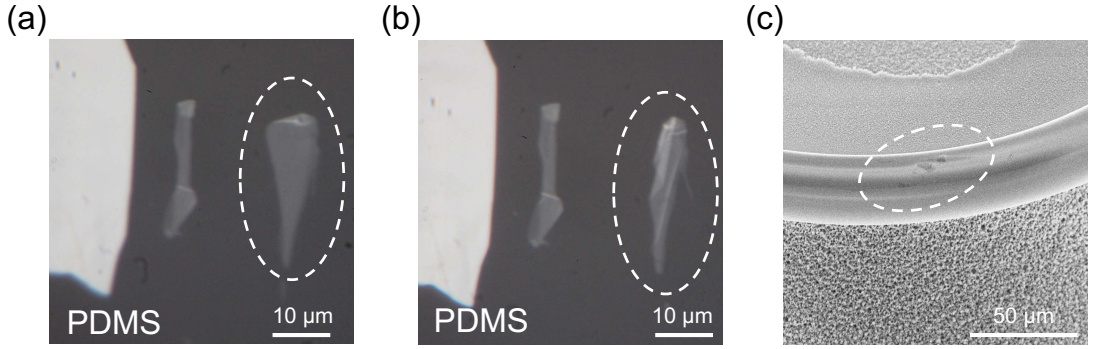

Fig. 3.15 Optical microscope images of the few-layer graphene on PDMS (a) before and (b) after transferred to the microtoroid. When graphene is transferred onto the surface of the microtoroid, the number of graphene layers on the PDMS, as shown in (b), decreases compared to the original graphene shown in (a). (c) An SEM image of the transferred graphene on the microresonator.

3.4 Introduction to the sol-gel method

In recent years, on-chip photonic integrated devices with optical gain and utilizing rare-earth ions and semiconductor materials have attracted considerable attention [86–89]. Of these, waveguide amplifiers doped with erbium ions have become particularly notable due to their compact size and high efficiency [90, 91], which has brought gain-doped photonic integrated circuits closer to practical realization. Low-loss microcavities with optical gain also offer chip-scale passive mode-locked lasers [92] by incorporating nanomaterials [83, 76, 93] that work as saturable absorbers. Another example of photonic integrated devices with gain utilizes non-Hermitian physics [94–99], particularly phenomena such as exceptional points. Recent studies have demonstrated that non-Hermitian systems enable us to realize enhanced functionalities, such as improved control over light propagation [100], loss management [101, 102], and enhanced sensor sensitivity [98, 99]. Specifically, in coupled whispering-gallery-mode (WGM) resonator systems, a gain-doped resonator is often paired with a passive resonator [102]. With this configuration, there is a contrast between gain and loss that depends on the light propagation direction. This has led to several intriguing studies including research on controlling the laser emission direction, suppressing optical modes, and achieving passive mode-locking [103].

Incorporating ions into existing photonic structures is typically achieved through ion implantation [90], a process in which ions are accelerated under an electric field and directed into a substrate material. This technique allows the precise doping of the material to modify its optical properties. However, a significant drawback of ion implantation is that it can increase losses in waveguides and resonators, as the process may introduce defects and damage to the crystal lattice of the host material [104]. Annealing is generally required after ion implantation to repair these defects; however, it also presents challenges, such as ion diffusion and potential thermal damage due to internal stress.

In contrast, the sol-gel process [105, 106, 22, 45, 107] is a method for fabricating oxide solids by dissolving organic or inorganic metal compounds in a solution, facilitating hydrolysis and polycondensation reactions within this solution, and further inducing solidification through heating. This technique is predominantly utilized in producing fibers such as silica-alumina, quartz, and alumina fibers in applications involving reflective coatings and other types of coating films [107, 108]. This method is initiated with a solution and progresses through a colloidal state containing fine particles, known as "sol," and transitioning through a "gel" phase with both liquid and gaseous inclusions between solid molecules. This process ultimately allows for the creation of glass or ceramic materials.

3.4.1 Sol-gel reaction

In the sol-gel method, the process begins by selecting a metal alkoxide corresponding to the desired oxide. Then, alcohol is added to prepare a mixed solution. Subsequently, water required for hydrolysis, along with an acid or base as a catalyst, is added as an alcohol solution to prepare the starting sol. The acid not only accelerates the reaction but also suppresses the formation of precipitates, thereby ensuring a homogeneous solution.

Under acidic conditions, the silica network forms a polymer-like structure [109], which promotes dense bonding during the heating process, making it easier to create thin films. In contrast, under basic conditions, the silica network remains relatively short, forming colloidal particles in the sol [109]. After heating, this results in a porous structure. Therefore, to fabricate uniform silica thin films in this study, the sol is prepared under acidic conditions using hydrochloric acid (HCl) as the catalyst.

For the fabrication of silica using the sol-gel method, tetraethyl orthosilicate (TEOS) is commonly used as the metal alkoxide. The chemical reactions involved in this process start with the hydrolysis reaction.

$$n\mathrm{Si}(\mathrm{OC_2H_5})_4 + 4n\mathrm{H_2O} \rightarrow n\mathrm{Si}(\mathrm{OH})_4 + 4n\mathrm{C_2H_5OH}. \tag{3.7}$$

Simultaneously, a condensation reaction occurs:

$$n\mathrm{Si}(\mathrm{OH})_4 \rightarrow n\mathrm{SiO_2} + 2n\mathrm{H_2O}. \tag{3.8}$$

Combining the two reactions, the overall process can be expressed as:

$$n\mathrm{Si}(\mathrm{OC_2H_5})_4 + n\mathrm{H_2O} \rightarrow n\mathrm{SiO_2} + 4n\mathrm{C_2H_5OH}. \tag{3.9}$$

For every 1 mol of TEOS, 4 mol of H_2O are theoretically sufficient. However, it is important to note that the pathways of the hydrolysis and condensation reactions vary significantly depending on the conditions of the solution. Consequently, the schematic image of the sol-gel thin film coating process on the target is shown in 3.16.

The sol-gel method, with its unique reaction mechanisms, offers several advantages in optics. These include the ability to synthesize materials at low temperatures, achieve a high degree of uniformity, produce glasses and ceramics with customizable compositions, and achieve higher production efficiency compared to methods like sputtering or chemical vapor deposition (CVD). The most noteworthy advantage is the capability for low-temperature synthesis.

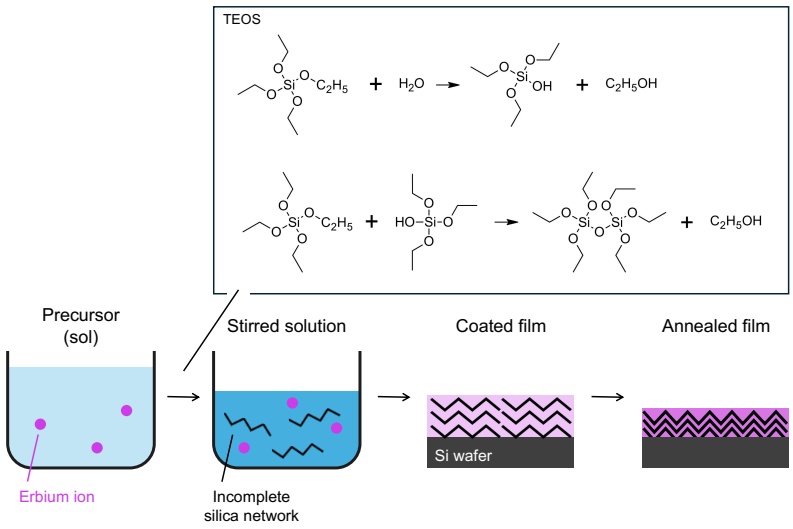

Fig. 3.16 Schematic illustration of the sol-gel reaction. In the precursor containing erbium ions, hydrolysis and polycondensation reactions occur over the stirring time, leading to the formation of an incomplete silica network. After coating onto the substrate, organic solvents and water are removed during the annealing process, resulting in a denser silica thin film.

Traditional glass fabrication methods, such as quartz fusion and CVD, require temperatures around 2000°C. In contrast, the sol-gel method enables the fabrication of silica glass at temperatures below 1100°C, which is lower than the glass transition temperature of silica. M. Yamane et al. [110] reported that the density, refractive index, and thermal expansion properties of silica glass fabricated using the sol-gel method are very similar to those of silica glass produced by quartz fusion.

In this study, a similar observation is made. For the fabrication of smooth silica films, an annealing temperature of 1000°C was sufficient. This demonstrates the sol-gel method's ability to produce high-quality silica thin films under significantly lower thermal conditions, making it an efficient and practical choice for optical applications.

3.4.2 Sol-gel thin film deposition and troubleshooting strategies

Sol-gel thin film deposition process

This section provides an overview of the method for fabricating sol-gel silica films on silicon substrates (Fig. 3.17). It explains the defects that can occur at various stages of the film formation process. Fabricating sol-gel thin films involves five major steps: solution mixing, silicon substrate cleaning, spin coating, short annealing, and long annealing. The spin coating and short annealing steps can be repeated for multilayer films to allow us to stack multiple layers.

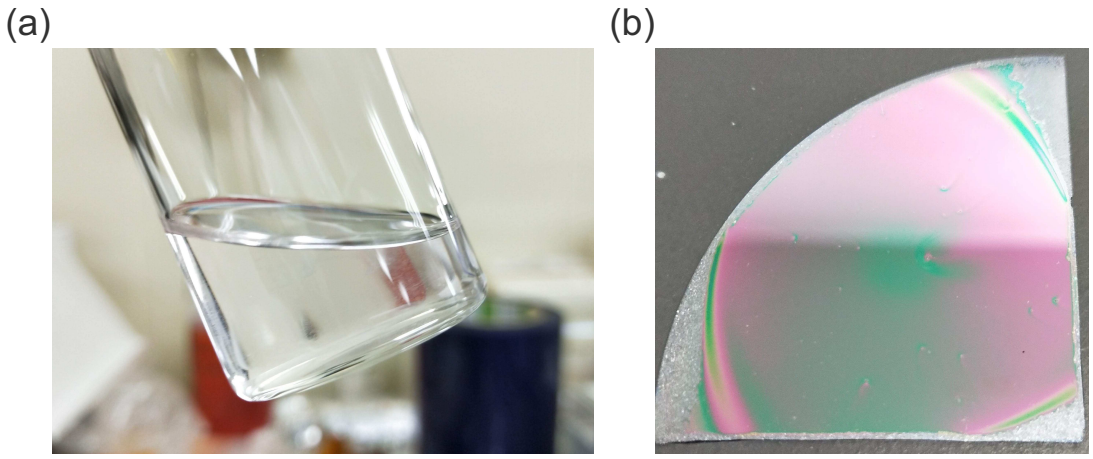

Fig. 3.17 (a) A sol-gel solution prepared by mixing with a tetraethyl orthosilicate, ethanol, and H_2O under acidic conditions. The erbium ions are mixed into this solution. (b) A photograph shows a sol-gel thin film-coated quartered 3-inch silicon wafer without defect.

Previous studies have reported various parameters that allow the successful fabrication of thin glass films using the sol-gel method for optical devices (Table 3.1). However, because temperature and humidity can significantly impact the film deposition process, these parameters may not directly apply to all experimental environments. Therefore, it is crucial to understand how inappropriate parameters can lead to the appearance of specific failure defects. This study emphasizes fundamental fabrication methods and examines potential defects that may arise in the films due to improper process parameters.

The sol-gel thin film process flow is shown in Fig. 3.18. The preparation of the sol-gel solution begins with a tetraethyl orthosilicate (TEOS) : ethanol : H_2O ratio of 5.0 : 5.0 : 2.0. Acidic conditions are established by using hydrochloric acid to adjust the pH to around 1. Once the solution has been prepared, it is stirred for 30 min at 70°C to facilitate the reaction and then aged at room temperature for 1 h. This aging process promotes the formation of stronger siloxane bonds, enhancing the resulting material's stability and strength. Next, the substrate is cleaned with ethanol, heated at 150°C for 3 min, and subjected to plasma ashing. The cleaned substrate is then placed in a spin coater, and the coating is applied at 4000 rpm for 50 sec. This is followed by 10 min of pre-annealing in a nitrogen atmosphere in an annealing furnace at 1000°C. The final step involves annealing for 1 h under the same conditions as the pre-annealing process. This process allows for the formation of a uniform sol-gel silica film with a thickness of approximately 300 nm. Repeating the coating and pre-annealing steps for thicker silica films enables the creation of films that are several μm thick [111].

Table 3.1 Various conditions for fabricating sol-gel thin film

Parameter	L. Yang (2005) [45]	L. Yang (2005) [112]	F. Sigoli (2006) [111]	H. Hsu (2009) [113]	A. Maker (2012) [114]	H. Choi (2018) [46]	Our work
Water/TEOS (MTES) molar ratio	1-2	–	–	2	–	–	4.6
Stirring time	3 h	1 h	24 h	2 h	–	2 h, 24 h (aging)	30 min, 1 h (aging)
Cosolvent	2-propanol	Ethanol	Ethanol, PVA	Ethanol	Ethanol	Ethanol	Ethanol
Annealing temperature	1000°C	500-800°C	600°C, 1200°C	1000°C	1000°C	1000°C	1000°C
Annealing time	3 h	30 min[a]	5 min (600°C) 1 min (1200°C)[b]	3 h	1 h	1 h[c]	1 h
Film thickness	1 μm	–	13.50 μm (600°C) 4.30 μm (1200°C)	1.2 μm	0.35 μm	–	1.8 μm

[a] 60°C drying (5 min) before annealing
[b] 600°C annealing after each coating & 1200°C annealing after all coatings
[c] 75°C drying (5 min) before annealing

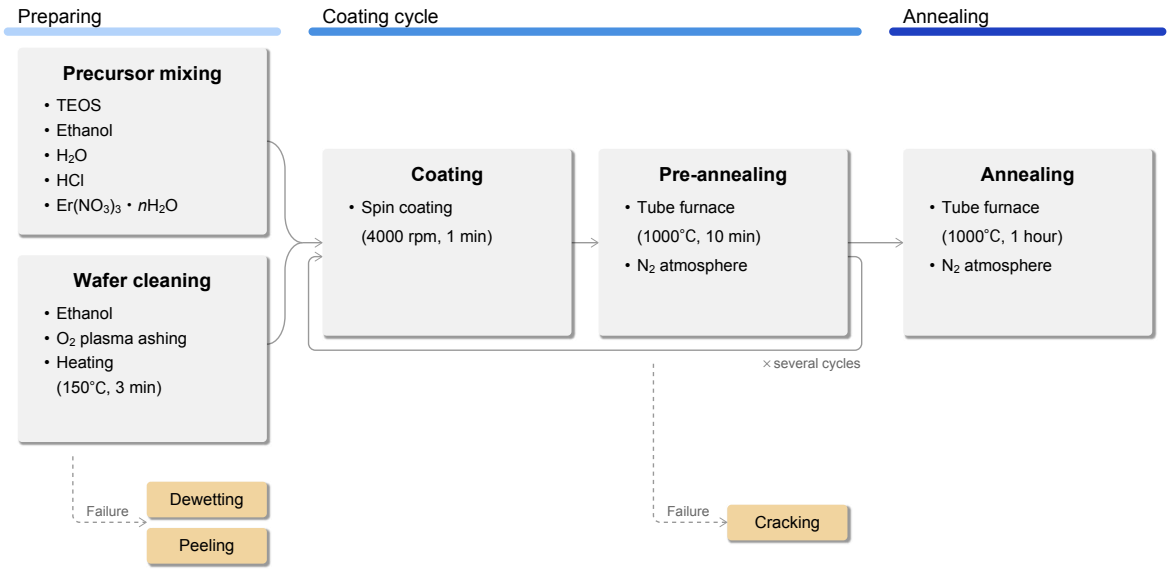

Fig. 3.18 The sol-gel thin film deposition process flow and common defects.

However, producing defect-free films is not guaranteed under the described parameters, as the fabrication environment also plays a critical role. Adjustments must be made to account for ambient temperature, humidity, and variations in equipment, such as the stirrers and annealing furnaces used in the fabrication process. Achieving uniform sol-gel films requires careful optimization of parameters such as solvent type, stirring time, and annealing conditions, all of which can vary considerably. Therefore, it is highly useful to understand troubleshooting strategies for addressing defects that may arise.

Figure 3.19 illustrates the types of defects that can occur in sol-gel films at various stages of the fabrication process. We found that these defects can be broadly categorized into three distinct types. In the following subsections, we will discuss the causes and potential solutions for each type of defect.

De-weting pattern

In the context of sol-gel films on substrates, an agglomeration state resembling raised droplets is referred to as a de-wetting condition (Fig. 3.19(a)), and it typically forms a hemispherical shape [115]. This defect has two primary causes. The first is an unsuitable substrate surface condition. If the substrate surface is not adequately cleaned and remains hydrophobic, the surface tension of the solution causes it to form droplet-like shapes. The second cause is the incomplete reaction of the solution. When the reaction time is too short, the polycondensation reaction remains incomplete, preventing the formation of a proper silica network.

If de-wetting occurs, the most effective solution is to improve the substrate surface treatment. An essential step is to perform sufficient plasma ashing (e.g., 1 min) before spin-coating the sol-gel solution, which removes organic contaminants from the substrate surface and increases its hydrophilicity. Additionally, the reaction time of the initial solution should be carefully adjusted.

Peeling pattern

As shown in Fig. 3.19(b), thin, mesh-like peeling can occur. A cross-sectional SEM image of this substrate is shown in Fig. 3.19(c). This phenomenon arises when the layers do not bond properly with each other. A poorly hydrophilic substrate surface is a primary cause of inadequate bonding between sol-gel layers. Additionally, while substances evaporated during annealing are generally removed, residual organic materials that are not fully eliminated can remain on the surface [116]. These residues interfere with the formation of vertical silica networks, leading to the observed peeling pattern.

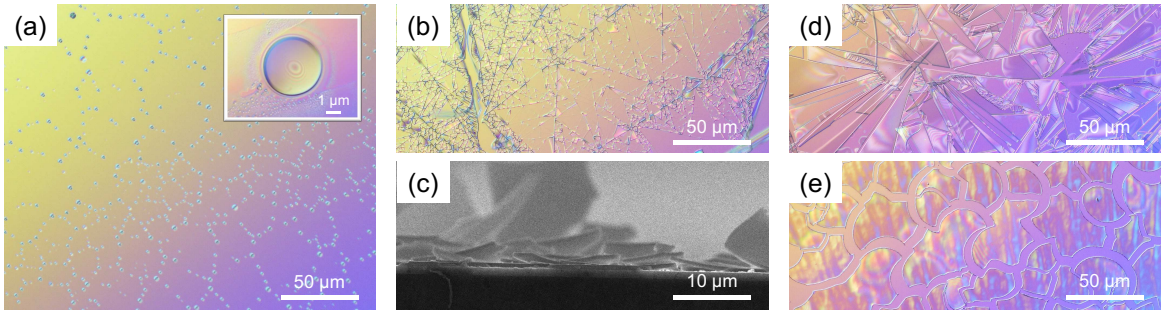

Fig. 3.19 Defects observed during sol-gel silica film deposition. Each image shows a different defect pattern: (a) a microscopic image of a de-wetting pattern (with the inset showing a magnified image), (b) a microscopic image of a peeling pattern, (c) a cross-sectional SEM image of a peeling pattern, (d) and (e) microscopic images of two types of cracking pattern. These patterns represent common issues encountered in thin film fabrication, resulting from different underlying causes.

A practical solution to this issue is to perform O_2 plasma ashing on the substrate surface before each layer is spin coated. Plasma ashing effectively removes organic residues, ensuring better adhesion between layers. When using this method, we observed no delamination, even when stacking multiple layers of films.

Cracking pattern

Among the observed defects, the most common is a pattern of cracks, as seen in the microscopic images in Figs. 3.19(d) and 3.19(e). These cracks are caused by excessive film thickness after spin coating, which leads to defects during annealing. As the sol-gel solution is spin-coated and then annealed, the solvent evaporates from the film, resulting in densification of the silica network and a reduction in film volume. If the annealing temperature is too low, this volume reduction induces structural instability, which results in cracks or delamination. Conversely, structural relaxation is more likely at high annealing temperatures of around 1000°C, which promotes uniform film formation. Therefore, it is preferable to place the coated substrate in a preheated annealing furnace rather than gradually increasing the temperature. Additionally, since the glass transition temperature of sol-gel films is approximately 600°C [117], the annealing temperature should exceed this threshold. Volume shrinkage during annealing can reach up to 20%, so each coating layer should be thin enough to allow structural relaxation to compensate for shrinkage. In this study, each layer is approximately 300 nm thick.

In Fig. 3.19(d), although the mixing ratio of the starting solution is optimal, an extended reaction time of 3 h results in an excessively thick film, which induces stress and contributes

to crack formation. An uneven film thickness or significant variations during spin coating can also cause these patterns. This unevenness arises from differences between the centrifugal forces at the center and the edges of the substrate during spin coating, which affect the solvent evaporation rate from the sol-gel solution. Evaporation begins as soon as the solution is dropped onto the silicon substrate and intensifies as the substrate spins, leading to a thickness difference of about 150 nm between the center and edges. Therefore, careful control of the solution's reaction time and spin-coating conditions is essential.

In Fig. 3.19(e), we observe patterns resembling "jigsaw puzzles" which we attribute to differences in water content in the starting solutions [118]. For this sample, the molar ratio of H_2O to TEOS in the starting solution is 3.0. According to the reaction formula (Fig. 3.16) and reaction efficiency, more than 4 moles of water per mole of TEOS are needed for a proper reaction. The cracks in this sample can thus be attributed to insufficient water content. This deficiency hinders the formation of the silica network, which is essential for structural integrity, as insufficient water limits the formation of the siloxane bonds (Si–O bonds) necessary for a robust silica network. Consequently, island-like cracks form, with larger island sizes observed in solutions with higher water content.

3.5 Erbium-doped silicon dioxide microtoroid

3.5.1 Film evaluation and microresonator fabrication

We fabricated an erbium-doped microtoroid after confirming the high quality of the defect-free ion-doped sol-gel film deposited on a silicon wafer. The fabrication process, illustrated in Fig. 3.20(a), follows a conventional photolithographic approach. As shown in Fig. 3.21, the microtoroid has a diameter of 60 μm and an erbium ion concentration of 2.0×10^{-18} cm^{-3}, comparable to commercial erbium-doped fibers.

Additionally, when a microtoroid is fabricated using a sol-gel thin film without erbium ion doping, it exhibits a Q-factor of approximately 10^7, similar to microtoroids made from thermally oxidized films [78].

It is important to note that, due to the limited thickness of sol-gel thin films, the fabrication method reported in previous studies is suitable for resonators with diameters of about 100 μm or less. The method described in the next section should be employed for larger toroid resonators.

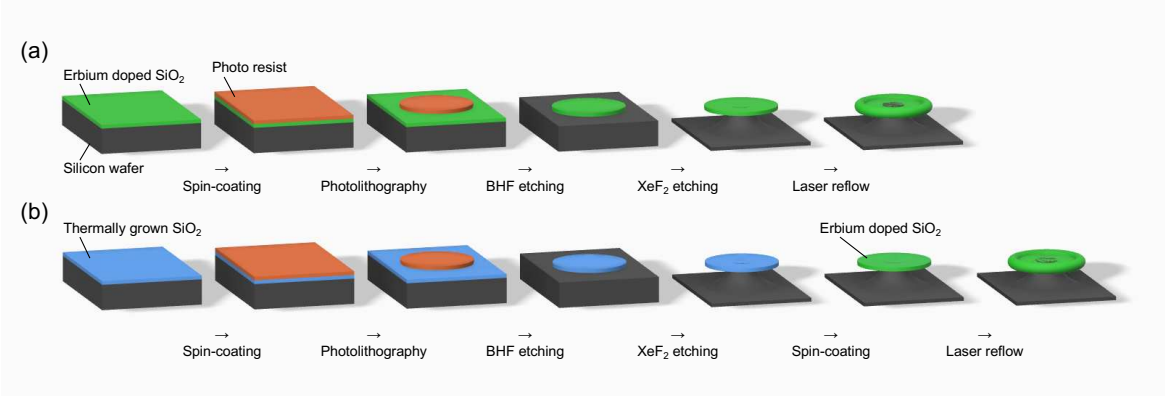

Fig. 3.20 (a) Schematic illustration of the process flow for fabricating a rare-earth ion-doped silica toroid from a thin sol-gel film. (b) Alternative fabrication method for a rare-earth ion-doped silica toroid by coating the surface of a pre-fabricated toroid with a sol-gel film.

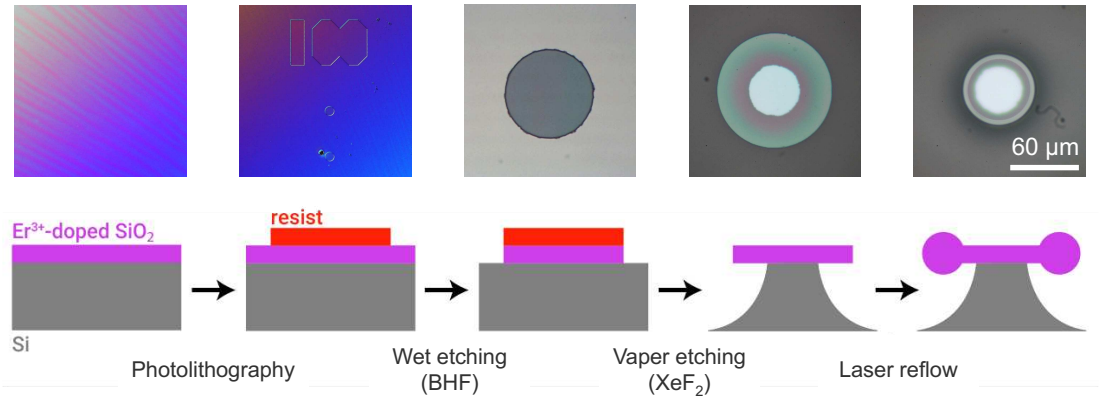

Fig. 3.21 Top-view microscopic images of a fabrication process and its corresponding process flow. A 60-μm-diameter Er^{3+}-doped microtoroid is fabricated from a sol-gel film with a thickness of 2.4 μm, coated in 8 layers, using a conventional process.

3.5.2 Coating the cavity for large-size Er-doped microtoroid fabrication

Fabrication

Next, we coated microstructures with sol-gel films. As shown in Fig. 3.20(b), the process flow involves coating a microdisk resonator with a sol-gel thin film and reflow using a CO_2 laser. When fabricating state-of-the-art silica disks or silica toroid resonators, as shown in Fig. 3.22, increasing the resonator diameter often results in buckling due to the mismatch between the thermal expansion coefficients of the silica film and the silicon substrate [119, 120]. To prevent buckling, it is known that the silica film thickness must exceed 5 μm. However, since each sol-gel thin film layer is limited to approximately 300 nm per coating, fabricating such a resonator using the method in Fig. 3.20(a) presents a challenge.

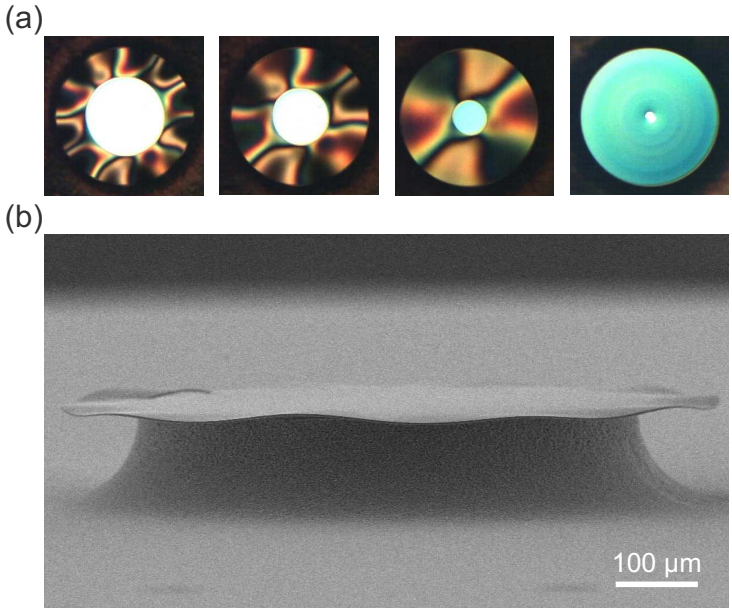

Fig. 3.22 (a) Top-view microscopic images of buckled silica disks (600 μm diameter and 2 μm silica film thickness). When the etching depth increases, the number of buckling distortions decreases. (b) A SEM image of a buckled silica disk resonator.

On the other hand, direct coating onto the silica disk resonator can circumvent the issue of buckling. In this experiment, we fabricated disk resonators with a diameter of 600 μm using an 8 μm thick thermally oxidized silica film, and no buckling was observed in these resonators. For coating, we used a spin coater set at 4000 rpm for 45 s, followed by annealing at 1000°C for 1 h. The fabricated device is shown in Fig. 3.23(a). The Q-value of the disk resonators before and after coating remained high at 1.2×10^6, indicating that the coating has

no impact on the resonator's performance. This coating method has significant potential for various applications, as it allows for ion activation without altering the resonator's quality.

Defects, as shown in Fig. 3.23(b), can occur during spin coating; however, coating without cracks is achievable by establishing an ethanol atmosphere inside the spin coater [121, 122]. Defects occur during coating due to non-uniform film thickness. Spin coating under an ethanol atmosphere is performed to achieve uniform film thickness.

After successfully obtaining the sol-gel activated silica disk, we employed CO_2 laser reflow, reducing the diameter to approximately 450 μm (Fig. 3.23(c)), as estimated from the measured free spectral range.

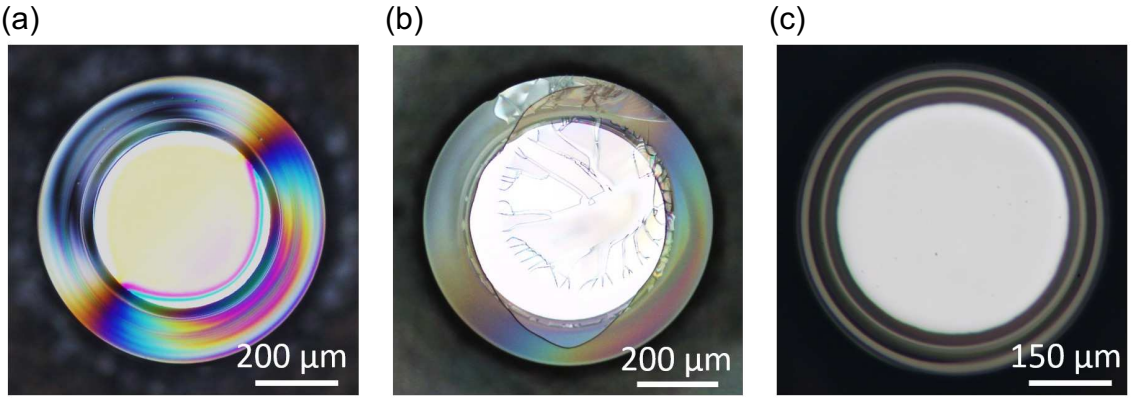

Fig. 3.23 (a) Silica microdisk coated with sol-gel film. (b) Silica micrdisk coated with sol-gel film but without ethanol atmosphere. (c) After reflowing (a).

3.5.3 Optical measurement of the sol-gel coated microtoroid

Lasing property

Using the resonator fabricated with the conventional method, we perform continuous-wave (CW) excitation at the 1480 nm band. We split the transmitted light from the resonator using a splitter and detect it with a power meter and an optical spectrum analyzer. The Q-factor of the resonator at the 1480 nm band measures 2.0×10^6. When we excite the resonator near a resonance wavelength of 1480 nm, we observe lasing oscillation at the 1550 nm band, as shown in Fig. 3.24(a). The wavelength spacing of the multimode lasing matches the FSR of 10 nm.

We also investigate the output-input curves for different doping concentrations, as shown in Fig. 3.24(b). When we vary the doping concentration from 0.85×10^{18} cm^{-3} to 1.7×10^{18} cm^{-3}, the lasing efficiency increases from approximately 0.6% to 1.0%.

On the other hand, the erbium-doped toroidal resonator with a diameter of 450 μm, shown in Fig. 3.23(c), exhibits a Q-value of 3.5×10^6 in the 1480 nm excitation mode. As the pump power is increased to excite the erbium ions, green up-conversion light is observed, indicating a good overlap between the erbium ions and the optical mode. When the pump power exceeds 350 μW, multi-mode laser oscillations are observed in the 1550 nm band. Thus, the lasing threshold is approximately 350 μW, with a lasing efficiency of 1.5%.

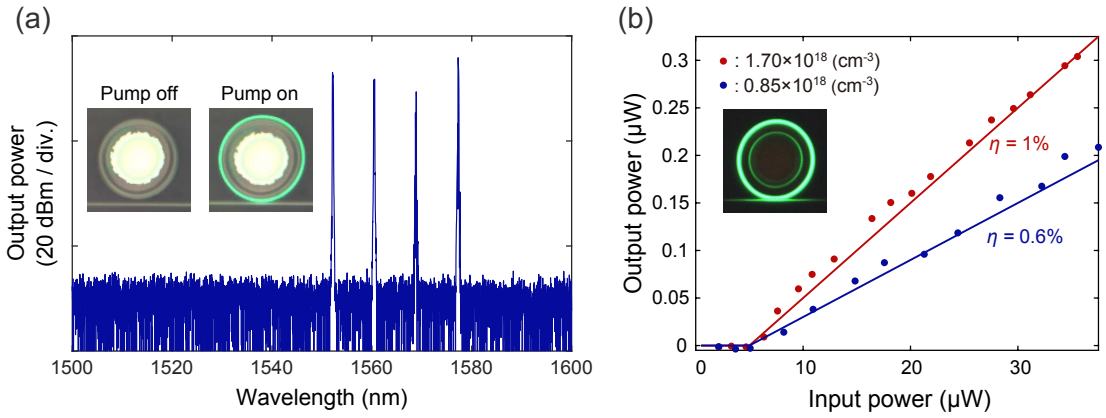

Fig. 3.24 (a) Laser emission spectrum of an Er^{3+}-doped microtoroid. This cavity lased around 1550 nm with a longitudinal mode spacing of 10 nm when it was pumped at 1480 nm. The inset image shows up-conversion luminescence of an Er^{3+}-doped microtoroid. (b) The output-input curves of Er^{3+}-doped microlasers with different concentrations. The red (blue) points and line indicate Er^{3+} concentration of 1.7×10^{18} cm^{-3} (0.85×10^{18} cm^{-3}).

Dispersion measurement

The transmission spectrum in the 1550 nm band for this cavity is shown in Fig. 3.25(a), with the red circles indicating the TE modes. We measured the dispersion of this cavity, as shown in Fig. 3.25(b) [41]. The blue dots represent the measured values, while the solid red line shows the fitting curve, which accounts for up to third-order dispersion. The dashed red line represents the theoretical dispersion curve for a silica microtoroid, assuming no erbium ion doping and identical major and minor diameters. The measurement results indicate that erbium ion doping has minimal impact on the dispersion, allowing the resonator to maintain anomalous dispersion.

Gain measurement

We fabricated Er^{3+}-doped SiO_2 toroids by the sol-gel method. We obtained a measured Q of $\sim 10^7$ when no Er^{3+} ions was doped. We made two resonators, both with the same

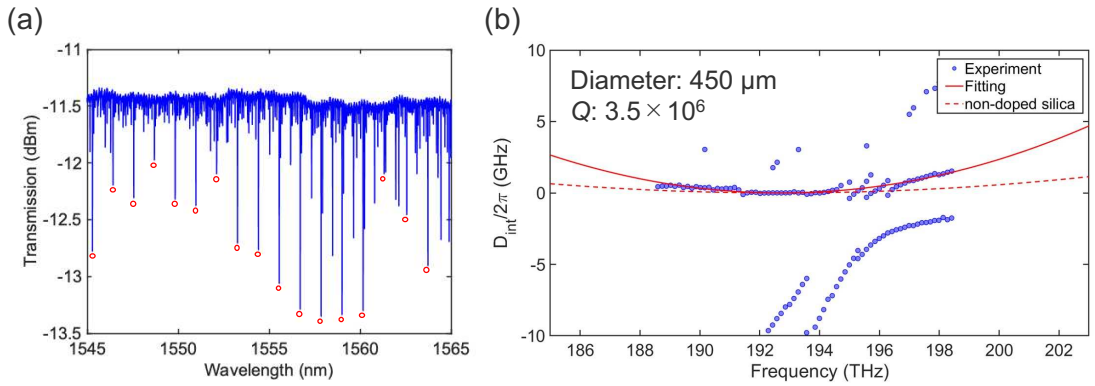

Fig. 3.25 (a) The transmission spectrum of the erbium-doped microtoroid in the 1550 nm band, with red circles indicating the fundamental TE mode. (b) Dispersion measurement results for the fundamental TE mode: blue dots represent the measured values, and the solid red line is the fitted curve. The dashed red line represents the theoretical dispersion values for a non-doped silica microtoroid with the same structure. Adding erbium ions has minimal impact on the dispersion.

diameter of $D \sim 60\ \mu$m, but with different Er^{3+} concentrations of 1.7×10^{18} cm^{-3} for device A and 0.85×10^{18} cm^{-3} for device B. The measured loaded Qs (i.e., in the presence of the Er absorption effect) of these two cavities were (device A): $Q_{\text{pump}} = 1.4 \times 10^6$ and $Q_{\text{lase}} = 1.1 \times 10^6$, and (device B): $Q_{\text{pump}} = 3.0 \times 10^5$, and $Q_{\text{lase}} = 1.1 \times 10^7$, where Q_{pump} and Q_{lase} are the Qs of the pump and lasing modes. We pumped the cavities at ~1485 nm and observed lasing at ~1550 nm, where the lasing power is shown as a function of the pump power in Fig. 3.24(b).

When we take account of the coupled-mode theory and upper-state population of Er ions based on rate equations, the slope η of the laser output-input power curve is theoretically given as[104],

$$\eta = \kappa_s^2 \left(\frac{\nu_s n_s V_m^s}{\nu_p n_p V_m^p} \right) \left(\frac{\alpha_p \left(\alpha_s + g_s^*\right) - \left(\alpha_p + g_p^*\right)\left(\alpha_s + \alpha_s^{\text{passive}}\right)}{\alpha_s^{\text{passive}} \left(\alpha_s + g_s^*\right)} \right) \cdot \left(\frac{4 n_p^2 \kappa_p^2 \left(\alpha_s + g_s^*\right)^2}{c^2 \left[\left(\alpha_p + \alpha_p^{\text{passive}}\right)\left(\alpha_s + g_s^*\right) - \left(\alpha_p + g_p^*\right)\left(\alpha_s + \alpha_s^{\text{passive}}\right) \right]^2} \right), \tag{3.10}$$

where ν, n, V_m, κ, and c are the light frequency, refractive index, mode volume, amplitude coupling coefficient between the resonator and the waveguide, and vacuum light velocity, respectively. Scripts p and s denote pump and signal modes, respectively. $\alpha_{s,p}^{\text{passive}}$ is the loss

(in m^{-1} units) determined by the loaded Q of a passive cavity without Er^{3+} doping for signal and pump modes($\alpha_s^{passive} = 2\pi n(\lambda_s Q_{load})^{-1}$). The absorption and gain (both in m^{-1} units) of Er^{3+} at a strong pump (i.e., $N_T = N_2$ and $N_1 = 0$) are theoretically given as,

$$\alpha_{s,p} = \Gamma_{s,p}\sigma^a_{s,p}N_T \ , \tag{3.11}$$

$$g^*_{s,p} = \Gamma_{s,p}\sigma^e_{s,p}N_T \ , \tag{3.12}$$

where N_T, σ^a, and σ^e are the overlap factors between the optical mode with a normalized Er^{3+} distribution, Er^{3+} concentration, absorption cross-section, and emission cross-section, respectively. In this study, we use previously reported values of $\sigma^a_p = 1.5\times10^{-21}$ cm^2, $\sigma^a_s = 2.8\times10^{-21}$ cm^2, $\sigma^e_p = 0.8\times10^{-21}$ cm^2, $\sigma^e_s = 4.8\times10^{-21}$ cm^2 [123]. For simplification, we assume $\Gamma_{s,p} = 1$ in our calculations.

By substituting Eqs. (3.11) and (3.12) into Eq. (3.10), we obtain graphs providing the relationship between N_T and η for different κ values, as shown in Fig. 3.26(a). These graphs enable us to estimate the effective N_T from an experimentally obtained η.

Once N_T is determined, we can obtain g_0 from Fig. 3.26(b). The gain can be estimated by solving the rate equation and propagation equation of an erbium-doped waveguide numerically. Hence, Fig. 3.26(b) is calculated as[123]

$$\frac{\partial P_{s,p}(z,t)}{\partial z} = \Gamma_{s,p}\left[\sigma^e_{s,p}N_2(t) - \sigma^a_{s,p}N_1(t)\right]P_{s,p}(z,t) \ , \tag{3.13}$$

$$\frac{\partial N_2(t)}{\partial t} = -\frac{N_2(t)}{\tau} - \frac{1}{A_{eff}}\left(\frac{\partial P_s(z,t)}{\partial z} + \frac{\partial P_p(z,t)}{\partial z}\right)N_2(t) \ , \tag{3.14}$$

$$N_1(t) + N_2(t) = N_T \ , \tag{3.15}$$

where P, N_1, N_2, and τ are the light energy (in units of photons), ground-level carrier density, excited-level carrier density, and carrier lifetime ($\tau = 10$ ms, in this study [123]), respectively. The gain saturates as we increase the pump power. Figure 3.26(b) is obtained by plotting the saturated gain g_0 as a function of N_T, where

$$g_0 = \Gamma_s\left[\sigma^e_s N_2(t) - \sigma^a_s N_1(t)\right]L \ . \tag{3.16}$$

$N_{1,2}(t_s)$ are the carrier densities in a steady-state calculated by using Eqs. (3.13)–(3.15), when the pump is sufficiently strong.

Figures 3.26(a) and 3.26(b) could be used as follows. If N_T is given, we can immediately obtain a theoretical gain g ($= g_0/L$) in units of m^{-1} from Fig. 3.26(b). On the other hand, Fig. 3.26(a) allows us to double-check the N_T value if we perform a lasing experiment,

as we demonstrated in Fig. 3.24(b). Figure 3.24(b) has a slope efficiency of $\eta = 1\%$ at an experimental Er^{3+} doping concentration of $N_T = 1.7 \times 10^{18}$ cm^{-3}. This corresponds to an effective N_T of 5.0×10^{18} cm^{-3} according to Fig. 3.26(a) and an experimentally estimated gain of $g = 1 \times 10^{-2}$ cm^{-1} from Fig. 3.26(b). On the other hand, the theoretical curve in Fig. 3.26(a) suggests that we should obtain a gain of $g = 3 \times 10^{-3}$ cm^{-1} at an $N_T = 1.7 \times 10^{18}$ cm^{-3} concentration. Although we do not know exactly why we obtained a slightly higher effective N_T, we think the values are in reasonably good agreement and within the experimental error.

Equations (3.13)–(3.16) also allow us to calculate g_0 versus P_s, at different P_p values, from which we can obtain P_{sat}^{g}, which is given as,

$$P_{sat}^{g} = \frac{1 + \dfrac{P_p \left(\sigma_p^a + \sigma_p^e\right) \tau}{A_{eff}}}{\dfrac{\left(\sigma_s^a + \sigma_s^e\right) \tau}{A_{eff} \hbar \omega_0}} . \tag{3.17}$$

P_{sat}^{g} is ~ 0.145 W when we assume a 500 mW pump and $D = 300$ μm. This value is used in the calculation, which is described in Chapter 4.

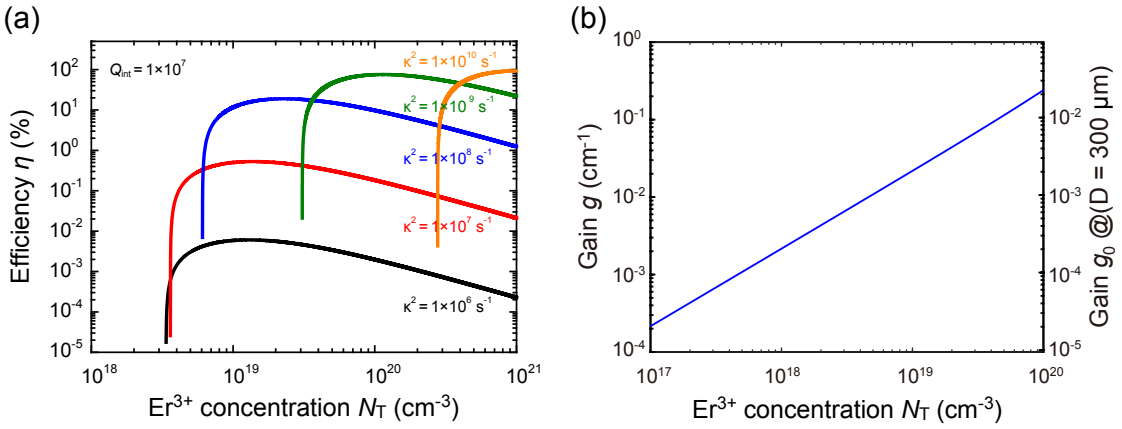

Fig. 3.26 (a) η versus N_T for different κ values ($\kappa = \kappa_p = \kappa_s$) at a cavity corresponding to $Q_{int} = 2 \times 10^7$ at 1550 nm. (b) Gain g (at saturating pump power) as a function of N_T. The vertical axis on the right is the saturated gain g_0 when $D = 300$ μm. We use $A_{eff} = 21$ μm^2 corresponding to a microresonator with $d = 30$ μm.

The gain of Er^{3+}-doped toroid resonators fabricated using two different methods is summarized in Table 3.2. Experimental results confirm that increasing the resonator diameter enhances the gain per round trip of the resonator.

Table 3.2 Parameters which measured and calculated to calculate the gain of fabricated resonators

Diameter	Fabrication	η	κ	N_{T}	g_{Tr}
60 μm	Conventional	1.0%	3.0×10^4	$2.0 \times 10^{-19}\mathrm{cm}^{-3}$	7.0×10^{-4}
450 μm	Coating	1.6%	2.0×10^4	$1.5 \times 10^{-19}\mathrm{cm}^{-3}$	3.0×10^{-3}

Chapter 4

Design and numerical analysis for passive mode-locking in microresonator system

Chapter 3 presents a comprehensive analysis of microresonator mode-locking dynamics through numerical simulations. The chapter begins with mode-locking behavior in a single microresonator, exploring the experimental feasibility of pulsed operation in a toroidal microresonator with gain and saturable absorption.

The second section extends the analysis to coupled microresonator systems, where mode-locking dynamics are influenced by inter-resonator coupling. Simulations reveal that in the vicinity of the exceptional point, system Q exhibits substantial modulation even with minor refractive index changes and a minimal Kerr effect contribution. We show theoretically and numerically that mode-locking is feasible with a coupled microresonator system with gain and loss, notably, without any natural saturable absorber.

4.1 Single cavity system

4.1.1 Introduction and motivation

Glass-based fiber lasers are excellent platforms for mode-locked ultrashort-pulse lasers because of their high beam quality, robustness, and simple configuration [124]. A gain medium and a mode-locker are the two key elements needed to build a mode-locked laser. Especially erbium-ion (Er^{3+}) doped fiber and carbon nanotubes (CNTs) are frequently used for these purposes in a fiber laser. Using a pulsed laser with a high repetition rate will open a new avenue to faster laser processing, higher capacity in optical communication, and more effective signal acquisition. Nonetheless, achieving a repetition rate above 1 GHz presents challenges, as the laser cavity length needs to be shortened to ensure the light pulses are

closely packed in time. Multi-gigahertz operation has been demonstrated using a 5 mm Fabry-Perot gain-doped fiber cavity, where the end surface is coated with CNTs as a saturable absorber (SA) [21]. However, further scaling of the repetition rate is impossible because the high pump power needed to compensate for the low gain can damage the CNTs.

Conversely, an ultrahigh-Q whispering-gallery-mode (WGM) microresonator has demonstrated its effectiveness as a platform for strong light-material interactions [39]. A WGM microresonator made of silicon dioxide on a silicon wafer has exhibited one of the highest Q values for greater than $\sim 10^8$. Since it is made of SiO_2, it is also a good host material for Er^{3+}-doping and will eventually provide a good platform on which to demonstrate a WGM microlaser [45, 104]. Continuous-wave (CW) lasing has been demonstrated at an ultralow threshold power, thanks to the high-Q.

Moreover, this type of WGM microresonator has also been demonstrated to generate dissipative Kerr solitons by applying CW pumping to one of the longitudinal modes. A four-wave mixing (FWM) process in a high-Q WGM microresonator generates an optical frequency comb. When a specific condition is met, we can lock all generated comb modes to create ultrashort pulses. These are attractive because dissipative solitons from a WGM microresonator have an extremely high repetition rate thanks to their small cavity size. However, these solitons are superimposed on a CW background, which complicates the pulse amplification necessary for using this light source as a seed in high-power applications. Additionally, achieving and stabilizing soliton pulses requires advanced wavelength sweeping and feedback mechanisms [15], adding complexity and increasing system costs.

If we can directly obtain mode-locked pulses from a small WGM microlaser, we would achieve background-free operation without using a complex feedback system. In addition to the CW lasing operation in a silica toroid WGM microresonator, SA is also confirmed with the same device by using CNTs (Fig. 4.1). So the combination of Er^{3+}-doped SiO_2 microtoroid with CNTs as the SA is of interest and has great potential in terms of realizing an ultracompact high-repetition-rate mode-locked pulse laser.

However, it is unclear whether we can demonstrate mode-locked operation in such a device since no experiments have yet been conducted with SiO_2 microtoroid for such a purpose, and the optimum parameter ranges are entirely unknown. Therefore, we aim to reveal the optimum range of parameters, such as the cavity size, Q, Er^{3+} ion concentration, dispersion, and nonlinear loss of the CNTs needed to achieve mode locking, and we discuss the experimental feasibility.

Previous studies have examined integrated mode-locked waveguide lasers on silicon substrates [18], yet our focus is on approaches using microresonators. Recent advancements in microresonators enable the utilization of ultrahigh Q factors and the novel doping of Er^{3+}

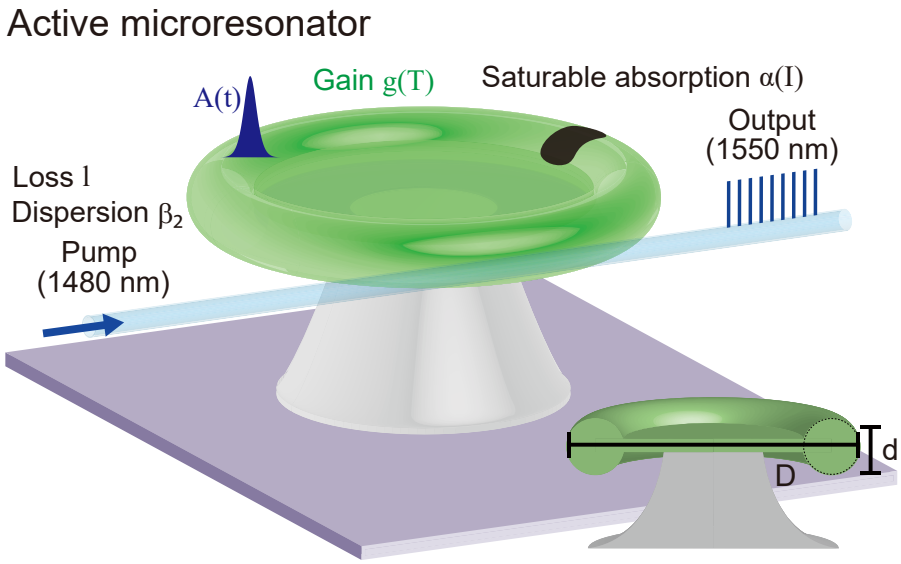

Fig. 4.1 An Er^{3+}-doped silica microtoroid resonator coupled with a tapered fiber that we studied numerically. Er^{3+} ions are doped by the sol-gel method, and CNTs are attached to the resonator's surface to enable saturable absorption.

ions in silica-on-silicon. We expect the high-Q to compensate for the limited gain of Er^{3+} ions and hence allow us to make the cavity size extremely small.

4.1.2 Theoretical model and parameters

Simulation model

Conceptually, a WGM microlaser is a miniaturized fiber ring laser. The system that we studied is shown in Fig. 4.1. The resonator is made of Er^{3+}-doped SiO_2 to enable gain, and it is fabricated by using the sol-gel method. CNTs are deposited on the surface of the resonator as a saturable absorber. A CW pump laser at 1480 nm is injected into the cavity, and the output light is coupled out by using a tapered fiber. Here, we define the intrinsic and loaded $Q(Q_{\text{total}})$ factors as follows. The intrinsic $Q(Q_{\text{int}})$ is the Q determined by the cavity losses, such as the scattering and absorption of the cavity. Typically, excess absorption losses from Er^{3+} ions and CNTs are omitted unless noted, as they are generally addressed separately in equations. The loaded Q is defined as

$$Q_{\text{total}}^{-1} = Q_{\text{int}}^{-1} + Q_{\text{ext}}^{-1}, \tag{4.1}$$

where $Q_{\mathrm{ext}} = \omega_0 \kappa^{-2}$ is the Q value determined by the coupling coefficient between the resonator and the tapered fiber (κ) and the angular frequency of the cavity resonance (ω_0). We solve the model based on the nonlinear Schrödinger equation as given by [125, 126]:

$$T_{\mathrm{r}} \frac{\partial}{\partial T} A(t,T) = \left(-iL\frac{\beta_2}{2}\frac{\partial^2}{\partial t^2} + iL\gamma_{\mathrm{NL}} |A|^2 \right) A(t,T) + \{ g_{\mathrm{T_r}}(T) - [l_{\mathrm{T_r}} + \alpha_{\mathrm{T_r}}(t,T)] \} A(t,T), \tag{4.2}$$

where A, t, and T are the slowly varying field envelope in the microcavity, short time, and long time, respectively. L, T_{r}, β_2, γ_{NL}, l, $g_{\mathrm{T_r}}$, and $\alpha_{\mathrm{T_r}}$ are the cavity length, one roundtrip time, second-order dispersion, nonlinear coefficient, linear loss per roundtrip (determined by the loaded cavity Q), net-gain of Er^{3+} per roundtrip, and nonlinear loss of the CNTs per roundtrip, respectively. Here, the nonlinear coefficient γ_{NL} was calculated using the nonlinear refractive index of silica $n_2 = 2.2 \times 10^{-20}$ m^2/W.

$$g_{\mathrm{T_r}}(T) = g_0 \left(\frac{1}{1 + \frac{\overline{|A(t,T)^2|}}{P_{\mathrm{sat}}^{g}}} \right) \left(1 + \frac{1}{{\omega_{\mathrm{g}}}^2} \frac{\partial^2}{\partial t^2} \right), \tag{4.3}$$

$$\alpha_{\mathrm{T_r}}(t,T) = \alpha_{\mathrm{ns}} + \frac{\alpha_0}{1 + \frac{\overline{|A(t,T)^2|}}{P_{\mathrm{sat}}^{\alpha}}}, \tag{4.4}$$

where g_0, P_{sat}^{g}, ω_{g}, α_{ns}, α_0, and $P_{\mathrm{sat}}^{\alpha}$ are the saturated net gain coefficient per roundtrip (hereafter referred to as gain), gain saturation power, gain bandwidth, non-saturable loss per roundtrip, modulation depth per roundtrip, and saturation power, respectively. ($\overline{|A(t,T)^2|}$) is the field intensity averaged over a short time t (i.e., average power in the cavity). We use the standard split-step Fourier method[40] to perform numerical simulations with a step size equal to the roundtrip time T_{r} for 1,500,000 roundtrips.

Parameters

The parameters of the system that we use in this calculation are summarized in Table 4.1. The cavity dispersion is given when the material and geometry of the cavity are determined [41]. We use a SiO_2 microtoroid, allowing us to calculate the dispersion by measuring the major diameter D and minor diameter d. (Fig. 4.1). The resonator is usually fabricated by laser reflow, and D/d is typically kept at about 10. Hence, we assume $d = D/10$ and calculate the dispersion, as shown in Fig. 4.1, and use these values for further calculations.

Table 4.1 Parameter values used in simulation

Parameter	Variable	Value	Unit	Source
Nonlinear refractive index	n_2	2.2×10^{-20}	m^2W^{-1}	Ref. [40]
Effective mode area	A_{eff}	var.	μm^2	Calculation
Second order dispersion	β_2	var.	ps^2/km	Calculation
Quality factor	Q	10^6–10^8	-	Experiments
Saturated gain	g_0	10^{-4}–10^{-1}	/roundtrip	Experiments
Gain saturation power	P^g_{sat}	var.	W	Eq. (3.17)
Gain bandwidth	$\omega_g/2\pi$	2.5	THz	Ref. [127]
Modulation depth	α_0	10^{-4}–10^{-1}	/roundtrip	Experiments
Non saturable loss	α_{ns}	0	/roundtrip	N.A.
Saturation power	$P^{\alpha}_{\text{sat}}/A_{\text{eff}}$	15	MW/cm^2	Experiments

In this calculation, we assume Er^{3+}-doped microtoroids for a $D = 300$ μm cavity. The saturation power of 15 MW/cm^2 and the modulation depth α_0 of 3.2×10^{-3} (details in §3.3 and Fig. 3.13). Therefore, we used $P^{\alpha}_{\text{sat}}/A_{\text{eff}} = 15$ MW/cm^2 and studied a modulation depth range of 10^{-4} to 10^{-1}. The gain per roundtrip (g_0) is theoretically calculated from the experimental results (detailed in §3.5.3); we investigate the $g_0 = 10^{-4}$ to 10^{-1} range.

4.1.3 Numerical calculation results and discussions

This numerical study aims to reveal the optimum parameters needed to achieve mode-locking operation in an Er^{3+}-doped WGM microresonator. We found four different states when we monitored the waveform under different conditions, as shown in Fig. 4.2. These four states are chaotic pulses (CP), multiple pulses (MP), a stable mode-locking regime (ML), and a continuous wave operation (CW). It is noted that, conventionally, mode-locking refers to phase coherence in the spectral domain; however, in this calculation, mode-locking is determined based on the peak-to-average power ratio ($P_{\text{peak}}/P_{\text{average}}$) and the temporal stability of this ratio. We are interested in the ML regime, where a single pulse circulates in the WGM resonator.

Quality factor dependence

In this section, we investigate key parameters, including saturated gain per round trip g_0 and nonlinear loss (modulation depth α_0) and Q-factor, for mode-locking using an Er^{3+}-doped microtoroid with $D = 300$ μm. Figure 4.3 shows the simulation results with gain and modulation depth as variables for intrinsic $Q = 10^7$ and 10^8. The red line indicates the

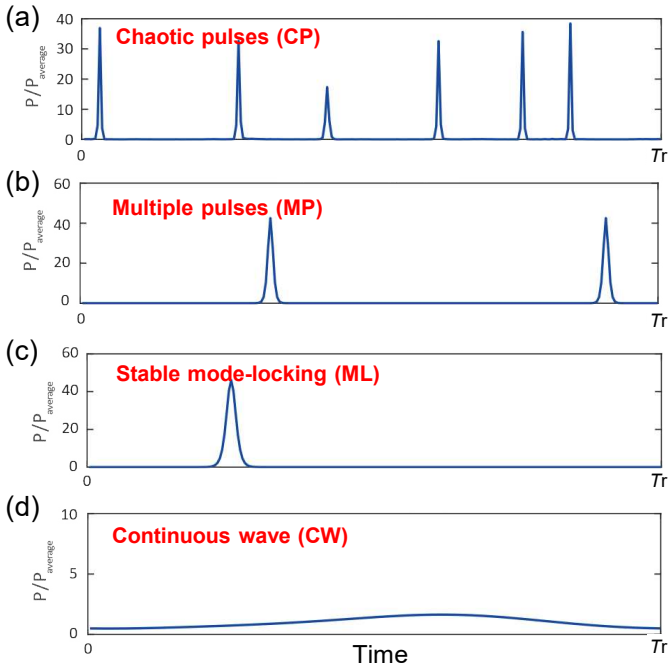

Fig. 4.2 Operation regimes were identified based on our four criteria: (a) chaotic pulses (CP), (b) multiple pulses (MP), (c) a stable mode-locked pulse (ML), and (d) continuous wave operation (CW).

estimation of g_0 when $N_T = 5.0 \times 10^{18}$ cm^{-3} of Er^{3+} ions concentration. It is noted that this parameter is achievable in experiments.

The regimes for the four different states (CP, MP, ML, and CW) are indicated in the figure 4.2. When the gain is low, the loss is larger than the gain, and the device will not lase. When the gain is greater than the loss, the device starts to oscillate a continuous wave. At a higher gain, along with an adequate modulation depth, the system exhibits ML operation. When we increase the gain even further, the pulse splits into multiple components and exhibits an MP state. Finally, the system is in an unstable regime at CP state when the gain is too high.

Figure 4.3(a) shows that the cavity exhibits CW lasing when Q is 10^7 at $g_0 = 10^{-3}$, which explains our CW lasing demonstration. However, it also shows that it is very challenging to achieve the ML state due to insufficient gain if we use this cavity. This situation will change if we use a cavity with a higher Q of 10^8, with which we should be able to reach the ML regime, as shown in Fig. 4.3(b). Although a Q of 10^8 is experimentally feasible, it is not easy to realize under Er^{3+}-doped conditions.

Therefore, we will look for another way to achieve ML, such as increasing the WGM microcavity laser diameter or designing the cavity dispersion. By increasing the cavity

diameter, we expect to obtain an increased gain per roundtrip. On the other hand, if we can make a cavity with a smaller dispersion, we expect that the mode-locking threshold will decrease. Both approaches will relax the cavity loss conditions for mode-locking.

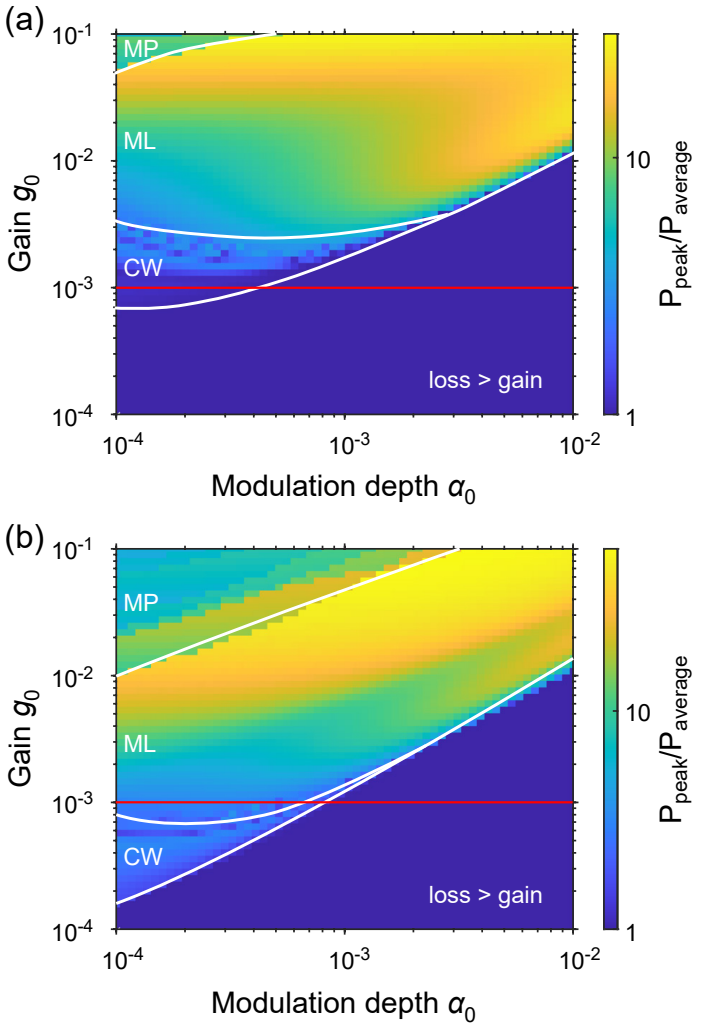

Fig. 4.3 Mode-locking investigation of $D = 300\ \mu$m Er^{3+}-doped microtoroid with nonlinear loss as parameters. (a) Calculation results for $Q = 10^7$ and (b) for $Q = 10^8$. The red line shows the position of the theoretical gain at $N_T = 5.0 \times 10^{18}$ cm^{-3}.

Cavity size and dispersion dependence

As discussed previously, a sufficiently large g_0 is crucial for achieving ML. An alternative way of increasing g_0 is to increase the size D of the microresonator. This approach appears to be straightforward, but the presence of dispersion makes the optimization more complex[41]. The calculated dispersion is at its minimum at $D \sim 150\ \mu$m but becomes anomalous disper-

sion when we increase the cavity size. A smaller dispersion is usually advantageous for easy mode-locking because of the stronger self-phase modulation that occurs at a lower intracavity power. Self-phase modulation is normally needed to achieve mode-locking. On the other hand, we prefer a larger cavity size because of the larger gain. Therefore, it appears that there is a tradeoff between gain and dispersion when we change the cavity size, and there may be an optimum point.

First, we investigated only the dispersion effect. Namely, we assumed that we could fix the diameter of the toroid microresonator at 300 μm but could change the dispersion. Figure 4.4(a) shows the numerical results we obtained when we fixed the modulation depth α_0 and Q at 5×10^{-4} and 10^7, respectively. As expected, ML is possible even with a small g_0 when the dispersion is close to zero. Unfortunately, in this case, however, the dispersion of a 300 μm diameter toroid is about -20 ps^2/km, which is outside the ML regime.

Second, we performed further numerical investigations at different cavity diameters D for a cavity where Q was fixed at 10^7. The dispersions for a cavity with different Ds are taken from the calculation. Increasing the diameter will increase the gain per roundtrip but result in a larger dispersion. On the other hand, the decreasing diameter will reduce the gain per roundtrip but achieve a weaker anomalous dispersion. Since these two approaches appear to have a tradeoff relationship, we confirmed which design approach was more suitable for passively mode-locking a WGM micro-laser. The result is shown in Fig. 4.4(b).

Figure 4.4(b) shows interesting behavior. As expected, the CW lasing threshold decreases as we increase the cavity diameter since the gain increases. However, the ML threshold is not sensitive to the diameter, and it is almost constant when $D > 300$ μm. This is encouraging because it tells us that ML is possible even with a small cavity, which is usually more challenging. Taking into consideration that a larger diameter WGM toroid resonator is often more difficult to fabricate[120], we concluded that the target diameter of the cavity is $D = 300$ μm, but with a slightly higher intrinsic Q and higher doping concentration.

Moreover, our results also suggested another approach, namely dispersion control. If we can shift the null dispersion point at a large D, we should be able to reduce the ML threshold since we can use a larger cavity. Throughout this study, we kept $D/d = 10$, but we might change this ratio (a larger D with a smaller d) by adjusting our laser reflow condition.

4.1.4 Conclusion

In conclusion, we numerically investigated the passive mode-locking of a toroidal WGM microlaser. The small cavity size allows for ultrahigh repetition rates; however, the gain per roundtrip is minimized, so ultra-high Q microresonators are necessary. Moreover, dispersion

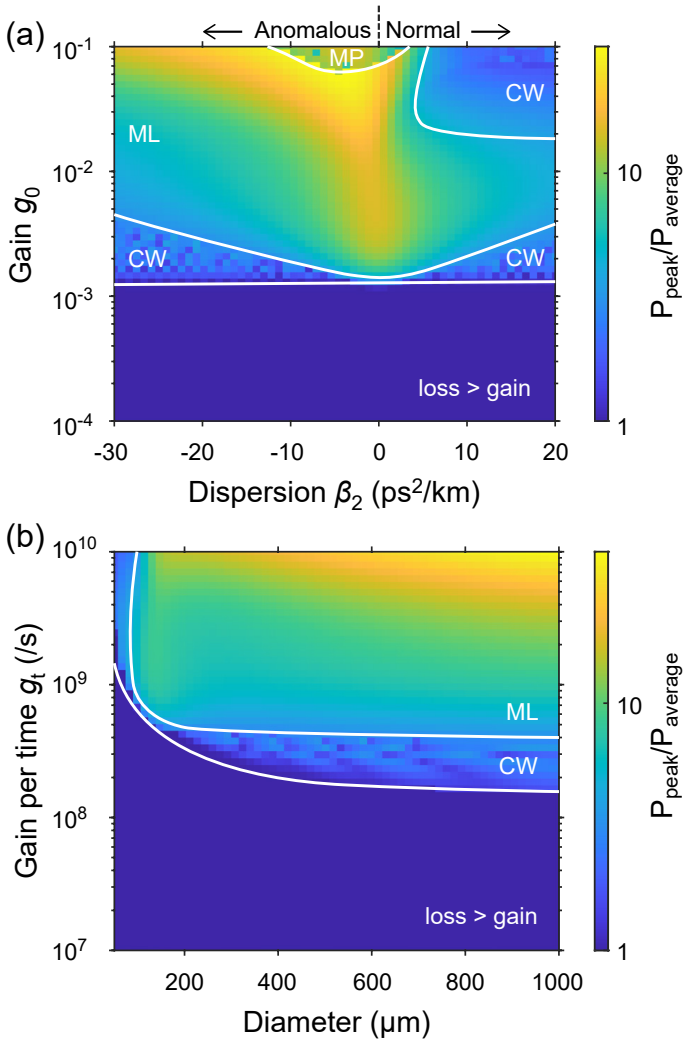

Fig. 4.4 (a) Modelocking investigation of a 300 μm diameter toroidal microresonator for $Q = 10^7$, with gain per roundtrip (g_{T_r}) and dispersion (β_2) as parameters. (b) Mode-locking investigation for toroid microcavities ($Q = 10^7$) with different diameters D while $D/d = 10$ is maintained. Note that the vertical axis is now gain per second (g_t), where $g_t = g_0/T_r$. The value is at $g_t = 2.2 \times 10^8$ s^{-1} when $g_0 = 10^{-3}$ and $D = 300$ μm ($T_r = 4.5$ ps).

plays an essential role in mode-locking: a weak anomalous dispersion promotes mode-locking operation with a limited gain.

In addition, the tradeoff relationship between gain and dispersion was highlighted due to their dependence on microresonator diameter. As a result, a 300 μm diameter WGM microlaser with a Q slightly higher than 10^7 proves to be a promising platform for a microlaser with an ultra-high repetition rate exceeding 100 GHz.

4.2 Coupled cavity system

This section describes the feasibility of mode-locking in a coupled cavity system with gain and loss, achieved without relying on a natural saturable absorber. Describing this system requires a non-Hermitian model with complex eigenvalues and non-orthogonal eigenstates rather than a conventional Hermitian model with real eigenvalues and orthogonal eigenstates. Tuning the parameters of this dissipative system can cause its complex eigenvalues and eigenstates to coalesce, forming a non-Hermitian degeneracy known as an exceptional point (EP). In the vicinity of the exceptional point, system Q exhibits substantial modulation even with minor refractive index changes and a minimal Kerr effect contribution. Leveraging this unique behavior, we propose an unprecedented approach wherein the lossy auxiliary cavity functions as an efficient artificial saturable absorber, thus facilitating mode-locking. This approach is novel and presents considerable advantages over conventional systems where both gain and saturable absorption are contained within a single microcavity. These benefits include reduced operational power and ease of post-adjustment, achievable through the manipulation of the coupling strength between the two microcavities.[1]

4.2.1 Introduction and motivation

Passively mode-locked pulsed lasers have emerged as essential tools in a variety of applications, including ultrafast laser spectroscopy and coherent control [128, 129], femtosecond laser processing [130, 131], attosecond physics [132, 133], time and frequency standards [134], and telecommunications [135]. Shortly after the invention of the laser, research into short-pulse generation was conducted [136], and mode-locking using saturable absorption (SA) was developed. Early laser systems employed laser dyes [137] and semiconductor saturable-absorber mirrors (SESAMs) [138], both of which rely on natural SA. For a long time, Kerr-lens mode-locking [139], a technique utilizing the self-focusing effect to create artificial SA, has been used for mode-locking in solid-state lasers. In recent years, the emergence of fibre lasers, which capitalize on both natural and artificial SA effects achieved through carbon nanotubes (CNTs) [140], graphene [141], nonlinear polarization rotation [8], nonlinear loop mirror [142], and Mamyshev oscillator [143, 144] has made ultrashort pulse lasers more accessible.

In recent times, the demand for high-repetition pulsed lasers has surged [39, 145–147] as they enable more effective data acquisition and faster material processing speed. Consequently, researchers have developed harmonic mode-locking techniques in fibre lasers [148],

[1] Contents presented in this section has been published in "Exceptional point proximity-driven mode-locking in coupled microresonators," Optics Express, Vol. 32, No. 13, pp. 22280-22290 (2024).

short-cavity solid-state lasers [4], mode locked integrated external-cavity surface-emitting lasers [149], and Er^{3+} doped fibre-ferrule cavities [21]. Among these, nanophotonic devices fabricated from erbium-ion (Er^{3+}) doped glass [150, 78] stand out as potential cost-effective solutions, given the maturity and robustness of the material. These devices are particularly promising if a small mode-locked cavity can be fabricated. Therefore, a mode-locked laser using a whispering-gallery-mode (WGM) microresonator [92], could provide a cost-effective on-chip solution for demonstrating ultra-high repetition rate optical pulses. However, the realization of SA in such a system, without sacrificing essential parameters such as the cavity quality factor (Q), poses a challenge if we choose to utilize CNTs or graphene. Hence, it is essential to develop an entirely new approach for achieving artificial SA and enabling passive mode-locking, especially if we aim to realize femtosecond pulse laser sources in nanophotonic devices.

At the same time, systems consisting of coupled resonators with gain and loss have been garnering interest and are being investigated for their ability to break parity-time (PT) symmetry in structures such as waveguides [151], photonic crystals [152], and microrings[153, 102, 154]. It has been proven that a coupled cavity resonator can achieve low-threshold lasing when operated beyond exceptional points (EPs), where eigenfrequencies coalesce [101]. This is due to a significant reduction in system loss. Notably, the system loss in such configurations exhibits considerable modulation near an EP.

In this work, we theoretically propose and numerically demonstrate passive mode-locking in a coupled-cavity system with gain and loss. Previous research has demonstrated self-pulsation in a similar setup, where inherent SA within a lossy cavity was enhanced through dynamic decoupling of the cavities[155]. Our findings, however, reveal that inherent natural SA is unnecessary when we exploit the unique properties arising near the EP. By exploiting the extensive system loss modulation that occurs close to the EP, we achieve efficient artificial SA, leading to ultrahigh-repetition mode-locking in a small cavity system. We also anticipate that the required quality factor (Q) of the system will be substantially relaxed thanks to the separation of gain and loss in two distinct cavities. Moreover, we introduce a new parameter: the coupling rate between the two microcavities. This additional control point should facilitate easier experimental demonstration.

4.2.2 Coupled cavities for mode-locking

Concept and operational mechanism

Our model system, as depicted in Fig. 4.5(a), is a pair of coupled microresonators. The first resonator, cavity A, provides gain, while the second one, cavity B, is a passive microresonator

with the same diameter as cavity A but with a higher loss (low Q). The difference between the Q values of the two resonators should be noted because the distinction is crucial as regards the mode-locking mechanism explored in this study.

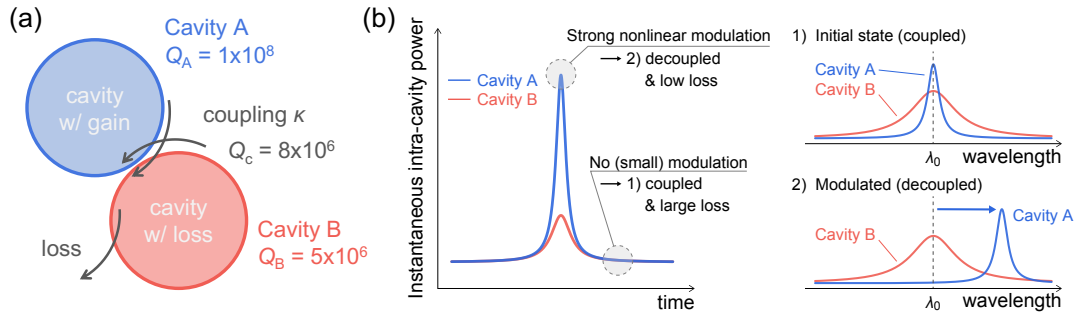

Fig. 4.5 Model and principle. (a) Schematic representation of our model. Cavity A is a cavity with gain; Cavity B is a lossy cavity. Light is generated in Cavity A and undergoes loss in Cavity B. (b) Explanation of the principle of artificial SA in a coupled cavity system. The left graph shows the temporal waveform in Cavity A (blue line) and Cavity B (red line). The pulse intensity in Cavity A is consistently higher due to its gain properties. At the pulse's peak, Cavity A exhibits strong nonlinearity, leading to modulation in the refractive index. In contrast, the tail (or background) remains linear. The right graphs show the resonant spectra for both cavities at the peak and tail of the pulse. Initially, at the tail of the pulse, Cavities A and B couple with each other since they share the same resonant wavelengths. However, as the peak of the pulse in Cavity A demonstrates significant optical nonlinearity, it causes a shift in resonant wavelengths between the two cavities, resulting in their decoupling. Consequently, the light in Cavity A experiences reduced loss.

With gain provided by cavity A, single and multi-mode lasing can be achieved when a pump is applied. However, only a continuous wave (CW) lasing is obtained in the absence of an SA effect. Figures 4.5(a) and 4.5(b) show how our system can exhibit an artificial SA that contributes to pulsing. Given the coupled nature of cavities A and B, and the lossy attribute of cavity B, the light from cavity A couples into cavity B, leading to its elimination due to the low-Q; an observation suggesting that we can reduce system loss if we can manage the decoupling of the two cavities.

The influence of the Kerr effect, characterized by an intensity-dependent, instantaneous refractive index change, such as,

$$n = n_0 + n_2 I, \tag{4.5}$$

where n_2 is the nonlinear refractive index, and I the intensity, is evident when examining a pulse circulating within the cavity. With gain in cavity A and $Q_A > Q_B$, the pulse peak shows pronounced nonlinear refractive index modulation in cavity A, causing disparate resonant frequency modulations in the two cavities, as explained in Fig. 4.5(b). This results in an

instantaneous decoupling of the cavities at the pulse peak; this is an intuitive explanation despite the challenge of defining an instantaneous resonant frequency within a round trip. Rigorously, this decoupling can also be viewed as a phase velocity mismatch caused by the Kerr effect. With initially identical resonant frequencies, cavities A and B experience modulation and decoupling only at the pulse peak. As a consequence, the light within cavity A undergoes decreased loss at the pulse peak, thereby replicating the operation of SA behaviour.

The primary challenge is to secure a substantial degree of coupling/decoupling modulation under conditions of minor refractive index modulation, given that n_2 is typically small. To surmount this challenge, we propose exploiting the potent modulation commonly observed near an EP in a coupled microresonator system.

Numerical model

To investigate the new mode-locking technique that forgoes the use of any natural SAs, we have constructed a model utilizing the approach described below with nonlinear Schrödinger equations with gain [92] and mode coupling terms [156], such as,

$$\begin{aligned} &T_{\mathrm{r}}\frac{\partial A(t,T)}{\partial T} \\ &= iL\left(-\frac{\beta_2}{2}\cdot\frac{\partial^2}{\partial t^2}+\gamma_{\mathrm{NL}}\left|A(t,T)\right|^2\right)A(t,T)+\frac{g_{T\mathrm{r}}(T)-l_{\mathrm{A}}}{2}A(t,T)+i\frac{\kappa}{2}B(t,T), \end{aligned} \tag{4.6}$$

$$T_{\mathrm{r}}\frac{\partial B(t,T)}{\partial T} = iL\left(-\frac{\beta_2}{2}\cdot\frac{\partial^2}{\partial t^2}+\gamma_{\mathrm{NL}}\left|B(t,T)\right|^2\right)B(t,T)-\frac{l_{\mathrm{B}}}{2}A(t,T)+i\frac{\kappa}{2}A(t,T), \tag{4.7}$$

where $A(t,T)$ and $B(t,T)$ are the complex electrical field amplitudes (in a slowly-varying envelope approximation) in cavities A and B. Here, t and T are the fast time and the slow time, respectively. Equations (4.6) and (4.7) are interconnected through the last term, with $\kappa=\omega_0/Q_{\mathrm{c}}$ representing the coupling rate, where Q_{c} is the coupling Q. $\gamma_{\mathrm{NL}}(=n_2\omega_0(cA_{\mathrm{eff}})^{-1})$ is the nonlinear coefficient. $g_{T\mathrm{r}}(T)$, and $l_{\mathrm{A,B}}$ are the gain per roundtrip in cavity A, and losses per roundtrip in cavities A or B, as below [92],

$$g_{T\mathrm{r}} = g_0\left(\frac{1}{1+\frac{\overline{|A(t,T)|}^2}{P^g_{\mathrm{sat}}}}\right)\left(1+\frac{1}{\Delta f_g^2}\frac{\partial^2}{\partial t^2}\right), \tag{4.8}$$

$$l_{\mathrm{A,B}} = T_{\mathrm{r}}\gamma_{\mathrm{A,B}} = T_{\mathrm{r}}\cdot\frac{\omega_0}{Q_{\mathrm{A,B}}}, \tag{4.9}$$

where the parameters are described in Tab. 4.2. When A is nonzero, the last term on the right-hand side of Eq. (4.6) can be rewritten as follows,

$$i\frac{\kappa}{2}B = \left[\text{Real}\left(i\frac{\kappa}{2}\frac{B}{A}\right) + i\cdot\text{Imag}\left(i\frac{\kappa}{2}\frac{B}{A}\right)\right]A, \tag{4.10}$$

where the real part (the first term) corresponds to gain and loss, whereas the imaginary part (the second term) pertains to the phase modulation, both arising due to the coupling. Given that A and B are functions of time t, Eq. (4.10) shows that the effective gain and loss emerging as a result of the coupling constitute a time-dependent function and may act as an artificial SA.

Table 4.2 Parameters employed in the calculations unless otherwise specified in the text

Parameter	Variable	Value of A	Unit
Intrinsic Q of Cavity A	Q_{A}	1×10^{8}	–
Intrinsic Q of Cavity B	Q_{B}	5×10^{6}	–
Coupling Q	Q_{c}	8×10^{6}	–
Cavity diameter	$D(=L/\pi)$	300	μm
Resonant wavelength	$\lambda_0(=2\pi c/\omega_0)$	1.55	μm
Roundtrip time	T_{r}	4.52	ps
Refractive index	n_0	1.44	–
Nonlinear refractive index	n_2	2.2×10^{-20}	m^2/W
Effective mode area	A_{eff}	21.28	$\mu\mathrm{m}^2$
Second order dispersion	β_2	-12.24	$\mathrm{ps}^2/\mathrm{km}$
Saturated gain	g_0	5×10^{-2}	/roundtrip
Saturation power	$P_{\mathrm{sat}}^{\mathrm{g}}$	144.8	mW
Gain bandwidth	Δf_{g}	2.50	THz

Equations (4.6) and (4.7) are solved using the split-step Fourier method, which is a technique widely adopted for calculations involving microresonator frequency combs [156]. As laid out in Tab. 4.2, we adopt a silica toroid microresonator with a diameter of $D = 300$ μm for our model. We only doped cavity A with Er^{3+} ions to produce gain, setting the Q_{A} and Q_{B} values at 1×10^{8} and 5×10^{6}, respectively. Cavities A and B are coupled with a coupling Q of $Q_{\mathrm{c}} = 8\times10^{6}$. We assume a saturated gain g_0 of 5×10^{-2} per roundtrip, which can be achieved with an Er^{3+} concentration of approximately 10^{20} cm^{-3} [92]. Parameters for dispersion and mode area are obtained from the given structure, with the minor diameter of the toroid specified as 30 μm. We note that both cavity exhibit the identical anomalous dispersion value ($\beta_2 = -12.24$ $\mathrm{ps}^2/\mathrm{km}$).

4.2.3 Results and Discussion

Demonstration of the mode-locking

The results of our computation are shown in Fig. 4.6(a), where we chart the average power within each cavity (P_{aveA} and P_{aveB}) as a function of the number of roundtrips after starting the cavity pump. As multimode lasing begins, the longitudinal modes remain unlocked, and the temporal waveform undergoes a random modulation (Fig. 4.6(b)). Following several thousand round trips, we begin to observe the formation of a pulse, albeit an unstable one (Fig. 4.6(c)). It takes approximately 7×10^4 round trips for the cavity to reach a state of complete stability.

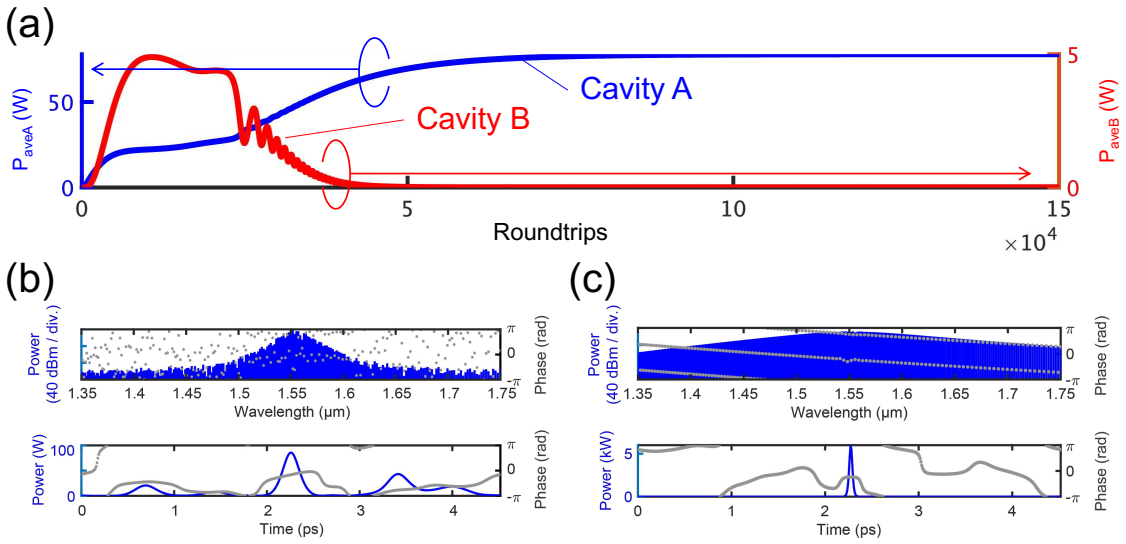

Fig. 4.6 Calculation results obtained from coupled nonlinear Schrödinger equations. (a) The average optical power in Cavity A (blue) and Cavity B (red) as a function of the roundtrips. (b) Spectral intensity and phase, alongside temporal intensity and phase, within a roundtrip at roundtrip 10,000. (c) At roundtrip 30,000.

The stable temporal waveforms for cavities A and B are shown in Figs. 4.7(a) and 4.7(b), respectively. At this juncture, we witness clear mode-locking behaviour. The pulse shape has a sech^2 profile with a full-width at half maximum (FWHM) of 30 fs. The phase of the pulse reveals it to be Fourier transform-limited, providing direct evidence of mode-locking, with a corresponding spectral width of 84 nm (FWHM).

Here, we confirm that the Kerr effect instigates instantaneous decoupling, and thus serves as an artificial SA. Figures 4.7(c) and 4.7(d) show the associated resonant wavelength shifts for the waveforms shown in Figs. 4.7(a) and 4.7(b), calculated via instantaneous nonlinear refractive index modulation as given in Eq. (4.5). The outcome indicates that the resonance

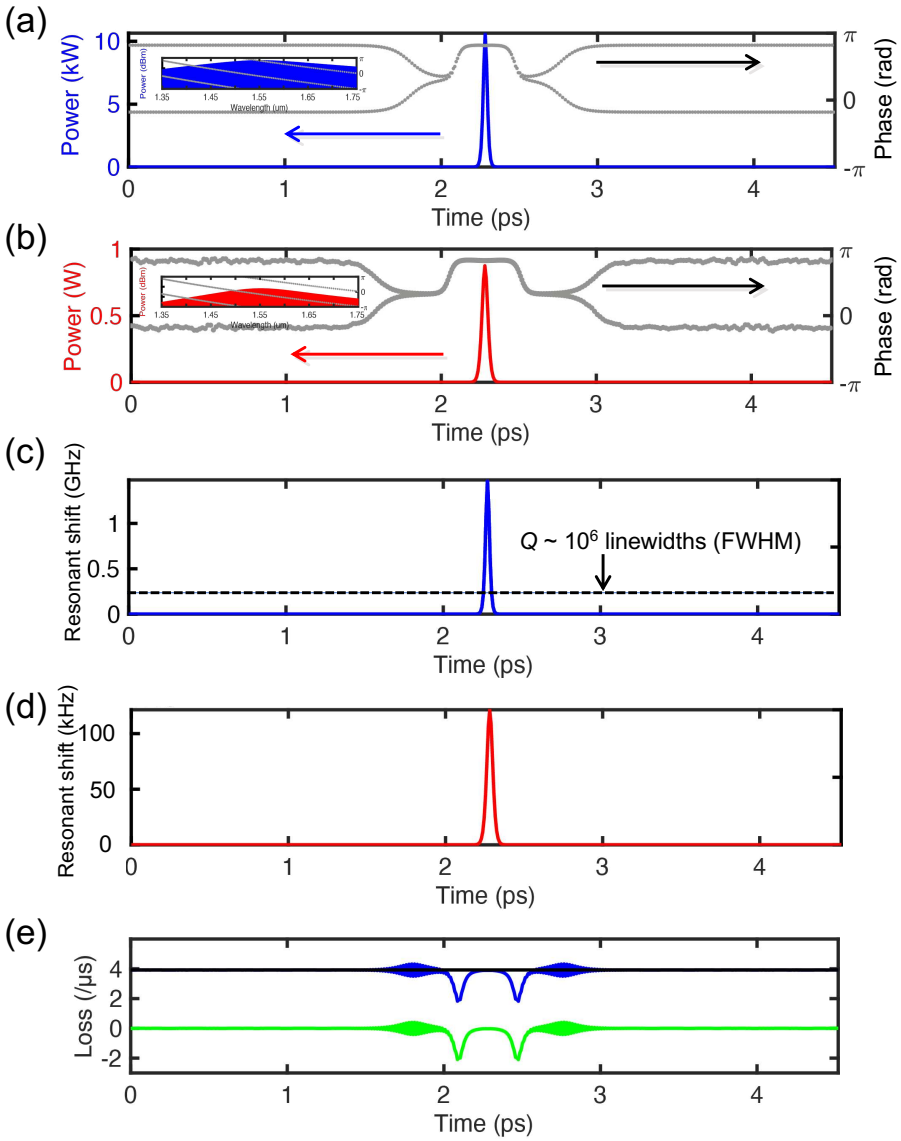

Fig. 4.7 (a) Mode-locked temporal waveform and spectrum (inset) in Cavity A at roundtrip 70,000. The blue line represents intensity, while the grey lines show the phase. (b) As (a), but for Cavity B. (c) Calculated resonant shift for Cavity A resulting from Kerr nonlinear refractive index modulation. A maximum frequency shift of ~ 1.5 GHz is observed at the pulse peak. The black dotted line indicates the frequency linewidth (FWHM) for a cavity with a Q of 10^6. (d) As (c) but for Cavity B. (e) The nonlinear loss and gain profile in Cavity A arising from the system's coupling and decoupling within the roundtrip. The black solid line depicts the net gain in Cavity A (i.e., g_0 minus the loss Q_A). The green line shows the extra loss in Cavity A due to its coupling with Cavity B. The blue curve portrays the overall net gain/loss profile in Cavity A. The green and blue curves are applicable only when the intensity within cavity A is nonzero.

of cavity A effectively undergoes a frequency shift of up to 1.5 GHz. This shift surpasses the linewidth of cavity B (with $Q_B = 5 \times 10^6$). Given that the shift in cavity B is negligible (Fig. 4.7(d)), we can instantaneously decouple cavity A from cavity B only at the pulse peak. This process results in minimal loss and allows the presence of the auxiliary cavity B to function as an artificial SA.

Figure 4.7(e) offers greater clarity by depicting the effective gain and loss experienced by cavity A due to its coupling with cavity B within a roundtrip. The loss is clearly negligible at the pulse peak and subsequently increases at the pulse tail. This finding reinforces our previous conclusion that the coupled cavity system indeed realizes an artificial SA. However, a lingering question persists: why does the SA occur so effectively with this parameter set? Generally, the n_2 value is small, implying that the modulation would only occur to a limited extent. To answer this question, it becomes crucial to exploit the impact of the EP within this system.

4.2.4 The impact of the exceptional point

Upon a closer examination of the temporal phase in Fig. 4.7(b), a unique structure is observable where the phase bifurcates before consolidating into one as the intensity ascends. In an attempt to comprehend this behaviour, we undertake a steady-state analysis of our coupled cavity system.

To simplify the picture, we consider two cavities; one with low loss (cavity A, with $Q_A = 10^8$) and the other with high loss (cavity B, with $Q_B = 5 \times 10^6$). A coupled-mode analysis is then performed based on the following expressions [101]:

$$\frac{dA}{dt} = i\omega_A A - \frac{\gamma_A}{2}A + i\frac{\kappa}{2}B, \tag{4.11}$$

$$\frac{dB}{dt} = i\omega_B B - \frac{\gamma_B}{2}B + i\frac{\kappa}{2}A. \tag{4.12}$$

At a steady state, the complex eigenfrequencies are given as,

$$\omega_\pm = \frac{\omega_A + \omega_B}{2} + i\frac{\chi}{2} \pm \beta, \tag{4.13}$$

where, χ is the average decay rate given by $\chi = \frac{1}{2}(\gamma_A + \gamma_B)$. Here, we introduce $\beta (= \frac{1}{2}\sqrt{\kappa^2 - \Gamma^2})$ to represent the effect of the coupling rate κ and of the difference in the decay rates of the two cavities, given by $\Gamma = \frac{1}{2}(-\gamma_A + \gamma_B)$. It is worth noting that the real part of Eq. (4.13) corresponds to the resonant frequencies, whereas the imaginary part signifies the system loss (i.e., Q).

Figures 4.8(a) and 4.8(b) present the real and imaginary components of the eigenfrequencies stipulated in Eq. (4.13), plotted as functions of Q_c, which is the coupling Q between the two cavities. The plots vary with different Q_B values. Figure 4.8(a) shows that the eigenfrequency (expressed in wavelength) moves beyond the EP as Q_c increases. Here we consider the unique phase bifurcations observed in Fig. 4.7(a), which we calculated using a Q_B value of 5×10^6. The system is linear at the tail of the pulse and resides below the EP because Q_c is at 8×10^6, as indicated by the orange dotted line in Fig. 4.8(a). Owing to the bifurcation of the real part of the eigenfrequency, a phase split becomes observable. As the pulse intensity increases, Q_c, quite intuitively, also effectively grows thanks to the increased decoupling, leading to a collision of the eigenfrequencies. Consequently, their phases merge into a single phase.

In Fig. 4.8(b), we witness substantial modulation of the system Q in proximity to the EP in all instances, a feature that substantially contributes to the efficient SA behaviour. This outcome implies that if we can modulate Q_c, we might be able to adjust the system Q significantly and consequently realize an effective SA.

Figure 4.8(c) shows the system Q as a function of the frequency detuning Δf between cavities A and B (i.e., $\Delta f = f_A - f_B$) while maintaining Q_B at 5×10^6. It shows results for various Q_c values. If Q_c is set at 2×10^7, the system is beyond the EP, which signifies that the two modes diverge into high and low Qs from the outset (as depicted by the green dotted line in Fig. 4.8(b)). Consequently, the system Qs have two values from the beginning, and the modulation remains shallow, even when we alter the refractive index of the cavity. Conversely, if Q_c is too small at $Q_c = 1 \times 10^6$, the starting point is significantly below the EP, as portrayed by the purple dotted line in Fig. 4.8(b). To obtain efficient modulation, we must initialize close to the EP, specifically at $Q_c = 8 \times 10^6$, which is just below the EP. As a result, with minor modulation of the detuning between the cavities, we can obtain significant modulation of the system Q.

While our operation is set just below the EP, it is equally possible to initialize the system just above the EP. However, it is critical to remain close to the EP to ensure effective modulation of the system Q. The resonant shift that we achieve is approximately 1.5 GHz (as shown in Fig. 4.7(c)), leading to a modulation of the system Q from $\sim 1 \times 10^7$ to $\sim 1 \times 10^8$, according to Fig. 4.8(c).

4.2.5 Mode-locking range

Lastly, we undertake a search for the optimal parameters. Figure 4.9(a) presents our findings, visually encapsulated by using a color map depicting the number of peaks in the waveform generated after 70,000 roundtrips. Furthermore, we evaluated the stability of the resulting

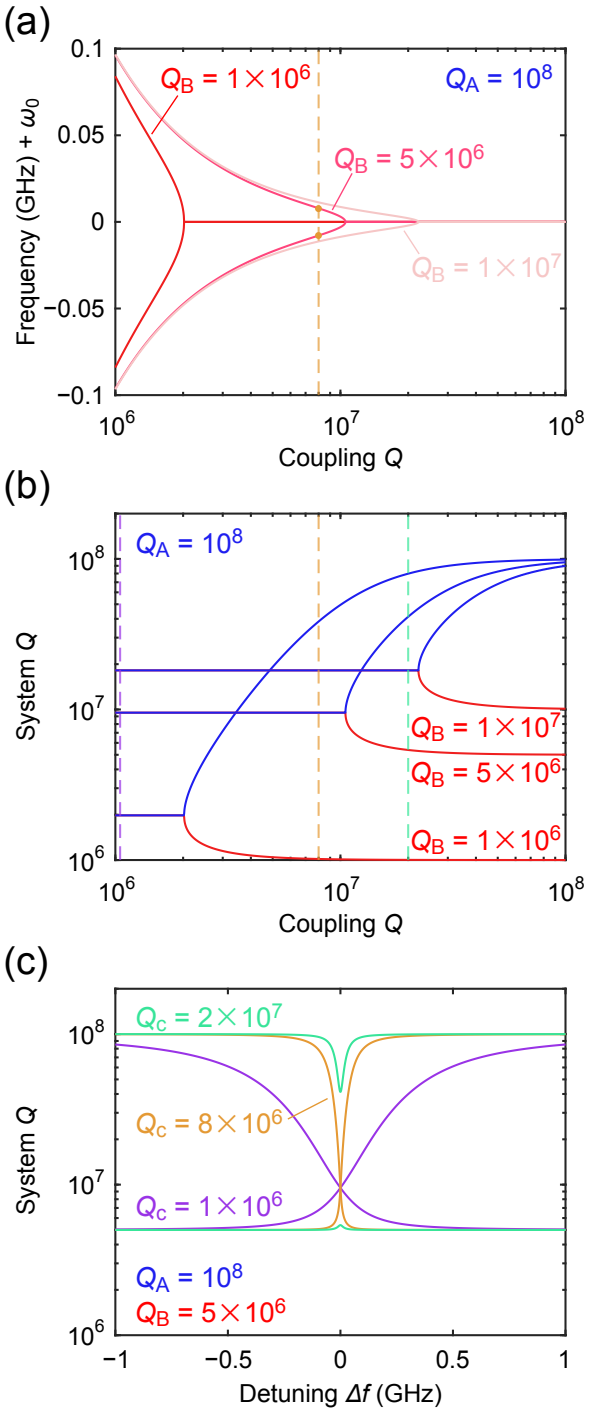

Fig. 4.8 (a) The real part of the eigenfrequency (resonant frequency) depicted as a wavelength shift from the baseline resonance at 1550 nm, for various Q_B values. Q_A is consistently set at 10^8. The orange line represents the condition where $Q_c = 8 \times 10^6$, the parameter set utilized for the computations in Figs. 4.6 and 4.7. (b) Imaginary part of the eigenfrequency (representing gain and loss) displayed as system Q, across different Q_B values. Q_A remains constant at 10^8. (c) System Q plotted against the detuning between Cavity A and Cavity B for a range of Q_c values. Q_A and Q_B are set at 10^8 and 5×10^6, respectively. The condition $Q_c = 8 \times 10^6$ is consistent with the parameters employed in the analyses of Figs. 4.6 and 4.7.

waveform in an attempt to distinguish between stable mode-locking, breather dynamics, and chaotic behaviour. The region of stability is denoted by a white-dotted contour. The white solid line indicates the condition of the EP.

To understand the result, we begin by pointing out that two conditions are needed to achieve mode-locking. The first condition is a high system Q because a low loss is needed to achieve lasing in the first place. It also helps facilitate efficient optical nonlinear effects. The second condition is to achieve efficient SA behaviour, which is essential for mode-locking. We employ Figs. 4.9(b) and 4.9(c) to investigate these two properties.

Figure 4.9(b) is the system Q as a function of Q_{B} when $Q_{\mathrm{A}} = 10^8$ and $Q_{\mathrm{c}} = 8 \times 10^6$. The system Q is high when Q_{B} is high since most of the light exhibits loss through cavity B. But the system Q recovers even when Q_{B} exhibits a reduction in its value due to the presence of the EP. The color-shaded region in the graph represents the value of Q_{A}, indicating that as the system moves away from the EP, the Q-factor approaches its intrinsic value of 1×10^8. Figure 4.9(c) presents the maximum slope value of the system loss rate $\Delta\gamma_\tau$ across varying Q_{B} values. The system Q (Q_{sys}) as a function of the cavity detuning Δf was previously outlined in Fig. 4.8(c). The system loss rate, γ_τ is represented by $\gamma_\tau = \omega_0/Q_{\mathrm{sys}}$, which also varies as a function of detuning Δf. Thus, we define $\Delta\gamma_\tau$ as,

$$\Delta\gamma_\tau = \max\left|\frac{d\gamma_\tau(\Delta f)}{d(\Delta f)}\right|. \tag{4.14}$$

Here, max indicates that we extract the peak value of the function. Computing $\Delta\gamma_\tau$ for different Q_{B} values provides the plot illustrated in Fig. 4.9(c). Intuitively, a larger value of $\Delta\gamma_\tau$ indicates that even small detuning, arising from the Kerr effect, can lead to significant modulation in the system's loss rate. In essence, a substantial $\Delta\gamma_\tau$ is indicative of an efficient artificial SA.

To gain a comprehensive understanding of the results presented in Fig. 4.9(a), let us consider a fixed Q_{c} at 8×10^6. Initiating our discussion at high Q_{B} values, where Q_{B} is $\sim 10^8$, the system Q is at its zenith. However, as suggested by Fig. 4.9(c), the potency of the artificial SA effect is minimal, rendering the system unstable. As Q_{B} falls to roughly 5×10^7, the increase in $\Delta\gamma_\tau$ facilitates mode-locking in the system. The further descent of Q_{B} to around $\sim 10^7$ situates the system on the fringes of stable mode-locking, as depicted in Fig. 4.9(a). Even as $\Delta\gamma_\tau$ increases, the system Q diminishes substantially. It is important to note that Q values degenerate beyond the EP (to the right of the solid white line in Fig. 4.9(a)). This infers that the intensities in cavities A and B are nearly identical, implying that the nonlinear refractive index modulations are virtually equivalent. Consequently, efficient detuning between cavities A and B becomes unattainable, and therefore the recovered Q

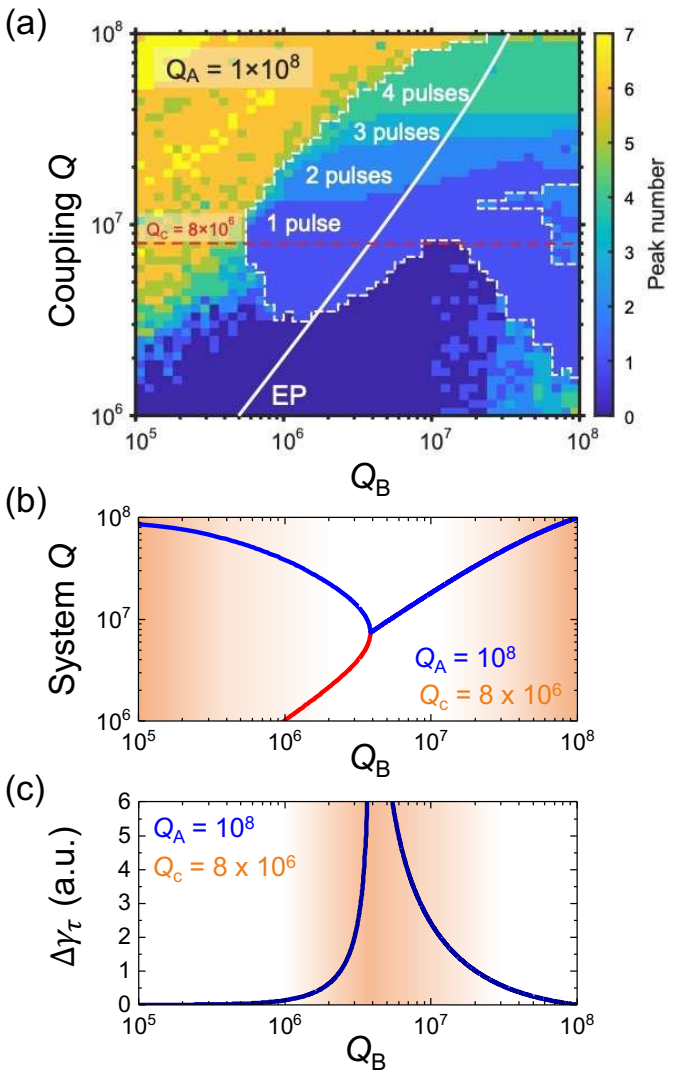

Fig. 4.9 (a) Colour map illustrating the count of peaks in the temporal waveform per roundtrip (indicating the number of pulses per roundtrip) after 70,000 roundtrips as a function of Q_B and Q_c. The region enclosed by a white dotted line represents the stable mode-locked regime. The white solid line signifies the position of the EP. (b) System Q, as calculated from Eq. (9), plotted as a function of Q_B when Q_A and Q_c are 10^8 and 8×10^6, respectively. The system Q decreases as Q_B reduces, but it recovers due to the presence of the EP. A high Q is essential to obtain sufficient net gain and optical nonlinearity in cavity A, which are required for lasing and mode-locking. (c) $\Delta\gamma_\tau$ plotted as a function of Q_B when Q_A and Q_c are 10^8 and 8×10^6, respectively. $\Delta\gamma_\tau$ reaches its maximum value of ~ 34.2 in an EP condition. The definition of $\Delta\gamma_\tau$ is provided in the main text. A higher value corresponds to substantial modulation of the system loss rate given a specific refractive index modulation. This property is necessary for achieving efficient artificial SA.

hinders the stable mode-locked operation (i.e., breathing behaviour). Yet, as Q_B nears the EP, $\Delta\gamma_\tau$ experiences a notable surge, peaking at approximately 34.2 at the EP. Owing to the pinnacle slope that occurs at $\Delta f = 0$, significant artificial SA arises close to EP, facilitating mode-locking even with diminished system Q values.

A region warranting particular attention lies to the left of the EP condition ($Q_B < 4 \times 10^6$). Here, while $\Delta\gamma_\tau$ undergoes a decline, the system Q exhibits a considerable resurgence, facilitating mode-locking courtesy of the pronounced Kerr effect. In contrast to the region to the right of the EP, the system Q between modes A and B shows a marked disparity that augments efficient system decoupling. This stability in mode-locking persists until Q_B falls to 6×10^5. Beyond this, the diminished $\Delta\gamma_\tau$ restricts the attainment of mode-locking (for $Q_B < 6 \times 10^5$).

The insights gleaned from Figs. 4.9(b) and 4.9(c) shed light on the restoration of mode-locking as Q_B decreases, a process that can be attributed to the unique behaviour of the EP in a coupled cavity system. This demonstrates the role of the EP as an enabler of mode-locking even under low-Q_B conditions, revealing novel avenues for the manipulation and control of lasing dynamics. Significantly, the optimal region for mode-locking is relatively broad, thus offering promising prospects for experimental implementation.

4.2.6 Conclusion

In conclusion, this study provides a comprehensive examination of a novel mode-locking strategy that forgoes the utilization of natural SAs, instead leveraging the Kerr effect and a coupled microresonator system in close proximity to an EP. The results reveal the occurrence of mode-locking after approximately 7×10^4 round trips. The formed pulse adopts a sech^2 shape, with its Fourier transform-limited phase. The resonant shift associated with the light intensity modulation underscores the role of instantaneous decoupling as an artificial SA, contributing to efficient mode-locking. Our exploration of the parameter space further clarifies the conditions under which mode-locking is achieved. Notably, mode-locking consistently occurs close to the EP, where substantial modulation of the system Q is possible.

Our research opens new avenues for exploring coupled microresonator systems as platforms for efficient mode-locking, moving beyond the traditional use of saturable absorbers. Our investigations identified the broad sweet spot for achieving mode-locking, which offers exciting possibilities for the experimental validation and application of this technique.

Our calculations indicate that in the coupled-resonator system, each resonator can achieve the required mode-locking parameters using fabrication processes that are already well-established. Moreover, the principle has been validated experimentally using fiber ring resonators [157], indicating that this method is viable.

Finally, calculations were performed for different resonator diameters, assuming actual experiments, which is considered a fabrication error. Figure 4.10 shows the colormap of the mode-locking region as a function of the diameter difference ΔD between the two resonators. The color represents the ratio of pulse peak power P_{peak} to average power P_{average}. The results reveal that stable pulses are achieved when the diameter difference is within 30 nm. To ensure that the diameters of the two resonators remain within 30 nm of each other, assuming that the fabrication errors follow a normal distribution, we calculated that approximately 600 samples are needed. With 600 samples, there is a 90% probability of matching this condition, which we consider to be a practical target. Therefore, when we fabricate a pair of toroids with a diameter difference within this tolerance, we can demonstrate the proof of principle for our coupled-resonator model.

Recent interest in Er^{3+}-ion doping in Si_3N_4 waveguide [90, 91] suggests it to be a viable alternative, attracting increasing attention and enabling tighter diameter control, which makes them an appealing candidate for passive mode-locking in a coupled-resonator system.

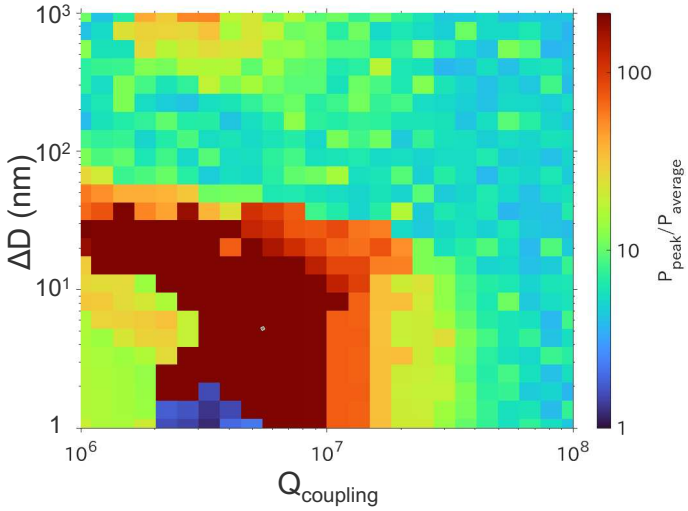

Fig. 4.10 Color map illustrating the power ratio of the peak power to the average power of the generated pulse. When the diameter difference ΔD increases, mode-locking cannot be achieved.

Chapter 5

Summary and outlook

This chapter summarizes the work in this thesis and provides an outlook for future research on passive mode-locking in integrated microresonator systems.

5.1 Summary

In Chapters 1 and 2, this thesis provides the background and fundamental principles underlying mode-locked lasers and microresonators. Building upon these foundations, Chapter 3 describes the fabrication process for high-Q microresonators, and Chapter 4 explains how the microresonator systems are designed for integrated passive mode-locked lasers.

Chapter 1 introduced the background on mode-locked lasers and explained the motivation behind this thesis. It covered the types and mechanisms of conventional mode-locked lasers, various mode-locking platforms, and related research, and finally, it outlined the thesis objectives.

Chapter 2 presents the theoretical, simulated, and experimental characteristics of microresonators. It also introduces the fundamentals of microresonator-based frequency combs (microcombs) and soliton microcombs, drawing on the Lugiato–Lefever equation to explain their underlying physics. Finally, the chapter discusses advances in soliton microcomb generation, focusing on experimental methods to reliably access the soliton existence range. The insights from this chapter are crucial for understanding how passive mode-locking and soliton formation can be realized using high-Q microresonators.

Chapter 3 describes the fabrication process and performance evaluation of ultra-high-Q silicon dioxide microresonators. The author fabricated silica microtoroids from thermally oxidized silicon wafers using photolithography and two types of etching processes. By refining each step and improving the surface quality of the resonator's waveguide region, the Q-factor was successfully enhanced, leading to the realization of toroidal resonators

with Q-factors exceeding 500 million. Specific attention is given to methods for doping erbium ions as the gain medium with the sol-gel method and incorporating carbon nanotubes or graphene as nonlinear loss materials. The chapter concludes by emphasizing that these fabrication techniques, combined with the sol-gel ion-doping and SA deposition methods, form the foundation for realizing integrated passive mode-locked lasers capable of generating ultrashort pulses.

Chapter 4 presents the design of integrated mode-locked lasers based on numerical analysis. Two approaches are discussed: single-resonator models and coupled-resonator models. In the single-resonator model, passive mode-locking is achieved by integrating a saturable absorber within an Er^{3+}-doped microresonator with Q higher than 10^8. The numerical simulations investigate the effect of system parameters, such as resonator Q and gain, on the generation of stable mode-locked pulses. Results demonstrate that achieving high-Q factors is crucial to support sufficient nonlinear optical effects necessary for stable mode-locking. Meanwhile, the coupled-resonator model offers an alternative approach to passive mode-locking without using any saturable absorber. The analysis reveals that coupling two microresonators creates a non-Hermitian system with an exceptional point (EP), a critical point where system eigenmodes coalesce. By tuning the coupling strength, the system exhibits strong modulation of its Q-factor, enabling saturable absorption-like behavior without physical absorbers. Numerical simulations show that the system can maintain stable mode-locking even under low-Q conditions in the secondary resonator, thereby broadening the operational range for passive mode-locking techniques. The chapter highlights that the non-Hermitian physics of coupled microresonators offers a novel and efficient route for achieving passive mode-locking, potentially surpassing conventional methods relying on saturable absorbers. This study lays the design guideline for experimental implementations of integrated mode-locked lasers based on microresonator systems.

5.2 Outlook

It is widely recognized that mode-locked lasers form a fundamental technology for industrial applications, serving as a core platform in areas such as ultrafast optics, precision metrology, and high-speed communication. Among these lasers, microresonator-based implementations offer a compelling balance between cost-effectiveness and high performance, making them highly promising for real-world deployment. In this work, we have developed the key design concepts and component technologies required to realize passive mode-locking within microresonators. As described in Chapter 4, passive mode-locking can, in principle, be

achieved in both single-resonator and coupled-resonator systems; however, each approach still faces practical challenges.

In the single-resonator system, the primary obstacle is achieving a sufficiently high Q-factor. For instance, attaching carbon nanotubes (CNTs) to an erbium-doped microresonator could provide the necessary conditions for stable mode-locking if the Q-factor on the order of 10^8 were reached. However, the presence of polydimethylsiloxane (PDMS) in the fabrication process results in significant absorption, thus preventing further increases in the Q-factor. Graphene represents a promising alternative saturable absorber material: by employing mechanical exfoliation and transfer methods, the resonator can be coated without introducing PDMS-based losses. Another possibility is to increase the erbium doping concentration to enhance the gain; however, doping beyond current levels leads to ion clustering and, consequently, higher loss, negating the benefit of increased gain.

Our calculations indicate that in the coupled-resonator system, each resonator can achieve the required mode-locking parameters using fabrication processes that are already well-established. Moreover, the principle has been validated experimentally using fiber ring resonators [157], indicating that this method is viable. This previous study draws inspiration from our mechanism [103] and employs a fiber ring system, in which matching the cavity lengths of the two resonators is relatively straightforward. If implemented using microresonator systems, this approach could enable repetition rates exceeding the GHz range and the generation of shorter pulses. In practice, coupling two resonators requires that their diameters match within about 30 nm, as shown in Fig. 4.10. Therefore, when we fabricate a pair of toroids with a diameter difference within this tolerance, we can demonstrate the proof of principle for our coupled-resonator model. A further alternative lies in erbium-doped Si_3N_4 ring resonators [90, 91], which have attracted increasing attention and enable tighter diameter control, making them a promising candidate for passive mode-locking with a coupled-resonator system.

Looking toward the future, our research identifies several promising opportunities. One significant avenue is expanding the wavelength coverage by employing different gain media, which would broaden the operating range of the microresonator platform and enable its use across various optical bands for diverse applications. Additionally, further advancements in fabrication techniques inspired by our process development can lead to the passive generation of Stokes solitons and the deterministic formation of soliton crystals [158] by integrating saturable absorbers with microresonators. Moreover, exploring nonlinear interactions between two-dimensional materials [93], such as graphene [76] and microresonators, offers valuable insights into novel light-matter interactions. These developments hold substantial potential for practical applications in photonics, including compact sensing devices such as LiDAR,

spectroscopy, and optical coherence tomography (OCT). Furthermore, microresonator-based frequency combs can facilitate high-speed optical communications, while their stable ultrashort pulses can serve as seed sources for laser processing in industrial applications.

In conclusion, continued advancements in microresonator fabrication, gain medium integration, and saturable absorber deposition will pave the way toward highly efficient, cost-effective mode-locked lasers for industrial applications. The current research highlights both the potential of single- and coupled-resonator systems for passive mode-locking and the challenges that remain in realizing these approaches. By resolving the challenges associated with Q-factor enhancement, doping concentration, and resonator diameter matching, future devices can unlock high-repetition-rate, short-pulse performance suitable for a wide range of technological demands.

References

[1] P. G. Kryukov, "Ultrashort-pulse lasers," Quantum Electronics **31**, 95 (2001).

[2] U. Keller, K. D. Li, B. T. Khuri-Yakub, D. M. Bloom, K. J. Weingarten, and D. C. Gerstenberger, "High-frequency acousto-optic mode locker for picosecond pulse generation," Optics Letters **15**, 45–47 (1990).

[3] U. Keller, "Recent developments in compact ultrafast lasers," Nature **424**, 831–838 (2003).

[4] S. Kimura, S. Tani, and Y. Kobayashi, "Kerr-lens mode locking above a 20 GHz repetition rate," Optica **6**, 532 (2019).

[5] M. Mangold, C. A. Zaugg, S. M. Link, M. Golling, B. W. Tilma, and U. Keller, "Pulse repetition rate scaling from 5 to 100 GHz with a high-power semiconductor disk laser," Optics Express **22**, 6099–6107 (2014).

[6] C. G. E. Alfieri, D. Waldburger, J. Nürnberg, M. Golling, and U. Keller, "Sub-150-fs pulses from an optically pumped broadband modelocked integrated external-cavity surface emitting laser," Optics Letters **44**, 25–28 (2019).

[7] G. Chang and Z. Wei, "Ultrafast fiber lasers: An expanding versatile toolbox," iScience **23**, 101101 (2020).

[8] M. E. Fermann, "Passive mode locking by using nonlinear polarization evolution in a polarization-maintaining erbium-doped fiber," Optics Letters **18**, 894 (1993).

[9] M. E. Fermann, F. Haberl, M. Hofer, and H. Hochreiter, "Nonlinear amplifying loop mirror," Optics Letters **15**, 752–754 (1990).

[10] N. Kuse, J. Jiang, C.-C. Lee, T. R. Schibli, and M. E. Fermann, "All polarization-maintaining Er fiber-based optical frequency combs with nonlinear amplifying loop mirror," Optics Express **24**, 3095–3102 (2016).

[11] W. Hänsel, H. Hoogland, M. Giunta, S. Schmid, T. Steinmetz, R. Doubek, P. Mayer, S. Dobner, C. Cleff, M. Fischer, and R. Holzwarth, "All polarization-maintaining fiber laser architecture for robust femtosecond pulse generation," Applied Physics. B, Lasers and Optics **123** (2017).

[12] K. J. Vahala, "Optical microcavities," Nature **424**, 839 (2003).

[13] T. J. Kippenberg, R. Holzwarth, and S. A. Diddams, "Microresonator-based optical frequency combs," Science **332**, 555–559 (2011).

[14] P. Del'Haye, A. Schliesser, O. Arcizet, T. Wilken, R. Holzwarth, and T. J. Kippenberg, "Optical frequency comb generation from a monolithic microresonator," Nature **450**, 1214 (2007).

[15] T. Herr, V. Brasch, J. D. Jost, C. Y. Wang, N. M. Kondratiev, M. L. Gorodetsky, and T. J. Kippenberg, "Temporal solitons in optical microresonators," Nature Photonics **8**, 145–152 (2014).

[16] F. Leo, S. Coen, P. Kockaert, S.-P. Gorza, P. Emplit, and M. Haelterman, "Temporal cavity solitons in one-dimensional kerr media as bits in an all-optical buffer," Nature Photonics **4**, 471–476 (2010).

[17] H. Lee, T. Chen, J. Li, K. Y. Yang, S. Jeon, O. Painter, and K. J. Vahala, "Chemically etched ultrahigh-Q wedge-resonator on a silicon chip," Nature Photonics **6**, 369–373 (2012).

[18] D. Pudo, H. Byun, J. Chen, J. Sickler, F. X. Kärtner, and E. P. Ippen, "Scaling of passively mode-locked soliton erbium waveguide lasers based on slow saturable absorbers," Optics Express **16**, 19221–19231 (2008).

[19] H. Byun, D. Pudo, S. Frolov, A. Hanjani, J. Shmulovich, E. P. Ippen, and F. X. Kärtner, "Integrated 2 GHz femtosecond laser based on a planar Er-doped lightwave circuit," in "CLEO/QELS: 2010 Laser Science to Photonic Applications," (2010), pp. 1–2.

[20] N. Singh, E. Ippen, and F. X. Kärtner, "Towards CW modelocked laser on chip– a large mode area and NLI for stretched pulse mode locking," Optics Express **28**, 22562–22579 (2020).

[21] A. Martinez and S. Yamashita, "Multi-gigahertz repetition rate passively modelocked fiber lasers using carbon nanotubes," Optics Express **19**, 6155–6163 (2011).

[22] L. Yang, D. K. Armani, and K. J. Vahala, "Fiber-coupled erbium microlasers on a chip," Applied Physics Letters **83**, 825–826 (2003).

[23] K. Totsuka and M. Tomita, "Optical microsphere amplification system," Optics Letters **32**, 3197–3199 (2007).

[24] X. Wang, Y. Yu, S. Wang, J. M. Ward, S. N. Chormaic, and P. Wang, "Single mode green lasing and multicolor luminescent emission from an Er^{3+}-Yb^{3+} co-doped compound fluorosilicate glass microsphere resonator," OSA Continuum **1**, 261–273 (2018).

[25] T. Tan, H.-J. Chen, Z. Yuan, Y. Yu, Q.-T. Cao, N. An, Q. Gong, C. W. Wong, Y. Rao, Y.-F. Xiao, and B. Yao, "Gain-assisted chiral soliton microcombs," arXiv [physics.optics] (2020).

[26] W. Wang, L. Wang, and W. Zhang, "Advances in soliton microcomb generation," Advanced Photonics (2020).

[27] X.-F. Liu, F. Lei, T.-J. Wang, G.-L. Long, and C. Wang, "Gain lifetime characterization through time-resolved stimulated emission in a whispering-gallery mode microresonator," Nanophotonics **8**, 127–134 (2018).

[28] Y. Hu, Y. Bai, Y. Liu, S. Ding, S. Hua, X. Jiang, and M. Xiao, "Absorption and gain saturable nonlinearities in erbium-doped optical microcavities," Physical Review. A **100**, 033831 (2019).

[29] B. Peng, Ş. K. Özdemir, M. Liertzer, W. Chen, J. Kramer, H. Yılmaz, J. Wiersig, S. Rotter, and L. Yang, "Chiral modes and directional lasing at exceptional points," Proceedings of the National Academy of Sciences of the United States of America **113**, 6845–6850 (2016).

[30] U. Fano, "Effects of configuration interaction on intensities and phase shifts," Physics Review **124**, 1866–1878 (1961).

[31] F. Lei, B. Peng, Ş. K. Özdemir, G. L. Long, and L. Yang, "Dynamic fano-like resonances in erbium-doped whispering-gallery-mode microresonators," Applied Physics Letters **105**, 101112 (2014).

[32] X.-F. Liu, T.-J. Wang, and C. Wang, "Optothermal control of gains in erbium-doped whispering-gallery microresonators," Optics Letters **43**, 326–329 (2018).

[33] B. Shen, L. Chang, J. Liu, H. Wang, Q.-F. Yang, C. Xiang, R. N. Wang, J. He, T. Liu, W. Xie, J. Guo, D. Kinghorn, L. Wu, Q.-X. Ji, T. J. Kippenberg, K. Vahala, and J. E. Bowers, "Integrated turnkey soliton microcombs," Nature **582**, 365–369 (2020).

[34] A. E. Ulanov, T. Wildi, N. G. Pavlov, J. D. Jost, M. Karpov, and T. Herr, "Synthetic reflection self-injection-locked microcombs," Nature Photonics **18**, 294–299 (2024).

[35] N. Kondratiev, A. Gorodnitskiy, and V. Lobanov, "Influence of the microresonator nonlinearity on the self-injection locking effect," EPJ Web of Conferences **220**, 02006 (2019).

[36] Y. Ooka, T. Tetsumoto, A. Fushimi, W. Yoshiki, and T. Tanabe, "CMOS compatible high-Q photonic crystal nanocavity fabricated with photolithography on silicon photonic platform," Scientific Reports **5**, 11312 (2015).

[37] M. A. Butt, S. N. Khonina, and N. L. Kazanskiy, "Recent advances in photonic crystal optical devices: A review," Optics and Laser Technology **142**, 107265 (2021).

[38] L. R. O. M. F.r.s., "CXII. the problem of the whispering gallery," The London, Edinburgh, and Dublin Philosophical Magazine and Journal of Science **20**, 1001–1004 (1910).

[39] T. Tanabe, S. Fujii, and R. Suzuki, "Review on microresonator frequency combs," Japanese Journal of Applied Physics **58**, SJ0801 (2019).

[40] G. P. Agrawal, *Nonlinear Fiber Optics: Formerly Quantum Electronics* (Academic Press, 2013).

[41] S. Fujii and T. Tanabe, "Dispersion engineering and measurement of whispering gallery mode microresonator for kerr frequency comb generation," Nanophotonics **9**, 1087–1104 (2020).

[42] T. Carmon, L. Yang, and K. Vahala, "Dynamical thermal behavior and thermal self-stability of microcavities," Optics Express **12**, 4742–4750 (2004).

[43] L. He, Y.-F. Xiao, J. Zhu, S. K. Ozdemir, and L. Yang, "Oscillatory thermal dynamics in high-Q PDMS-coated silica toroidal microresonators," Optics Express **17**, 9571–9581 (2009).

[44] T. J. Kippenberg, S. M. Spillane, and K. J. Vahala, "Kerr-nonlinearity optical parametric oscillation in an ultrahigh-Q toroid microcavity," Physical Review Letters **93**, 083904 (2004).

[45] L. Yang, T. Carmon, B. Min, S. M. Spillane, and K. J. Vahala, "Erbium-doped and raman microlasers on a silicon chip fabricated by the sol–gel process," Applied Physics Letters **86**, 091114 (2005).

[46] H. Choi and A. M. Armani, "Raman–Kerr frequency combs in zr-doped silica hybrid microresonators," Optics Letters **43**, 2949–2952 (2018).

[47] C.-H. Dong, Z. Shen, C.-L. Zou, Y.-L. Zhang, W. Fu, and G.-C. Guo, "Brillouin-scattering-induced transparency and non-reciprocal light storage," Nature Communications **6**, 6193 (2015).

[48] Y. Bai, M. Zhang, Q. Shi, S. Ding, Y. Qin, Z. Xie, X. Jiang, and M. Xiao, "Brillouin-Kerr soliton frequency combs in an optical microresonator," Physical Review Letters **126**, 063901 (2021).

[49] M. Zhang, S. Ding, X. Li, K. Pu, S. Lei, M. Xiao, and X. Jiang, "Strong interactions between solitons and background light in Brillouin-Kerr microcombs," Nature Communications **15**, 1661 (2024).

[50] H. A. Haus and W. Huang, "Coupled-mode theory," Proceedings of the IEEE **79**, 1505–1518 (1991).

[51] T. Herr, K. Hartinger, J. Riemensberger, C. Y. Wang, E. Gavartin, R. Holzwarth, M. L. Gorodetsky, and T. J. Kippenberg, "Universal formation dynamics and noise of kerr-frequency combs in microresonators," Nature Photonics **6**, 480–487 (2012).

[52] P. Del'Haye, A. Coillet, W. Loh, K. Beha, S. B. Papp, and S. A. Diddams, "Phase steps and resonator detuning measurements in microresonator frequency combs," Nature Communications **6**, 5668 (2015).

[53] X. Xue, Y. Xuan, P.-H. Wang, Y. Liu, D. E. Leaird, M. Qi, and A. M. Weiner, "Normal-dispersion microcombs enabled by controllable mode interactions," Laser and Photonics Reviews **9**, L23–L28 (2015).

[54] X. Xue, M. Qi, and A. M. Weiner, "Normal-dispersion microresonator kerr frequency combs," Nanophotonics **5**, 244–262 (2016).

[55] S. Zhang, T. Bi, G. N. Ghalanos, N. P. Moroney, L. Del Bino, and P. Del'Haye, "Dark-bright soliton bound states in a microresonator," Physical Review Letters **128**, 033901 (2022).

[56] A. A. Savchenkov, V. S. Ilchenko, A. B. Matsko, and L. Maleki, "Kilohertz optical resonances in dielectric crystal cavities," Physical Review. A **70**, 051804 (2004).

[57] Y. K. Chembo, "Kerr optical frequency combs: theory, applications and perspectives," Nanophotonics **5**, 214–230 (2016).

[58] Y. K. Chembo and C. R. Menyuk, "Spatiotemporal Lugiato-Lefever formalism for kerr-comb generation in whispering-gallery-mode resonators," Physical Review. A **87** (2013).

[59] S. Coen, H. G. Randle, T. Sylvestre, and M. Erkintalo, "Modeling of octave-spanning kerr frequency combs using a generalized mean-field Lugiato-Lefever model," Optics Letters **38**, 37–39 (2013).

[60] Q. Li, T. C. Briles, D. A. Westly, T. E. Drake, J. R. Stone, B. R. Ilic, S. A. Diddams, S. B. Papp, and K. Srinivasan, "Stably accessing octave-spanning microresonator frequency combs in the soliton regime," Optica **4**, 193–203 (2017).

[61] Z. Gong, A. Bruch, M. Shen, X. Guo, H. Jung, L. Fan, X. Liu, L. Zhang, J. Wang, J. Li, J. Yan, and H. X. Tang, "High-fidelity cavity soliton generation in crystalline AlN micro-ring resonators," Optics Letters **43**, 4366–4369 (2018).

[62] V. Brasch, M. Geiselmann, M. H. P. Pfeiffer, and T. J. Kippenberg, "Bringing short-lived dissipative Kerr soliton states in microresonators into a steady state," Optics Express **24**, 29312–29320 (2016).

[63] X. Yi, Q.-F. Yang, K. Youl Yang, and K. Vahala, "Active capture and stabilization of temporal solitons in microresonators," Optics Letters **41**, 2037–2040 (2016).

[64] M.-G. Suh, Q.-F. Yang, K. Y. Yang, X. Yi, and K. J. Vahala, "Microresonator soliton dual-comb spectroscopy," Science **354**, 600–603 (2016).

[65] M.-G. Suh and K. J. Vahala, "Soliton microcomb range measurement," Science **359**, 884–887 (2018).

[66] J. R. Stone, T. C. Briles, T. E. Drake, D. T. Spencer, D. R. Carlson, S. A. Diddams, and S. B. Papp, "Thermal and nonlinear dissipative-soliton dynamics in Kerr-microresonator frequency combs," Physical Review Letters **121**, 063902 (2018).

[67] S. Zhang, J. M. Silver, L. Del Bino, F. Copie, M. T. M. Woodley, G. N. Ghalanos, A. O. Svela, N. Moroney, and P. Del'Haye, "Sub-milliwatt-level microresonator solitons with extended access range using an auxiliary laser," Optica **6**, 206 (2019).

[68] H. Zhou, Y. Geng, W. Cui, S.-W. Huang, Q. Zhou, K. Qiu, and C. Wei Wong, "Soliton bursts and deterministic dissipative Kerr soliton generation in auxiliary-assisted microcavities," Light, Science and Applications **8**, 50 (2019).

[69] R. Niu, S. Wan, Z.-Y. Wang, J. Li, W.-Q. Wang, W.-F. Zhang, G.-C. Guo, C.-L. Zou, and C.-H. Dong, "Perfect soliton crystals in the high-Q microrod resonator," IEEE Photonics Technology Letters **33**, 788–791 (2021).

[70] R. D. Richtmyer, "Dielectric resonators," Journal of Applied Physics **10**, 391–398 (1939).

[71] Z. Chen, X. Tu, M. Dai, Q. Li, and H. Y. Fu, "Kerr frequency comb generation in microsphere resonators with normal dispersion," Journal of Lightwave Technology **40**, 1092–1097 (2022).

[72] S. M. Spillane, T. J. Kippenberg, O. J. Painter, and K. J. Vahala, "Ideality in a fiber-taper-coupled microresonator system for application to cavity quantum electrodynamics," Physical Review Letters **91**, 043902 (2003).

[73] L. Yang and K. J. Vahala, "Gain functionalization of silica microresonators," Optics Letters **28**, 592–594 (2003).

[74] A. V. Andrianov and E. A. Anashkina, "Tunable Raman lasing in an As_2S_3 chalcogenide glass microsphere," Optics Express **29**, 5580–5587 (2021).

[75] J. Yu, Y. Du, X. Zhao, S. Jia, Z. Li, S. Wang, and P. Wang, "2 μm lasing from Tm^{3+}-doped PbO-PbF_2-Bi_2O_3-Ga_2O_3 glass microspheres," Optics Letters **46**, 5084–5087 (2021).

[76] T. Tan, Z. Yuan, H. Zhang, G. Yan, S. Zhou, N. An, B. Peng, G. Soavi, Y. Rao, and B. Yao, "Multispecies and individual gas molecule detection using stokes solitons in a graphene over-modal microresonator," Nature Communications **12**, 6716 (2021).

[77] Z. Chen, X. Tu, J. Zhao, and H. Y. Fu, "An erbium-doped fiber whispering-gallery-mode microcavity laser," IEEE Photonics Technology Letters **31**, 1650–1653 (2019).

[78] D. K. Armani, T. J. Kippenberg, S. M. Spillane, and K. J. Vahala, "Ultra-high-Q toroid microcavity on a chip," Nature **421**, 925–928 (2003).

[79] G. Lin, R. Henriet, A. Coillet, M. Jacquot, L. Furfaro, G. Cibiel, L. Larger, and Y. K. Chembo, "Dependence of quality factor on surface roughness in crystalline whispering-gallery mode resonators," Optics Letters **43**, 495–498 (2018).

[80] S. Honari, S. Haque, and T. Lu, "Fabrication of ultra-high Q silica microdisk using chemo-mechanical polishing," Applied Physics Letters **119**, 031107 (2021).

[81] H. F. Winters and J. W. Coburn, "The etching of silicon with XeF_2 vapor," Applied Physics Letters **34**, 70–73 (1979).

[82] K. Sugano and O. Tabata, "Reduction in surface roughness and aperture size effect for xef_2 etching of Si," in "Micromachining and Microfabrication Process Technology VIII," (SPIE, 2003).

[83] T. Kumagai, N. Hirota, K. Sato, K. Namiki, H. Maki, and T. Tanabe, "Saturable absorption by carbon nanotubes on silica microtoroids," Journal of Applied Physics **123**, 233104 (2018).

[84] A. Martinez, M. Al Araimi, A. Dmitriev, P. Lutsyk, S. Li, C. Mou, A. Rozhin, M. Sumetsky, and S. Turitsyn, "Low-loss saturable absorbers based on tapered fibers embedded in carbon nanotube/polymer composites," APL photonics **2**, 126103 (2017).

[85] J. H. Kim, J.-Y. Hwang, H. R. Hwang, H. S. Kim, J. H. Lee, J.-W. Seo, U. S. Shin, and S.-H. Lee, "Simple and cost-effective method of highly conductive and elastic carbon nanotube/polydimethylsiloxane composite for wearable electronics," Scientific Reports **8**, 1375 (2018).

[86] A. Polman, "Erbium implanted thin film photonic materials," Journal of Applied Physics **82**, 1–39 (1997).

[87] J. D. B. Bradley and M. Pollnau, "Erbium-doped integrated waveguide amplifiers and lasers," Laser and Photonics Reviews **5**, 368–403 (2011).

[88] J. Mu, M. Dijkstra, J. Korterik, H. Offerhaus, and S. M. García-Blanco, "High-gain waveguide amplifiers in Si_3N_4 technology via double-layer monolithic integration," Photonics Research **8**, 1634 (2020).

[89] M. Xin, N. Li, N. Singh, A. Ruocco, Z. Su, E. S. Magden, J. Notaros, D. Vermeulen, E. P. Ippen, M. R. Watts, and F. X. Kärtner, "Optical frequency synthesizer with an integrated erbium tunable laser," Light, Science and Applications **8**, 122 (2019).

[90] Y. Liu, Z. Qiu, X. Ji, A. Lukashchuk, J. He, J. Riemensberger, M. Hafermann, R. N. Wang, J. Liu, C. Ronning, and T. J. Kippenberg, "A photonic integrated circuit-based erbium-doped amplifier," Science **376**, 1309–1313 (2022).

[91] Y. Liu, Z. Qiu, X. Ji, A. Bancora, G. Lihachev, J. Riemensberger, R. N. Wang, A. Voloshin, and T. J. Kippenberg, "A fully hybrid integrated erbium-based laser," Nature Photonics **18**, 829–835 (2024).

[92] T. S. Prugger Suzuki, A. Nakashima, K. Nagashima, R. Ishida, R. Imamura, S. Fujii, S. Y. Set, S. Yamashita, and T. Tanabe, "Design of a passively mode-locking whispering-gallery-mode microlaser," Journal of the Optical Society of America B **38**, 3172–3178 (2021).

[93] S. Fujii, N. Fang, D. Yamashita, D. Kozawa, C. F. Fong, and Y. K. Kato, "Van der waals decoration of ultra-high-Q silica microcavities for $\chi^{(2)}$–$\chi^{(3)}$ hybrid nonlinear photonics," Nano Letters **24**, 4209–4216 (2024).

[94] C. Wang, Z. Fu, W. Mao, J. Qie, A. D. Stone, and L. Yang, "Non-hermitian optics and photonics: from classical to quantum," Advances in Optics and Photonics **15**, 442 (2023).

[95] W. Chen, D. Leykam, Y. D. Chong, and L. Yang, "Nonreciprocity in synthetic photonic materials with nonlinearity," MRS bulletin **43**, 443–451 (2018).

[96] M. Zhang, W. Sweeney, C. W. Hsu, L. Yang, A. D. Stone, and L. Jiang, "Quantum noise theory of exceptional point amplifying sensors," Physical Review Letters **123** (2019).

[97] C. Wang, W. R. Sweeney, A. D. Stone, and L. Yang, "Coherent perfect absorption at an exceptional point," Science (New York, N.Y.) **373**, 1261–1265 (2021).

[98] J. Zhang, B. Peng, Ş. K. Özdemir, K. Pichler, D. O. Krimer, G. Zhao, F. Nori, Y.-X. Liu, S. Rotter, and L. Yang, "A phonon laser operating at an exceptional point," Nature Photonics **12**, 479–484 (2018).

[99] W. Chen, Ş. Kaya Özdemir, G. Zhao, J. Wiersig, and L. Yang, "Exceptional points enhance sensing in an optical microcavity," Nature **548**, 192–196 (2017).

[100] Y. Huang, Y. Shen, C. Min, S. Fan, and G. Veronis, "Unidirectional reflectionless light propagation at exceptional points," Nanophotonics **6**, 977–996 (2017).

[101] B. Peng, S. K. Özdemir, S. Rotter, H. Yilmaz, M. Liertzer, F. Monifi, C. M. Bender, F. Nori, and L. Yang, "Loss-induced suppression and revival of lasing," Science **346**, 328–332 (2014).

[102] B. Peng, Ş. K. Özdemir, F. Lei, F. Monifi, M. Gianfreda, G. L. Long, S. Fan, F. Nori, C. M. Bender, and L. Yang, "Parity–time-symmetric whispering-gallery microcavities," Nature Physics **10**, 394–398 (2014).

[103] R. Imamura, S. Fujii, A. Nakashima, and T. Tanabe, "Exceptional point proximity-driven mode-locking in coupled microresonators," Optics Express **32**, 22280 (2024).

[104] B. Min, T. J. Kippenberg, L. Yang, K. J. Vahala, J. Kalkman, and A. Polman, "Erbium-implanted high-Q silica toroidal microcavity laser on a silicon chip," Physical Review. A **70**, 033803 (2004).

[105] X. Orignac, D. Barbier, X. Min Du, R. M. Almeida, O. McCarthy, and E. Yeatman, "Sol–gel silica/titania-on-silicon Er/Yb-doped waveguides for optical amplification at 1.5 μm," Optical Materials **12**, 1–18 (1999).

[106] X. Zhang and A. M. Armani, "Silica microtoroid resonator sensor with monolithically integrated waveguides," Optics Express **21**, 23592–23603 (2013).

[107] S. Liu, R. Lv, Y. Wang, J. Wang, Y. Wang, and H. Wang, "Passively mode-locked fiber laser with WS_2/SiO_2 saturable absorber fabricated by sol-gel technique," ACS Applied Materials and Interfaces **12**, 29625–29630 (2020).

[108] W. Huang, R. R. A. Syms, E. M. Yeatman, M. M. Ahmad, T. V. Clapp, and S. M. Ojha, "Fiber-device-fiber gain from a sol-gel erbium-doped waveguide amplifier," IEEE photonics technology Letters: a publication of the IEEE Laser and Electro-optics Society **14**, 959–961 (2002).

[109] Y. Djaoued, V. H. Phong, S. Badilescu, P. V. Ashrit, F. E. Girouard, and V.-V. Truong, "Sol-gel-prepared ITO films for electrochromic systems," Thin Solid Films **293**, 108–112 (1997).

[110] M. Yamane, S. Aso, S. Okano, and T. Sakaino, "Low temperature synthesis of a monolithic silica glass by the pyrolysis of a silica gel," Journal of Materials Science **14**, 607–611 (1979).

[111] F. A. Sigoli, R. R. Gonçalves, Y. Messaddeq, and S. J. L. Ribeiro, "Erbium- and ytterbium-doped sol–gel SiO2–HfO2 crack-free thick films onto silica on silicon substrate," Journal of Non-Crystalline Solids **352**, 3463–3468 (2006).

[112] L.-L. Yang, Y.-S. Lai, J.-S. Chen, P. H. Tsai, C. L. Chen, and C. J. Chang, "Compositional tailored sol-gel SiO_2-TiO_2 thin films: Crystallization, chemical bonding configuration, and optical properties," Journal of Materials Research **20**, 3141–3149 (2005).

[113] H.-S. Hsu, C. Cai, and A. M. Armani, "Ultra-low-threshold Er:Yb sol-gel microlaser on silicon," Optics Express **17**, 23265–23271 (2009).

[114] A. J. Maker, B. A. Rose, and A. M. Armani, "Tailoring the behavior of optical microcavities with high refractive index sol-gel coatings," Optics Letters **37**, 2844–2846 (2012).

[115] R. Mukherjee and A. Sharma, "Instability, self-organization and pattern formation in thin soft films," Soft Matter **11**, 8717–8740 (2015).

[116] A. S. Idris, H. Jiang, and K. Hamamoto, "Multi-layer stacking scheme of sol-gel based SiO_2 towards thicker (>0.8 μm) cladding layers for optical waveguides," IEICE Electronics Express **15**, 20180783–20180783 (2018).

[117] P. Innocenzi, M. O. Abdirashid, and M. Guglielmi, "Structure and properties of sol-gel coatings from methyltriethoxysilane and tetraethoxysilane," Journal of Sol-Gel Science and Technology **3**, 47–55 (1994).

[118] L. H. Slooff, M. J. A. de Dood, A. van Blaaderen, and A. Polman, "Effects of heat treatment and concentration on the luminescence properties of erbium-doped silica sol–gel films," Journal of Non-Crystalline Solids **296**, 158–164 (2001).

[119] T. Chen, H. Lee, and K. J. Vahala, "Thermal stress in silica-on-silicon disk resonators," Applied Physics Letters **102**, 031113 (2013).

[120] J. Ma, X. Jiang, and M. Xiao, "Kerr frequency combs in large-size, ultra-high-Q toroid microcavities with low repetition rates [invited]," Photonics Research **5**, B54–B58 (2017).

[121] R. R. A. Syms and A. S. Holmes, "Deposition of thick silica-titania sol-gel films on Si substrates," Journal of Non-Crystalline Solids **170**, 223 (1994).

[122] X. Min, X. Orignac, and R. M. Almeida, "Striation-free, spin-coated sol-gel optical films," Journal of the American Ceramic Society **78**, 2254–2256 (1995).

[123] P. C. Becker, N. A. Olsson, and J. R. Simpson, *Erbium-doped fiber amplifiers*, Optics and Photonics (Academic Press, San Diego, CA, 1999).

[124] A. Martinez and Z. Sun, "Nanotube and graphene saturable absorbers for fibre lasers," Nature Photonics **7**, 842–845 (2013).

[125] F. X. Kärtner, J. A. der Au, and U. Keller, "Mode-locking with slow and fast saturable absorbers-what's the difference?" IEEE Journal of Selected Topics in Quantum Electronics **4**, 159–168 (1998).

[126] H. A. Haus, J. G. Fujimoto, and E. P. Ippen, "Structures for additive pulse mode locking," Journal of the Optical Society of America. B, Optical physics **8**, 2068 (1991).

[127] I. A. Yarutkina, O. V. Shtyrina, A. Skidin, and M. P. Fedoruk, "Theoretical study of energy evolution in ring cavity fiber lasers," Optics communications **342**, 26–29 (2015).

[128] A. H. Zewail, "Laser femtochemistry," Science **242**, 1645–1653 (1988).

[129] R. Itakura, K. Yamanouchi, T. Tanabe, T. Okamoto, and F. Kannari, "Dissociative ionization of ethanol in chirped intense laser fields," The Journal of Chemical Physics (2003).

[130] F. Korte, J. Serbin, J. Koch, A. Egbert, C. Fallnich, A. Ostendorf, and B. N. Chichkov, "Towards nanostructuring with femtosecond laser pulses," Applied Physics A: Materials Science & Processing **77**, 229–235 (2003).

[131] T. Tanabe, F. Kannari, F. Korte, J. Koch, and B. Chichkov, "Influence of spatiotemporal coupling induced by an ultrashort laser pulse shaper on a focused beam profile," Applied optics **44**, 1092–1098 (2005).

[132] F. Krausz and M. Ivanov, "Attosecond physics," Reviews of modern physics **81**, 163–234 (2009).

[133] T. Gaumnitz, A. Jain, Y. Pertot, M. Huppert, I. Jordan, F. Ardana-Lamas, and H. J. Wörner, "Streaking of 43-attosecond soft-X-ray pulses generated by a passively CEP-stable mid-infrared driver," Optics Express **25**, 27506–27518 (2017).

[134] T. Fortier and E. Baumann, "20 years of developments in optical frequency comb technology and applications," Communications Physics **2**, 1–16 (2019).

[135] A. Hasegawa and Y. Kodama, *Solitons in Optical Communications* (Clarendon Press, 1995).

[136] A. J. DeMaria, D. A. Stetser, and H. Heynau, "SELF MODE-LOCKING OF LASERS WITH SATURABLE ABSORBERS," Applied Physics Letters **8**, 174–176 (1966).

[137] E. P. Ippen, C. V. Shank, and A. Dienes, "Passive mode locking of the CW dye laser," Applied Physics Letters **21**, 348–350 (1972).

[138] U. Keller, W. H. Knox, and H. Roskos, "Coupled-cavity resonant passive mode-locked ti:sapphire laser," Optics Letters **15**, 1377–1379 (1990).

[139] D. E. Spence, P. N. Kean, and W. Sibbett, "60-fsec pulse generation from a self-mode-locked Ti:sapphire laser," Optics Letters **16**, 42–44 (1991).

[140] S. Y. Set, H. Yaguchi, Y. Tanaka, and M. Jablonski, "Laser mode locking using a saturable absorber incorporating carbon nanotubes," Journal of Lightwave Technology **22**, 51–56 (2004).

[141] Q. Bao, H. Zhang, Y. Wang, Z. Ni, Y. Yan, Z. X. Shen, K. P. Loh, and D. Y. Tang, "Atomic-layer graphene as a saturable absorber for ultrafast pulsed lasers," Advanced functional materials **19**, 3077–3083 (2009).

[142] I. N. Duling, "Subpicosecond all-fibre erbium laser," Electronics Letters **6**, 544–545 (1991).

[143] K. Regelskis, J. Želudevičius, K. Viskontas, and G. Račiukaitis, "Ytterbium-doped fiber ultrashort pulse generator based on self-phase modulation and alternating spectral filtering," Optics Letters **40**, 5255–5258 (2015).

[144] Z. Liu, Z. M. Ziegler, L. G. Wright, and F. W. Wise, "Megawatt peak power from a Mamyshev oscillator," Optica **4**, 649–654 (2017).

[145] T. J. Kippenberg, A. L. Gaeta, M. Lipson, and M. L. Gorodetsky, "Dissipative Kerr solitons in optical microresonators," Science **361** (2018).

[146] C.-Z. Ning, "Semiconductor nanolasers and the size-energy-efficiency challenge: a review," Advanced Photonics **1**, 014002 (2019).

[147] H. Pfeifer, L. Ratschbacher, J. Gallego, C. Saavedra, A. Faßbender, A. von Haaren, W. Alt, S. Hofferberth, M. Köhl, S. Linden, and D. Meschede, "Achievements and perspectives of optical fiber Fabry-Pérot cavities," Applied physics. B, Lasers and optics **128**, 29 (2022).

[148] B. C. Collings, K. Bergman, and W. H. Knox, "Stable multigigahertz pulse-train formation in a short-cavity passively harmonic mode-locked erbium/ytterbium fiber laser," Optics Letters **23**, 123–125 (1998).

[149] U. Keller and A. C. Tropper, "Passively modelocked surface-emitting semiconductor lasers," Physics reports **429**, 67–120 (2006).

[150] L. Collot, V. Lefèvre-Seguin, M. Brune, J. M. Raimond, and S. Haroche, "Very high-Q whispering-gallery mode resonances observed on fused silica microspheres," EPL **23**, 327–334 (1993).

[151] C. E. Rüter, K. G. Makris, R. El-Ganainy, D. N. Christodoulides, M. Segev, and D. Kip, "Observation of parity–time symmetry in optics," Nature Physics **6**, 192–195 (2010).

[152] K. Takata, K. Nozaki, E. Kuramochi, S. Matsuo, K. Takeda, T. Fujii, S. Kita, A. Shinya, and M. Notomi, "Observing exceptional point degeneracy of radiation with electrically pumped photonic crystal coupled-nanocavity lasers," Optica **8**, 184 (2021).

[153] H. Hodaei, M.-A. Miri, M. Heinrich, D. N. Christodoulides, and M. Khajavikhan, "Parity-time-symmetric microring lasers," Science **346**, 975–978 (2014).

[154] K. Komagata, A. Tusnin, J. Riemensberger, M. Churaev, H. Guo, A. Tikan, and T. J. Kippenberg, "Dissipative Kerr solitons in a photonic dimer on both sides of exceptional point," Communications Physics **4**, 1–13 (2021).

[155] A. M. Yacomotti, S. Haddadi, and S. Barbay, "Self-pulsing nanocavity laser," Physical Review. A **87**, 041804 (2013).

[156] S. Fujii, A. Hori, T. Kato, R. Suzuki, Y. Okabe, and others, "Effect on Kerr comb generation in a clockwise and counter-clockwise mode coupled microcavity," Optics Express **25**, 28969–28982 (2017).

[157] J. Yelo-Sarrión, F. Leo, and S. Pierre-Gorza, "Mode-locking in active PT-symmetric dimers," in "CLEO 2024," (Optica Publishing Group, Washington, D.C., 2024), p. FTh4D.5.

[158] A. Nakashima, S. Fujii, R. Imamura, K. Nagashima, and T. Tanabe, "Deterministic generation of a perfect soliton crystal microcomb with a saturable absorber," Optics Letters **47**, 1458–1461 (2022).

Appendix A

Constants, symbols, and relations

Table A.1 Lists of symbols and definitions.

Symbol	Unit	Description
a_0	–	intracavity field, $\lvert a_0\rvert^2$ corresponds to the intracavity photon number
A_{eff}	m^2	effective mode area
c	m/s	speed of light
D_1	rad·Hz	cavity FSR, $D_1/2\pi = t_{\text{r}}^{-1}$
D_2	rad·Hz	second order dispersion related to β_2
f_{ceo}	Hz	carrier envelope offset frequency
f_{rep}	Hz	repetition frequency
I_{sat}	W/m^2	saturation intensity
L	m	cavity length
n	–	refractive index, $n = 1.44$ in silica
P_{cav}	W	intracavity power
$P_{\text{cav}}^{\text{FWM}}$	W	threshold intracavity power of degenerate FWM
P_{in}	W	input pump power
$P_{\text{in}}^{\text{FWM}}$	W	threshold input power of degenerate FWM
$P_{\text{in}}^{\text{SRS}}$	W	threshold input power of SRS

Table A.2 Lists of symbols and definitions.

Symbol	Unit	Description
Q	–	optical quality factor
Q_{ext}	–	external optical quality factor, $Q_{\text{ext}} = \omega_0/\gamma_{\text{ext}}$
Q_{int}	–	intrinsic optical quality factor, $Q_{\text{int}} = \omega_0/\gamma_{\text{int}}$
Q_{total}	–	total optical quality factor, $Q_{\text{total}} = \omega_0/\gamma = Q_{\text{int}}^{-1} + Q_{\text{ext}}^{-1}$
s_{in}	–	input field from the waveguide
t_{r}	s	cavity round-trip time
V_{eff}	m^3	effective mode volume
v_{g}	m/s	group velocity
α_0	–	modulation depth
α_{ns}	–	non-saturable loss
β	–	propagation constant
β_2	s^2/m	second order dispersion
$\Delta\omega_0$	rad·Hz	pump detuning, $\Delta\omega_0 = \omega_{\text{p}} - \omega_0$
η	–	coupling ratio, $\eta = \gamma_{\text{ext}}/\gamma_{\text{int}}$
γ	s^{-1}	cavity decay rate
γ_{ext}	s^{-1}	coupling rate to the external waveguide
γ_{int}	s^{-1}	intrinsic cavity decay rate
γ_{NL}	$\text{W}^{-1}\text{m}^{-1}$	nonliear coefficient
λ_{m}	m	wavelength of m-th mode
μ	–	mode number, the center mode is $\mu = 0$
ω_0	rad·Hz	angular frequency of pump mode
ω_{m}	rad·Hz	angular frequency of m-th mode
ω_{p}	rad·Hz	angular pump frequency
τ_{p}	s	photon lifetime, $\tau_{\text{p}} = \gamma^{-1}$
$\hbar$	$\text{J}\cdot\text{s}/\text{rad}$	Planck constant

Appendix B

Abbreviations

Table B.1 Lists of important abbreviations.

Abbreviation	Original expression
AOM	acousto-optic modulator
ASE	amplified spontaneous emission
CNT	carbon nanotube
CW	continuous wave
DAQ	data acquisition
Er	erbium
FG	function generator
FSR	free spectral range
FWM	four wave mixing
LLE	Lugiato-Lefever equation
MZI	Mach-Zehnder interferometer
OSA	optical spectrum analyzer
OSC	oscilloscope
PD	photodiode, photodetector
PWM	power meter
SA	saturable absorber
SEM	scanning electron microscope
SESAM	semiconductor saturable absorber mirror
SPM	self-phase modulation
SRS	stimulated Raman scattering
WGM	whispering-gallery-mode
XPM	cross-phase modulation

List of publications and presentations

Publications (related to this thesis)

1. 今村陸, 鈴木 S.L.P. 智生, 石田蘭丸, 藤井瞬, セット ジ イヨン, 山下真司, 田邉孝純, “小型モード同期レーザ開発に向けたエルビウム添加微小光共振器の作製と可飽和吸収特性,” 電気学会論文誌 C, Vol. 142, No. 3, (2022).
2. R. Imamura, S. Fujii, A. Nakashima, and T. Tanabe, “Exceptional point proximity-driven mode-locking in coupled microresonators,” Optics Express, Vol. 32, Issue 13, pp. 22280-22290, (2024).
3. R. Imamura, S. Fujii, K. Nagashima, and T. Tanabe, “Scalable fabrication of erbium-doped high-Q silica microtoroid resonators via sol-gel coating,” Optics Continuum, Vol. 4, Issue 3, pp. 512-521 (2025).

Other publications

1. Y. Zhuang, H. Kumazaki, S. Fujii, R. Imamura, N. A. B. Daud, R. Ishida, H. Chen, and T. Tanabe, “Coupling of a whispering gallery mode to a silicon chip with photonic crystal,” Opt. Lett. Vol. 44, Issue 23, pp. 5731-5734, (2019).
2. T. S.L.P. Suzuki, A. Nakashima, K. Nagashima, R. Ishida, R. Imamura, S. Fujii, S. Y. Set, S. Yamashita, and T. Tanabe, “Design of a passively mode-locking whispering-gallery-mode microlaser,” Journal of the Optical Society of America B, Vol. 38, Issue 10, pp. 3172-3178, (2021).
3. A. Nakashima, S. Fujii, R. Imamura, K. Nagashima, and T. Tanabe, "Deterministic generation of a perfect soliton crystal microcomb with a saturable absorber," Opt. Lett. Vol. 47, 1458–1461 (2022).

Presentations

1. 今村陸, Tomoki S. L. Prugger Suzuki, 石田蘭丸, 鈴木良, 藤井瞬, 伊藤瑞生, 牧英之, Lan Yang, 田邉孝純, “小型モード同期レーザに向けたエルビウム添加微小光共振器の作製,” 第 66 回応用物理学会春季学術講演会, 東京, 2019 年 3 月 10 日口頭発表.
2. R. Imamura, S. Fujii, T. S. L. P. Suzuki, R. Suzuki, R. Ishida, M. Ito, H. Maki, L. Yang, T. Tanabe, “Fabrication of Er-doped Microresonator for On-chip Mode-locked Laser with CNT as Saturable Absorber,” The 8th Advanced Lasers and Photon Sources (ALPS2019), Yokohama, Japan, 2019 年 4 月 25 日口頭発表.
3. R. Imamura, S. Fujii, T. S. L. P. Suzuki, R. Suzuki, R. Ishida, M. Ito, H. Maki, L. Yang, T.

Tanabe, “Saturable Absorption with CNT Coupled WGM and Fabrication of Er-doped Microresonator for On-chip Mode-locked Laser,” CLEO/Europe-EQEC 2019, Munich, Germany, 2019 年 6 月 23 日口頭発表.

4. 今村陸, 鈴木 S. L. P. 智生, 石田蘭丸, 藤井瞬, 牧英之, Lan Yang, 田邉孝純, “小型モード同期レーザ開発に向けた可飽和吸収特性とエルビウム添加微小光共振器の作製,” 電気学会 2019 年電子・情報・システム部門光・量子デバイス研究会, 東京, 2019 年 7 月 26 日口頭発表.
5. 今村陸, 鈴木 S. L. P. 智生, 藤井瞬, 石田蘭丸, 田邉孝純, “微小光共振器を用いたモード同期レーザにおける数値解析,” 第 80 回応用物理学会秋季学術講演会, 札幌, 2019 年 9 月 21 日口頭発表.
6. 今村陸, 長島圭吾, 石田蘭丸, 田邉孝純, “10 nm 縦モード間隔を有する Er 添加トロイド微小光共振器,” 第 67 回応用物理学会春季学術講演会, 東京, 2020 年 3 月 12 日口頭発表.
7. 今村陸, 長島圭吾, 石田蘭丸, 田邉孝純, “PDMS を用いた微小光共振器への CNT のコーティングと可飽和吸収特性,” 第 67 回応用物理学会春季学術講演会, 東京, 2020 年 3 月 12 日口頭発表.
8. 今村陸, 長島圭吾, 藤井瞬, 熊崎基, 田邉孝純, コーティング法による Er 添加トロイド微小光共振器の作製, 第 68 回応用物理学会春季学術講演会, オンライン開催, 2021 年 3 月 19 日口頭発表.
9. R. Imamura, A. Nakashima, K. Nagashima, T. S. L. Prugger Suzuki, R. Ishida, S. Fujii, and T. Tanabe, “Design of a Passively Mode-locked Microlaser with an Er-doped Microcavity and Carbon Nanotubes,” CLEO/Europe-EQEC 2021, Online, 2021 年 6 月 23 日口頭発表.
10. R. Imamura, K. Nagashima, and T. Tanabe, “Measurement of saturable absorption behavior of CNT/PDMS coated high-Q microcavity towards modelocking of Er-doped laser (invited),” META 2021, Online, 2021 年 7 月 22 日口頭発表
11. R. Imamura, Y. Tate, A. Nakashima, K. Nagashima, S. Fujii, and T. Tanabe, “Mode-locked Operation in a Coupled Microresonator System with Gain and Nonlinear Loss,” CLEO Pacific Rim 2022, Sapporo, Japan, 2022 年 8 月 4 日口頭発表.
12. 今村陸, 藤井瞬, 中島綾太, 田邉孝純, “利得と非線形損失を有する微小光共振器結合系におけるモード同期動作に向けた数値解析,” 第 83 回応用物理学会秋季学術講演会, 仙台, 2022 年 9 月 22 日口頭発表.
13. R. Imamura, S. Fujii, A. Nakashima, and T. Tanabe, “Numerical analysis of mode-locked regime in a coupled microresonator system,” The 12th Advanced Lasers and Photon Sources (ALPS2023), Yokohama, Japan, 2023 年 4 月 20 日口頭発表.
14. R. Imamura, S. Fujii, A. Nakashima, and T. Tanabe, “Passive mode-locking without a saturable absorber using a coupled microresonator,” CLEO 2023, San Jose, California, USA, 2023 年 5

月 11 日ポスター発表.

15. R. Imamura, S. Fujii, A. Nakashima, and T. Tanabe, “Mode-locking System of Coupled Microcavities with Gain and Nonlinear Loss,” CLEO/Europe-EQEC 2023, Munich, Germany, 2023 年 6 月 27 日ポスター発表.
16. 今村陸, 藤井瞬, 中島綾太, 田邉孝純, “例外点近傍における結合共振器系受動モード同期レーザーの理論実証,” レーザー学会学術講演会第 44 回年次大会, 東京, 2024 年 1 月 18 日口頭発表.
17. R. Imamura, S. Fujii, A. Nakashima, and T. Tanabe, “Vicinity of exceptional point-induced mode-locking in coupled microresonators,” CLEO 2024, Charlotte, USA, 2024 年 5 月 8 日口頭発表.

Acknowledgments

本当に興味深いのは，作製した共振器をライトで照らし測定系のカメラで見ただけで，そこまでの作製プロセスの良し悪しがわかることです．高 Q 値な共振器は低 Q 値なものと比べて明らかに光輝いて見えます．この理由は，Q 値は共振器表面の粗さに大きな影響を受ける，という田邉研究室では当たり前のことですが，ナノ〜マイクロメートルという本来肉眼では捉えられない違いが，光の散乱・反射という目に見えてわかるところに毎回密かに感心し，楽しみにしていました．建築家丹下健三が言ったように「美しきもののみ機能的である」，を体現したかのような微小光共振器に，そしてそれを自ら実践できるデバイス作製に，面白さを感じられたのかもしれません．デバイス作製は大変だぞ，と言われ引き継いだ大学 4 年の頃から数えて約 4 万個の共振器を作製してきましたが，私の目に映る微小光共振器の持つ美しさは今もそのままであることに感慨深く思います．

本研究は慶應義塾大学理工学部電子工学科田邉研究室，田邉孝純教授のご指導の元行われたものです．学部生の頃より一貫してご指導くださった田邉教授には，言葉では尽くせぬほどの感謝を申し上げます．研究に行き詰まったときも，拙い問いに対しても，常にオープンマインドに，そして忍耐強く接してくださった先生の姿勢は，私の学びと成長にとって何よりの支えでした．今後，私自身が研究開発に携わる者として，先生のように本質を見抜き，誠実に研究と向き合える人間でありたいと強く願っております．加えて国際会議発表をはじめとする，様々な普通はできない体験をさせていただきました．ここに厚く御礼を申し上げます．

本論文の審査にあたり，副査を引き受けていただいた，慶應義塾大学理工学部の斎木敏治教授，武岡正裕教授，渡邉紳一教授，東京大学先端科学技術研究センターの Set Sze Yun 教授に感謝申し上げます．お忙しい中，長期間にわたる審査を引き受け，各審査会へお越しいただき感謝いたします．

研究を行うにあたり，多くの研究室メンバーや共同研究者に恵まれました．研究活動は必ずしも明るい日々だけではありませんでしたが，そんな状況だったからこそ，周りの方々とのつながりを強く意識できた数年間でした．誰かと二言三言話すだけで，気分が晴れ，知らぬ間に元気づけられることが何度もありました．特に藤井瞬助教や熊﨑基さんをはじめとする先輩方には，研究室配属から約 7 年にわたって公私共にサポートいただきました．さらに，長島圭吾君，菅野凌君，高野淳史君，國分淳之介君をはじめとする，多くの優秀な

後輩にも恵まれました．研究室生活を通して関わった皆様へ，これまでの感謝と共にこれからの成功を心から祈っております．また就職後すぐにもかかわらず，快く送り出してくださった日本サムスン株式会社の上司および先輩方にも，この場を借りて深く感謝申し上げます．

最後に，そばで支えてくれた妻には心から感謝しています．また博士論文の執筆中に，妻の妊娠が判明し，生まれてくる娘の存在は大きな心の支えとなりました．今は，無事に生まれてきてくれる日を心から楽しみにしています．そして遠い鹿児島から応援してくれている家族に感謝を伝えたいと思います．いつでも帰ることのできる場所を用意して，そこにいてくれると思うだけで本当に心強かったです．妻，娘，父，母，兄，わがままだけど聡明な妹へ，ありがとうございました．

2025 年 8 月　今村陸